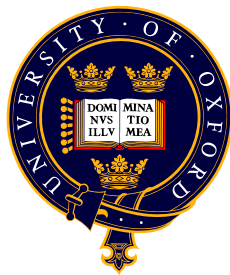


Signal processing methods for the analysis of cerebral blood flow and metabolism

Tingying Peng
Lincoln College



Robotics Research Group
Department of Engineering Science
University of Oxford

Trinity 2008

This thesis is submitted to the Department of Engineering Science, University of Oxford, for the degree of Doctor of Philosophy. This thesis is entirely my own work, and, except where otherwise indicated, describes my own research.

Tingying Peng
Lincoln College

Doctor of Philosophy
Trinity 2008

Signal processing methods for the analysis of cerebral blood flow and metabolism

Abstract

An important protective feature of the cerebral circulation is its ability to maintain sufficient cerebral blood flow and oxygen supply in accordance with the energy demands of the brain despite variations in a number of external factors such as arterial blood pressure, heart rate and respiration rate. If cerebral autoregulation is impaired, abnormally low or high CBF can lead to cerebral ischemia, intracranial hypertension or even capillary damage, thus contributing to the onset of cerebrovascular events.

The control and regulation of cerebral blood flow is a dynamic, multivariate phenomenon. Sensitive techniques are required to monitor and process experimental data concerning cerebral blood flow and metabolic rate in a clinical setting. This thesis presents a model simulation study and 4 related signal processing studies concerned with CBF regulation.

The first study models the regulation of the cerebral vasculature to systemic changes in blood pressure, dissolved blood gas concentration and neural activation in a integrated haemodynamic system. The model simulations show that the three pathways which are generally thought to be independent (pressure, CO_2 and activation) greatly influence each other, it is vital to consider parallel changes of unmeasured variability when performing a single pathway study. The second study shows how simultaneously measured blood gas concentration fluctuations can improve the accuracy of an existing frequency domain technique for recovering cerebral autoregulation dynamics from spontaneous fluctuations in blood pressure and cerebral blood flow velocity. The third study shows how the continuous wavelet transform can recover both time and frequency information about dynamic autoregulation, including the contribution of blood gas concentration. The fourth study shows how the discrete wavelet transform can be used to investigate frequency-dependent coupling between cerebral and systemic cardiovascular dynamics. The final study then uses these techniques to investigate the systemic effects on resting BOLD variability.

The general approach taken in this thesis is a combined analysis of both modelling and data analysis. Physiologically-based models encapsulate hypotheses about features of CBF regulation, particularly those features that may be difficult to recover using existing analysis methods, and thus provide the motivation for developing both new analysis methods and criteria to evaluate these methods. On the other hand, the statistical features extracted directly from experimental data can be used to validate and improve the model.

Contents

1	Introduction	2
1.1	Physiological Basis	3
1.2	Measuring Cerebral Blood Flow and Metabolism	10
1.3	Summary of Thesis	12
2	Literature review	15
2.1	Introduction	15
2.2	Control of cerebral blood flow	15
2.3	Clinical studies of autoregulation	17
2.4	Analysis of clinical autoregulation data	30
2.5	Summary	47
3	System definition	50
3.1	Introduction	50
3.2	Model Description	51
3.3	Simulation results	57
3.4	Model linearisation	61
3.5	Discussion	76
3.6	Summary	78
4	Multivariate system identification for cerebral Autoregulation	80
4.1	Introduction	81
4.2	Method	84
4.3	Results	88
4.4	Discussion	94
5	Wavelet phase synchronization analysis of cerebral blood autoregulation	101
5.1	Introduction	102
5.2	Method	104
5.3	Results	110
5.4	Discussion	117
5.5	Conclusion	120

6	The effects of age on the spontaneous low-frequency oscillations in cerebral and systemic cardiovascular dynamics	121
6.1	Introduction	122
6.2	Methods	124
6.3	Results	129
6.4	Discussion	135
7	Quantification of the effects of CO₂ on the resting BOLD signal	141
7.1	Introduction	141
7.2	Methods	143
7.3	Results	147
7.4	Discussion	155
7.5	Conclusion	157
8	Conclusion	158
8.1	Summary	158
8.2	Limitations and Future work	160

Acknowledgements

Funding for this thesis was generously provided by Dorothy Hodgkin Postgraduate Awards, jointly funded by EPSRC and Hutchison Whampoa. Essential advice and guidance were administered by Drs. Stephen Payne and Yiannis Ventikos. Without their experienced guidance, constructive criticism, technical expertise, and finally patient and painstaking proof-reading this research would not have happened.

I would like to thank collaboration and assistance of researchers at the experimental part: Dr Mark Poulin of University of Calgary, Canada, Dr Phillip Ainslie of University of Otago, New Zealand, Dr Richard Wise of University of Cardiff, UK and Prof Peter Robbins of University of Oxford, UK. For technical assistance I would like to thank Drs. Alexander Rowley, Nicholas Hughes and Mark Ebden of Institute of Biomedical Engineering, University of Oxford.

Members of the PUMMA Group and its associated researchers formed a good working environment in all respects: Drs Michael Chappell and Alexander Rowley, Mr Hasan Abatay, Miss Samira Kazan, Mr Chang Sub Park and Mr Shen-wei Su.

Finally, most thanks of all are reserved for my family and friends, for their love and support.

Introduction

The brain is a complex and heterogeneous organ that is critically dependent on its blood supply. A human brain typically comprises about 2% of the body mass yet receives 12-15% of cardiac output and consumes around 20% of the oxygen entering the body (Siesjo (1978)). Insufficient blood flow and oxygen supply will result in cerebral ischemia, in which the neurons and other blood cells are damaged and lose their function. On the other hand, since the skull is a rigid container, excessive blood perfusion can lead to intracranial hypertension or even capillary damage. As a result, numerous regulatory mechanisms act to maintain an adequate blood and oxygen supply to the brain in accordance with its underlying functional or metabolic needs, despite considerable external changes. Cerebral autoregulation, in particular, refers to the capacity of cerebral blood flow (CBF) to remain relatively constant despite variations in perfusion pressure (CPP) (the difference between mean arterial blood pressure (ABP) and intracranial pressure (ICP, the pressure exerted by the skull on brain tissue)) (Lassen (1980)).

Cerebral autoregulation is known to be impaired after severe head injury. This can increase the risk of secondary neuronal injury in patients. Ischaemic stroke can damage numerous homeostatic control mechanisms, which can result in hypertension (high arterial blood pressure). Impaired cerebral autoregulation in these circumstances can thus lead to excessive blood flow, severely increasing the risk of haemorrhage. Understanding the underlying physiological processes of this autoregulation mechanism is key to investigating

the various factors that leads to a pathological autoregulation status.

Besides pressure regulation, neural activation and blood gas reactivity are also known to be mechanisms responsible for controlling blood flow. The development of sensitive techniques for monitoring cerebral blood flow and metabolic rate has the potential to contribute significantly to their clinical use in both health and disease. This thesis, therefore, reports developments in analysis of clinical measurements of cerebral circulation and metabolism, particularly focusing on cerebral autoregulation and its interaction with the other two mechanisms. This chapter provides an outline of the physiological background, the key measurement techniques and a description of the approach taken.

1.1 Physiological Basis

1.1.1 Brain Structure

The human brain is surrounded and protected by the skull, the meninges (three layers of connective tissue called the *dura mater*, the *arachnoid mater* and the *pia mater*) and the cerebrospinal fluid (CSF), a watery cushion that flows in the subarachnoid space.

The brain consists of two cerebral hemispheres, the brain stem and the cerebellum. The cerebral hemispheres consist of a core of grey matter, surrounded by white matter and an outer cortex of grey matter, the cerebral cortex, which is around 5 mm in thickness covering the cerebral hemispheres. The cerebral cortex is highly folded into ridges and dips (known as gyri and sulci) which greatly increases its surface area (Nolte (2002)).

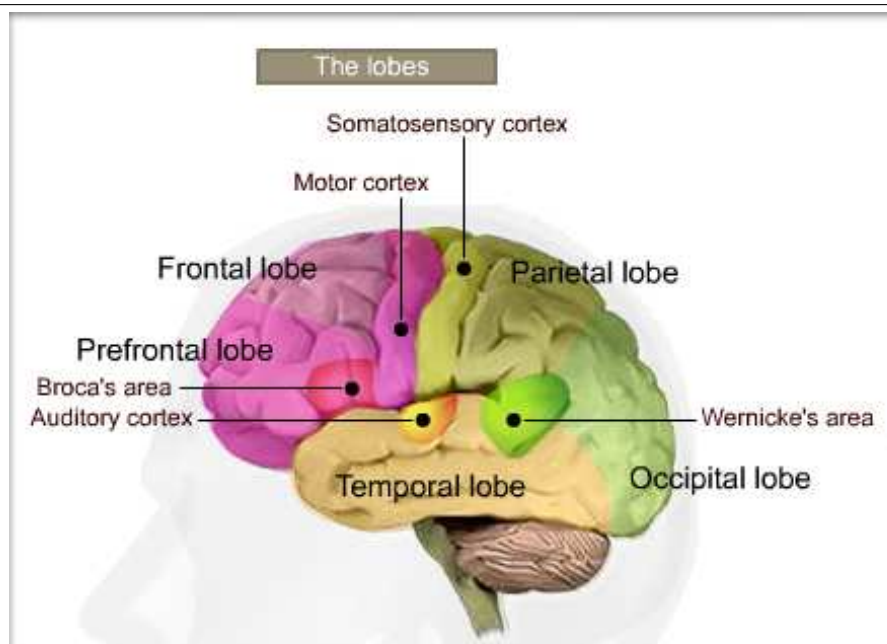
1.1.2 Brain Function

How the brain works has been the subject of much debate. Since the brain has a relatively uniform appearance, many scientists believe in the theory of mass action, i.e. that areas of the brain work together for every task without much regional specialization (Finger (1999)). In contrast, another hypothesis has been proposed to argue that the specific

types of brain function are associated with particular regions of the brain, forming the foundation of the concept of cortical functional localization.

The second idea was supported by the observation that damage to different areas of the brain produced relatively specific deficits in patients. Most recently, with the development of functional neuroimaging techniques as explained below, it is possible to detect the small, local variations in a particular brain region that relate to different types of behaviour, thus further improving our understanding of the brain's functional structure. Figure 1.1 is an anatomical structure of the brain, illustrating where the different brain functions occur, as a function map.

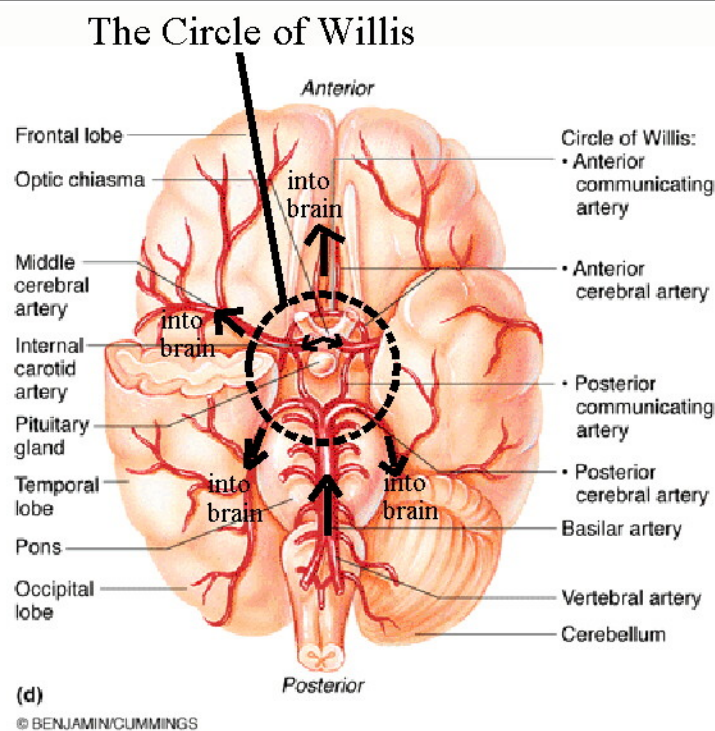
Figure 1.1 Functional organization of the human brain. The occipital lobe in the right hemisphere is devoted to vision and the parietal lobe above deals with movement, position, orientation and calculation. The frontal and prefrontal lobes in the left hemisphere are often considered to be the most highly developed regions, dealing with the most complex thought, such as decision making, planning, conceptualising, attention control and working memory. The temporal lobes below deal with sound and speech comprehension and some aspects of memory. (Taken from www.newscientist.com)



1.1.3 Cerebral circulation

Compared to other organs, the brain is unusual in that it is supplied by four major arteries that eventually coalesce to form the Circle of Willis, shown in Figure 1.2 (Willis (1664)). These primary vessels are the two internal carotid arteries (ICA) and two vertebral arteries (VA), which unite intracranially to form the basilar artery. Under normal circumstances (especially in young people), such an arrangement permits an adequate perfusion of all parts of the brain despite the occlusion or obstruction of any one of the four arterial vessels (Edvinsson et al. (1992)).

Figure 1.2 Schematic diagram of the Circle of Willis. (Taken from www.webanatomy.net)



The ICA are quantitatively more important—each contributes approximately 40% to the total perfusion of the brain. Each ICA enters the cranial cavity through the foramen lacerum, grooves the lateral aspect of the sphenoid bone, and divides into four major branches: the anterior cerebral, the middle cerebral, the anterior choroidal, and the posterior communicating arteries. The arterial component of the cerebral circulation terminates at the level of

autoregulating capillaries, where the network chemical exchange of metabolic substances takes place. In contrast to the systemic circulation, the vascular wall of cerebral vessels is impermeable to large organic molecules and plasma proteins. This aspect of the cerebral circulation is termed the *blood-brain barrier*.

The venous component of the cerebral circulation, responsible for carrying deoxygenated blood and waste products away from the brain, can be separated into two subdivisions: superficial and deep. Superficial veins that drain the cortex and white matter coalesce towards the pia mater at the outer surface of the brain, finally joining the dural venous sinuses. Deep cerebral veins that drain deeper structures finally coalesce to the great cerebral vein which eventually joins the straight sinus. The final venous outflow is through the sigmoid sinuses which becomes the internal jugular vein in the neck.

1.1.4 Brain Energy Metabolism

Cerebral blood flow transports oxygen to brain cells via the iron containing oxygen transport metalloprotein *haemoglobin*. Haemoglobin binds with oxygen in the pulmonary capillaries adjacent to the alveoli, termed oxyhaemoglobin. Oxyhaemoglobin is then transported in the red blood cells to brain cells and releases the oxygen for cell use. *Deoxyhaemoglobin* is the form of haemoglobin without the bound oxygen. Besides the haemoglobins is also found *cytochrome-c-oxidase (CtOx)*. CtOx is the final electron acceptor of the mitochondrial electron transfer chain and catalyses the metabolism of oxygen within cells. Monitoring of brain concentrations of oxyhaemoglobin, deoxyhaemoglobin and cytochrome-c-oxidase is thus an alternative to monitoring cerebral blood flow for investigating cerebral autoregulation.

1.1.5 Regulation of Blood Flow

As mentioned above, it is extremely important that cerebral blood flow and oxygen supply are efficiently regulated, in proportion to the energy demand of brain cells. The underlying

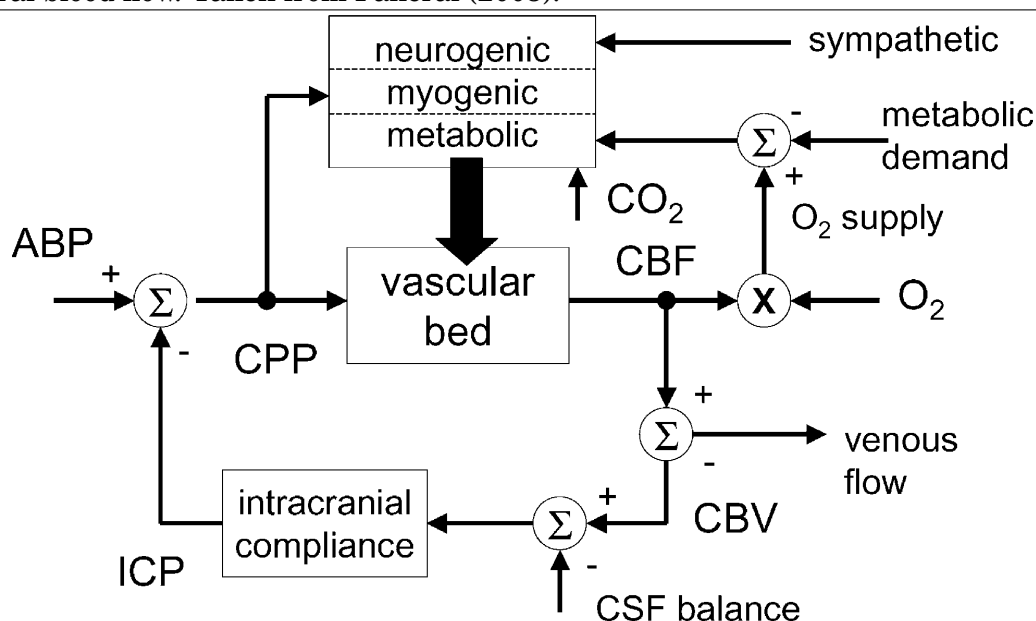
mechanisms through which blood flow is regulated are highly complex, yet incompletely understood.

Figure 1.3 is a concise summary of the mechanisms responsible for cerebral blood flow regulation. CBF is driven through the cerebral vasculature by the cerebral perfusion pressure (CPP), which depends upon the difference between ABP and ICP. Changes in ICP occur when cerebral volume (CBV) changes occur, for example due to loss of CSF in head injury. Global cerebrovascular resistance (CVR) defined as:

$$CVR = \frac{CPP}{CBF}, \quad (1.1)$$

is one convenient lumped descriptor of the properties of the cerebral vasculature.

Figure 1.3 Simplified diagram of the main mechanisms responsible for the regulation of cerebral blood flow. Taken from Panerai (2003).



Several hypotheses have been proposed to describe the mechanisms that act on the properties of the cerebral vasculature (described quantitatively by CVR) to maintain adequate oxygen supply: myogenic, metabolic, and neurogenic mechanisms. These mechanisms are convenient groupings of different regulation pathways that have been observed experimentally. Current understanding of these pathways will now be briefly summarised.

The Myogenic Hypothesis

The myogenic hypothesis of autoregulation suggests that the smooth muscle cells in cerebral vessels either constrict or dilate in response to increases or decreases in the transmural pressure, respectively. This hypothesis was first reported in Bayliss (1902), who suggested that a myogenic response arises by the altered state of the actin and myosin filaments in smooth muscle cells, induced by a rapid change in the intravascular pressure. Numerous studies have confirmed that isolated cerebral vessels exhibit this myogenic response. If autoregulatory responses rely predominantly on myogenic factors, cerebral vessels would be expected to constrict in response to increases in intravascular pressure, despite changes in cerebral perfusion pressure. This prediction, however, is opposite to the experimental observation that increases in venous pressure induce dilation, not constriction, in cerebral arterioles (Wei and Kontos (1982); Mcpherson et al. (1988)).

The Metabolic Hypothesis

Metabolic mechanisms of blood flow regulation hypothesize that the decreased local blood flow allows accumulation of vasodilating metabolites (Harper and Jennett (1990)). When CPP falls, CBF also falls, preventing the wash-out of vasoactive molecules, such as CO_2 , H^+ , K^+ and adenosine (Kuschinsky and Wahl (1978)). In particular, since CO_2 is a major end product of neuronal metabolism, this metabolic pathway is thought to be a major regulator of CBF response to neural activity. During brain activation, arterial pressure remains constant, but the increase of local metabolism leads to increasing tissue concentrations of metabolites which results in a vasodilatory effect. Thus the resistance decreases and blood flow increases, supplying the necessary nutrients as required.

The Neurogenic Hypothesis

Since the extraparenchymal and intraparenchymal blood vessels are innervated (i.e. they are contacted by nerves in a manner comparable with blood vessels in the periphery), a hypothesis has arisen that the nerves innervating cerebral vessels contain transmitters, which are received by receptors residing on cerebral vessels, inducing vasoconstriction or vasodilation (McCulloch and Edvinsson (1984)). Numerous reports, however, have

demonstrated that autoregulation is preserved in sympathetically and parasympathetically denervated animals (Busija and Heistad (1984)), suggesting that the sympathetic or parasympathetic nervous systems are unlikely to play a central role in CBF regulation. Other studies have reported that the lower limit of CBF autoregulation was shifted toward higher levels of blood pressure in sympathetic activation or parasympathetic denervation (Paulson et al. (1990); Morita et al. (1994)), suggesting a modulating effect of sympathetic control of cerebral circulation. However, the role of autonomic modulation on autoregulation is far from unanimous in the literature. A recent discussion, van Lieshout and Secher (2008), illustrates this controversy, by outlining both point and counterpoint for the influence of sympathetic activity on cerebral blood flow. Though it draws different conclusions, it agrees that the effect of sympathetic stimulation is practically nil under normal conditions, but may be activated to compensate the blood supply when cardiac output or blood pressure become compromised.

Other effects

Numerous investigations of isolated arteries have shown that endothelial cells may cause the relaxation/contraction of vascular smooth muscle via the release of endothelium-derived relaxing/contractile factors (Furchgott (1984); Rubanyi et al. (1986); Rosenblum et al. (1987)). Though the role of endothelium-derived factors in cerebral autoregulation has been studied extensively, whether these factors contribute significantly to autoregulation, however, remains unclear. Most studies performed *in vitro* suggest that the endothelium may function as a transducer by releasing or suppressing myogenic factors in response to altered intravascular pressure or flow; however, studies performed *in vivo* are approximately evenly divided between those that support and those that refute a role for the endothelium in cerebral vascular autoregulation (Edvinsson et al. (1992)).

1.2 Measuring Cerebral Blood Flow and Metabolism

To understand the regulation of cerebral blood flow in health and disease requires accurate measurements of cerebral blood flow and metabolism. Numerous invasive and non-invasive techniques have been developed, each of which has unique applications, advantages and limitations. Here only the key non-invasive techniques currently used for blood flow and oxygenation measurement are described below. A more detailed review of the historical development of these techniques and others important in the study of cerebral autoregulation can be found in Chapter 2.

Transcranial Doppler Ultrasonography

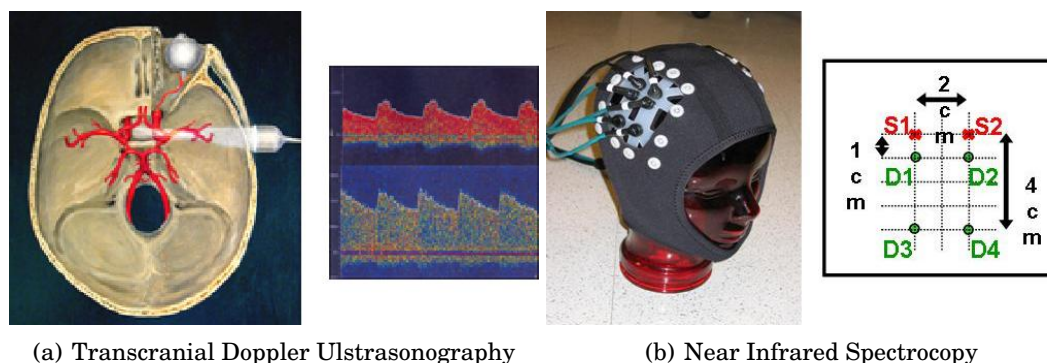
Transcranial Doppler Ultrasonography (TCD) is a non-invasive technique that permits observation of the velocity, direction and properties of blood flow in the middle cerebral artery by means of a pulsed ultrasonic beam (Aaslid et al. (1982)), as shown in Figure 1.4(a). Averaging of the TCD-measured cerebral blood flow waveform over the cardiac cycle is typically performed in autoregulation studies, and temporal resolutions of around 10Hz are typically obtained, which is sufficient to capture all variability in mean cerebral blood flow velocity. However, it is worth to point out TCD measured CBF velocity is not a direct measurement of blood flow and its variations can only represent the changes of blood flow with the assumption of unvaried vessel diameter during the measurement period.

Near Infrared Spectroscopy

Near Infrared Spectroscopy (NIRS) is a technique for the non-invasive measurement of tissue-averaged oxygen concentration changes by measuring the attenuation of near infrared light (spectrum 700-1000nm) passing from a laser diode to a sensor both of which are incorporated in a head-mounted probe, shown in figure 1.4(b). Since the light-absorption spectra of oxyhaemoglobin and deoxyhaemoglobin differ in the near-infrared region, this attenuation can be related to changes in the tissue averaged concentration of oxyhaemoglobin (O_2Hb), deoxyhaemoglobin (HHb), total haemoglobin (THb) and cytochrome-c-oxidase ($CtOx$)

using the modified Beer-Lambert Law (Delpy and Cope (1997)). Measurements have a time resolution of around 6Hz and multi-channel NIRS can also provide a low spatial resolution.

Figure 1.4 a) Left: the anatomical distribution of intracerebral arteries that can be insonated using a standard TCD machine; Right: a typical raw TCD data example. b) Left: a typical NIRS set-up; Right: a typical position of head-mounted probes.

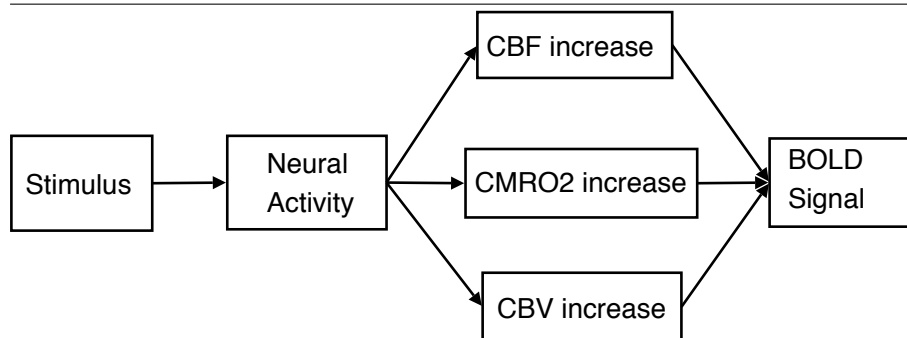


Blood-oxygen-level-dependent fMRI

Haemoglobin is diamagnetic when oxygenated but paramagnetic when deoxygenated. The magnetic resonance (MR) signal of blood is therefore slightly different depending on the level of oxygenation. These differential signals can be detected using an appropriate MR pulse sequence as the blood-oxygen-level dependent (BOLD) contrast. Though fMRI is widely used to map the brain function (Purves et al. (1997)), it is not a directly measure of neural activity. Instead, it is an endogenous contrast mechanism that mirrors the proportion of deoxyhemoglobin in a particular brain region, depending on the combined changes in cerebral blood flow, cerebral blood volume, and cerebral metabolic rate of oxygen ($CMRO_2$). As illustrated in Figure ??, the stimulus first induces local changes in neural activity, which then triggers increased energy metabolism with accompanying changes in CBF , CBV and $CMRO_2$. These physiological changes combine to alter the MRI signal, which is known as the BOLD signal measured by fMRI. Similar to NIRS, fMRI also utilises signals intrinsic to the brain rather than signals originating from an exterior stimulus; consequently, repeated observations can be made on the same individual, providing a major advantage over other imaging methods. fMRI provides superior spatial resolution (currently about 2 or 3 millimetres) and good temporal resolution (about 1 second). At

present fMRI is mostly used to analyse brain function, however, it does provide a method to investigate local cerebral oxygenation and metabolic rate, which cannot be achieved by TCD and NIRS.

Figure 1.5 The chain of events leading to the BOLD signal.



1.3 Summary of Thesis

A better understanding of regulation of cerebral blood flow has the potential to contribute significantly to improved clinical practice, allowing better monitoring and assessment of patients of post-head injury, post ischemic stroke and also gaining a better understanding of how systemic variations influence functional imaging of the brain. The regulation of cerebral blood flow is a very complex system which involves numerous control mechanisms. Experiments are often carried out to test the flow response to the proposed stimuli and to identify a particular regulatory pathway. In reality, however, the completely isolated regulatory pathway can never exist as the parallel changes in unmeasured variability are difficult to control and may also have a significant effect on the results. Any analytical techniques must appreciate this reality, and their performance must be evaluated with these considerations in mind.

This thesis focuses on the clinical evaluation of signal processing techniques for the analysis of mechanisms regulating cerebral blood flow in humans. After a thorough literature review in Chapter 2, Chapter 3 describes a combined haemodynamic system (CHS) which predicts the response of the cerebral vasculature to changes in arterial blood pressure,

arterial CO_2 concentration and neural stimulation. Dynamic simulations of the model under different conditions show that there is significant interaction between the autoregulation and activation processes. In order to relate the model to the mathematical relationships estimated directly from clinically measurements, ABP and cerebral blood flow velocity (CBFV) measured in the middle cerebral artery using TCD, the linear part of CHS is derived, which closely approximates a second order system for typical values of physiological parameters. The model parameters can thus be optimally estimated from available experimental data for the Impulse Response (IR), yielding physiologically reasonable values.

Chapter 4 demonstrate how multivariate system identification can be used to analyse the regulation of CBFV of healthy human subjects by fluctuations in ABP, end-tidal CO_2 partial pressure fluctuations (P_{ETCO_2}) and end-tidal O_2 fluctuations (P_{ETO_2}) and how these additional inputs, P_{ETCO_2} and P_{ETO_2} , can account for higher coherence values at low frequencies where univariate coherence between ABP and CBFV is always low. A simulation study, using models described in Chapter 3, will be used to illustrate why univariate system identification methods fail to perform when additional inputs are not accounted for.

Chapter 5 will show how the wavelet phase synchronization method can be used to investigate the time-varying phase relationship between ABP and $CBFV$, thus relaxing the strict assumption of stationarity imposed by use of the Fourier transform. The fluctuations of P_{ETCO_2} are also showed to have effects on the instantaneous $ABP - CBFV$ phase relationship and the CO_2 effects can be removed by using a correction term representing the CO_2 contribution to $CBFV$ variations, identified by a multivariate system identification method, as proposed in Chapter 4.

Chapter 6 will propose wavelet cross-correlation as a method of analysing frequency dependent coupling, which will be applied to investigate age-dependency and posture-dependency of the coupling between cerebral haemodynamics and systemic cardiovascular dynamics. This will demonstrate how the discrete wavelet cross-correlation can localise this coupling

to a particular frequency band around 0.1Hz, where low frequency oscillations occur.

The wavelet-based signal processing techniques described in Chapter 5 and Chapter 6 are then used to quantify the contribution of CO_2 variations in the baseline BOLD fluctuations of both eyesopen and eyesshut cases. The advantage of these techniques will be illustrated by comparing with the classical correlation coefficient and regression analysis methods.

The final chapter, Chapter 8 will draw together the findings of Chapter 3-7 and suggests future research directions.

Literature review

2.1 Introduction

Chapter 1 has outlined the significance of understanding the maintenance and regulation of blood flow and oxygen supply in the human brain. Without the mechanisms that regulate cerebral blood flow (CBF), abnormally low or excessive CBF can lead to cerebral ischemia, intracranial hypertension or even capillary damage, thus contributing to the onset of cerebrovascular events. As a result, both the classification and assessment of CBF regulation become important steps in the diagnosis of many clinical conditions. They have thus has been the subject of intensive study as shown by the very large literature.

This Chapter, therefore, will first summarise clinical studies of cerebral autoregulation, focussing on the available measurements, autoregulation status and physiologic modulation. The second part of this chapter then addresses the mathematical analysis of the cerebral system, including both physiologically-based modelling and data-driven modelling, as well as signal processing algorithms.

2.2 Control of cerebral blood flow

As mentioned in Chapter 1, the brain is the most energy-consuming organ in the human body, requiring sufficient, yet not excessive, blood flow and oxygen supply in accordance

with its underlying functional or metabolic needs. Thus, numerous regulatory mechanisms are involved in the delicate control of cerebral blood flow. These CBF regulatory mechanisms can be separated into the central cardiovascular control mechanism and cerebral autoregulation.

2.2.1 Central cardiovascular hemodynamics

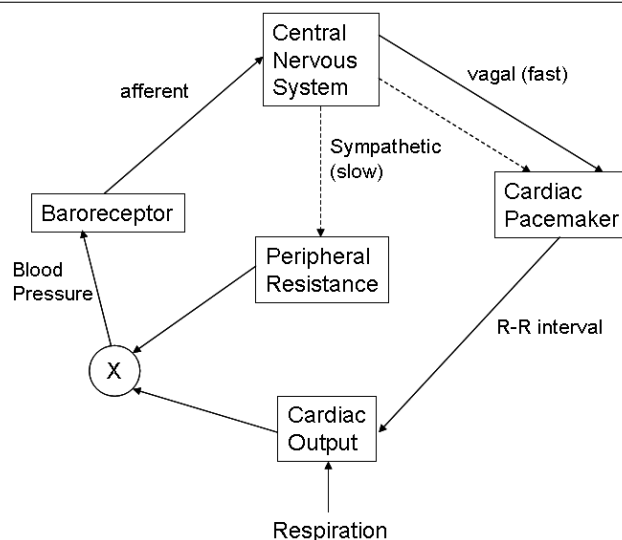
The left ventricle primarily generates the energy for the systemic circulation (Priebe (1999)). Changes in heart rate, myocardial contractility, peripheral resistance and venous return also affect cerebral circulation. All these factors are tightly regulated to maintain the required mean arterial blood pressure (ABP) and cardiac output (CO) to satisfy adequate blood perfusion in the brain and all other body organs.

Among all these regulation mechanisms, the principal short-term ABP regulator is the baroreflex, which is a negative feedback system based on multiple pathways, as illustrated in Figure 2.1. The baroreceptors, mainly located in the carotid sinuses and aortic arch, are sensitive to changes in ABP. They then communicate this information to the cardiovascular control centre to counteract the ABP change. The sympathetic nervous system is then activated to adjust heart rate and ventricle contractility as well as peripheral resistance in order to restore ABP back towards its baseline value.

The baroreflex plays an important role in maintaining blood pressure at a relatively constant level during daily orthostatic manoeuvres (such as getting up/standing up and laying/sitting down). Maintaining adequate blood pressure provides the first line of defense of the cerebral circulation against hypo- or hyperperfusion.

2.2.2 Cerebral autoregulation

Cerebral autoregulation serves as the next line of defense by helping to maintain relatively constant CBF despite variations in cerebral perfusion pressure (CPP) (the difference between ABP and intracranial cerebral pressure (ICP)), first defined in Lassen (1959) (Lassen

Figure 2.1 Schematic diagram of the baroreflex. Adapted from deBoer et al. (1987).

(1980)). Blood flow in a series of blood vessels is determined by the drop of blood pressure divided by the resistance, a dynamic change primarily caused by the vasodilation or vasoconstriction of arterioles. For example, as the pressure drops, these blood vessels will dilate resulting in a decrease of the cerebral vascular resistance which then helps to maintain a near constant blood flow.

Due to this negative feedback loop, cerebral autoregulation enables a tight coupling between CBF/oxygen supply and the metabolic demand of the brain to be maintained and thus plays an essential role in maintaining normal brain function. Details of its assessment in both normal and various pathophysiological conditions will be addressed in the following chapters.

2.3 Clinical studies of autoregulation

The assessment of cerebral autoregulation is important for rational clinical management of specific conditions, such as severe head injury, acute ischemic stroke or subarachnoid haemorrhage, which are known to abolish autoregulation (Paulson et al. (1990); Bouma and Muizelaar (1992)). Patients whose autoregulation is impaired or abolished are very vulnerable to pressure changes and are thus at much greater risk of cerebral ischaemia or

secondary brain damage due to hyperfusion. These patients require much greater control of fluctuations in CPP in order to prevent harmful haemodynamic consequences of therapeutic interventions (Panerai (1998)).

2.3.1 Key measurement techniques

According to the definition of cerebral autoregulation, the goal of research performed on human cerebral autoregulation is essentially to estimate the extent to which cerebral vascular resistance is actively modified in order to keep relatively constant blood flow (and hence oxygen supply) despite changes in perfusion pressure. As a result, the assessment of autoregulation status requires accurate measurements of both CPP and CBF, the key variables involved in autoregulation mechanism. It is worth to make it clear that the target of cerebral autoregulation is differing in ischemia and haemorrhage: cerebral oxygenation, which is directly related to brain metabolic rate, will be key variables which require continuously monitoring in ischemic case (CBF is only a surrogate variable for cerebral oxygen); while in haemorrhage case, the quantity of cerebral blood flow becomes the most crucial variable. Among the current conventional measurements of blood flow and oxygenation presented below, Transcranial doppler is target at measuring blood flow supply in the brain, while the other two measurements, Near infrared spectroscopy and Blood oxygen level-dependent functional MRI are both focused on cerebral oxygenation level.

Measurement of cerebral blood flow and blood oxygenation

Early studies of cerebral autoregulation often used indicator-dilution methods, including inert gases such as N_2O , ^{85}Kr or ^{133}Xe , to estimate CBF in humans (Ingvar and Lassen (1965); Lassen (1959, 1974); Torizuka et al. (1971)). These methods provide a value of the average CBF in units of ml of blood per 100 g of tissue per minute, but to obtain absolute blood flow it is necessary to estimate the total brain weight. Moreover, each CBF measurement with ^{133}Xe takes 15 minutes (as the clearance of ^{133}Xe takes around 9 to 12 minutes (Torizuka et al. (1971))). Since it also requires the injection or inhalation of a radioactive

indicator, the total number of observations in a single subject is very limited. This clearly precludes any measurement of the temporal dynamics of cerebral autoregulation and thus the technique can only be used for studies of steady state autoregulation.

Transcranial doppler (TCD) ultrasound provided a new technique for non-invasively examining the intracranial arteries supplying the human brain, utilising the Doppler shift to detect the velocity of red blood cells in large blood vessels (Aaslid et al. (1982)). TCD allows continuous measurements to be made of cerebral blood flow velocity (CBFV), usually in the middle cerebral artery (MCA), with sufficient time resolution to capture dynamic variability in the signal, and thus permitting studies to be made of the temporal dynamics of cerebral autoregulation. The advantage of non-invasiveness and high time-resolution led to TCD becoming the most commonly used method for measuring cerebral blood flow in autoregulation studies (Panerai (1998)). However, to convert changes in CBFV to those in CBF requires an additional assumption to be made that the vessel cross-sectional area (CSA) remains stable during the examination. Consequently, one of the most discussed issues in cerebral hemodynamics is whether the large cerebral arteries-especially the MCA should be considered as rigid tubes or whether they possess dilatatory properties that come into play during CBF variations (Edvinsson et al. (1992)). Several investigations in humans suggest that the diameter of the middle cerebral artery, and other large cerebral vessels, remains relatively constant despite changes in ABP and blood gases (Hansen et al. (1983); Greisen et al. (1984); Giller et al. (1993); Poulin and Robbins (1996), though concerns about this assumption have arisen under sympathetic stimulation or the infusion of drugs (Panerai (1998)).

Near infrared spectroscopy (NIRS) is a relatively new method for the measurement of cerebral hemodynamics, first outlined by Jöbsis (1977). It is an optical approach utilising light in the near infrared region of the spectrum (700-1000nm), which can penetrate up to 8cm of biological tissue (Cope (1991)), to monitor changes in the oxygenation of the brain. Light attenuation within tissue involves two main compartments, (i) the absorbers whose concentration are fixed during the measurement period and (ii) the chromophores whose

concentration (and therefore light absorption) vary with time or with oxygenation status, such as oxyhaemoglobin (O_2Hb), deoxyhaemoglobin (HHb), and oxidised cytochrome oxidase ($CtOx$) (Elwell (1995)).

Changes in the concentration of these chromophores can be quantified by the modified Beer-Lambert law (MBL) (Delpy and Cope (1997)):

$$A = \log \frac{I_o}{I} = \alpha \cdot c \cdot d \cdot B + G, \quad (2.1)$$

where A is the optical density attenuation, I_o the incident light intensity, I the detected light intensity, α the absorption coefficient of the chromophore, c the concentration of chromophore and d the geometrical distance between light emitter and light receiver. B is the different pathlength factor (DPF) used to account for the increased pathlength due to scatter (dimensionless) and G represents tissue absorption, which is assumed to be constant during the measurement period.

Without the *absolute* value of G , equation 2.1 cannot be solved to provide a measure of the *absolute* concentration of the chromophore in tissue, however with the assumption that G remains constant, the *changes* in the concentration of the chromophore (Δc) can be determined by the *changes* of light attenuation (ΔA), for given values of B , d and α , which can actually be measured:

$$\Delta A = \Delta c \cdot \alpha \cdot d \cdot B \quad (2.2)$$

In order to determine the concentration changes of three chromophores, O_2Hb , HHb and $CtOx$ in the brain, the light attenuation at multiple NIR wavelengths needs to be measured (for example the Hamamatsu Photonics NIRO 500 uses 4 wavelengths (Elwell (1995))). Through a matrix operation which incorporates the absorption coefficients for each wavelength and chromophore, changes in chromophore concentration can be calculated from the measured attenuation, as shown in Equation 2.3 (full details can be found in Elwell (1995)):

$$\begin{bmatrix} \Delta A_{\lambda_1} \\ \Delta A_{\lambda_2} \\ \Delta A_{\lambda_3} \\ \Delta A_{\lambda_4} \end{bmatrix} = d \cdot B \cdot \begin{bmatrix} \alpha_{O_2Hb, \lambda_1} & \alpha_{HHb, \lambda_1} & \alpha_{CtOx, \lambda_1} \\ \alpha_{O_2Hb, \lambda_2} & \alpha_{HHb, \lambda_2} & \alpha_{CtOx, \lambda_2} \\ \alpha_{O_2Hb, \lambda_3} & \alpha_{HHb, \lambda_3} & \alpha_{CtOx, \lambda_3} \\ \alpha_{O_2Hb, \lambda_4} & \alpha_{HHb, \lambda_4} & \alpha_{CtOx, \lambda_4} \end{bmatrix} \cdot \begin{bmatrix} \Delta O_2Hb \\ \Delta HHb \\ \Delta CtOx \end{bmatrix}. \quad (2.3)$$

NIRS relies on the biochemical specificity of the signal and it is completely noninvasive, giving it the potential for measuring at the bedside (Elwell et al. (1994)), where it has been widely used for monitoring the brains of new-born infants (Duncan et al. (1995); Bortfeld et al. (2007)). Recently, it has also been used to detect changes in Hb oxygenation with functional brain activation at a low spatial resolution, termed functional NIRS (MacIntosh et al. (2003); Toronov et al. (2003); Huppert et al. (2005)). However, because of the poor depth penetration of NIRS, concerns have been expressed in the literature about a potential contaminating signal generated by extracranial tissues in the NIRS measurements (Kirkpatrick et al. (1998); Al-Rawi et al. (2001)). This extracranial contamination is important to consider in autoregulation studies when using NIRS since the aim is to investigate the coupling between cerebral hemodynamics and systemic variables. Extracranial blood flow (such as skin flow) might follow systemic changes with a regulation mechanism different from that of cerebral autoregulation.

Blood oxygen level-dependent (BOLD) fMRI is also a measure of blood oxygenation. It is based on the fact that HHb is paramagnetic whereas O_2Hb is diamagnetic. Hence, an increase in the concentration of HHb alters the local magnetic susceptibility, creating magnetic field distortion within and around blood vessels and producing a positive alteration in local MR signal, known as BOLD response (Ogawa et al. (1990); Kwong et al. (1992)).

Similar to NIRS, fMRI also utilises the signal intrinsic to the brain rather than signals originating from an exterior stimulus; consequently, repeated observations can be made on the same individual, providing a major advantage over other imaging methods. Owing to its superior spatial resolution (currently about 2 or 3 millimetres) and good temporal resolution (about 1 second), BOLD-based fMRI has been widely used to map brain function (Purves et al. (1997)). However, the effects of systemic changes on BOLD signal have been little investigated and the results are controversial and potentially conflicting. For example, both Wang et al. (2006) and Liu et al. (2006) have investigated the effects of ABP on BOLD response, drawing different conclusions: Wang et al. (2006) have identified a correlation between BOLD signal and ABP time series whereas Liu et al. (2006) found that ABP

changes do not affect either the global or regional BOLD response. These different results could be due to different experimental methodology, since Liu et al. (2006) studied BOLD response to baseline ABP change whilst Wang et al. (2006) were focused on dynamics of ABP and BOLD signal. Similar controversy has also arisen for the relationship between the local BOLD signal and the global BOLD signal modified by different CO_2 levels. An attenuation of the regional BOLD (rBOLD) response after the inhalation of 5% CO_2 has been found Bandettini and Wong (1997) and Cohen et al. (2002), yet a constant rBOLD was suggested by Corfield et al. (2001). A more complicated dependence of the regional BOLD signal on the global signal was suggested by Kemna and Posse (2001) and Posse et al. (2001), with an increased BOLD response in mild hypercapnia ($ET_{CO_2} < 50mmHg$) with a decrease at higher ET_{CO_2} levels. These controversies could be due to nonlinearities in the BOLD response, which is a major complication in explanations of the BOLD signal in clinical settings.

Measurement of cerebral perfusion pressure

CPP is normally expressed as the difference between systemic mean ABP and ICP (Paulson et al. (1990)). Under normal conditions ICP will be low and CPP can be approximated by mean ABP corrected for height of the head (Lassen (1959)). However, in severe head injury, ICP is elevated, or varies dramatically within minutes, as a result of hydrocephalus, in which case its measurement becomes essential for the correct estimation of CPP as $ABP - ICP$.

In earlier static autoregulation studies, the most common method of measuring ABP was with an intravascular catheter (Panerai (1998)). Though it is undoubtedly the most accurate technique for measure ABP, it is an invasive method that limits its application in clinical settings, especially for normal subjects. The Finapres device, alternatively, provides a non-invasive recording of the continuous ABP waveform based on the principle of arterial volume clamping (Molhoek et al. (1984); Parati et al. (1989)), which could facilitate the incorporation of autoregulation testing into routine clinical practice. However, assessment

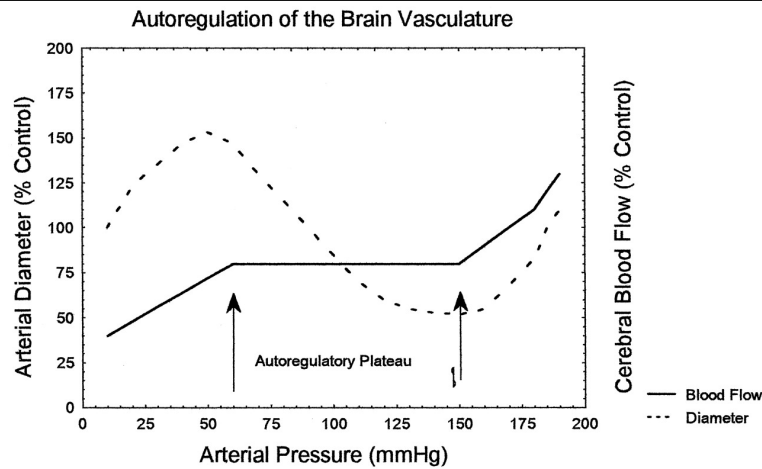
of autoregulation based on methods which induce large changes in mean ABP might also lead to changes in cardiac output which might then affect the pressure drop between the site of measurement and the large cerebral vessels, making it inaccurate to estimate ABP by this non-invasive method (Treib et al. (1996)). Birch and Morris (2003) also expressed the suspicion that peripheral vasoaction caused by sudden thigh cuff release may distort the measurement of blood pressure with the Finapres. However, a recent published paper (Panerai et al. (2008)) has investigate the influence of non-invasive Finapres device on the dynamic cerebral autoregulation identification by comparing to blood pressure recorded in the ascending aorta. Highly correlated result between the two different measurements proves the reliability of the Finapres device in autoregulation assessment.

2.3.2 Static cerebral autoregulation curve

Static autoregulation studies only look at the relationship between mean CBF and CPP (or mean ABP in most cases) (Panerai (1998)). They do not consider the time course of changes in flow following changes in pressure, which belongs to the scope of dynamic autoregulation studies and is addressed below. The basis of this static approach is the classical autoregulation curve, shown in Figure 2.2, which describes the active response of cerebrovascular resistance arteries (dilating during ABP decrease and constricting during ABP increases), thus maintaining relatively constant levels of CBF over a fairly broad range of ABP (Lassen (1959); Paulson et al. (1990)). However, it should be noted that the autoregulation plateau region does not necessarily have a zero slope (Rosenblum (1995); Panerai et al. (1995b); Ursino et al. (1995))

When arterial pressure exceeds the limits of the autoregulation plateau, cerebral resistance arteries respond passively and CBF increases or decreases passively with further increases or decreases in ABP. Thus, the critical levels of ABP are defined as lower and upper limits of CBF autoregulation: reduction of ABP below the lower limit results in hypoperfusion of the brain and cerebral ischemia, whilst further increases of ABP above the upper limit lead to hyperperfusion and possible disruption of the blood-brain barrier.

Figure 2.2 The ideal response of cerebral vasculature and mean blood flow to changes in mean arterial pressure. Adapted from Jennings (2003).



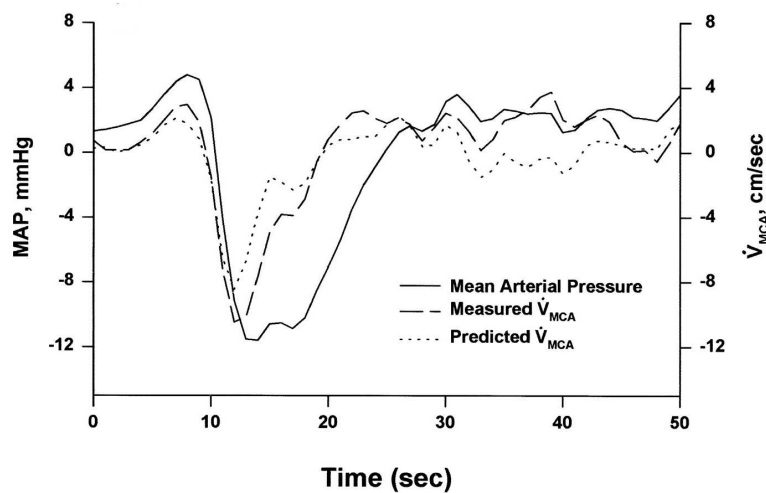
Owing to the clinical importance of both limits, a number of studies have attempted to locate the position of the lower or upper limit of autoregulation or shifts in the autoregulation curve due to changes in other physiological parameters (a comprehensive review can be found in Panerai (1998)). Among these assessments of static autoregulation, the most common approach used to induce changes in mean ABP is the infusion of drugs which do not have effects on cerebral vasculature or metabolism (Lassen (1959); Olesen (1972); Lassen (1974); Paulson et al. (1988)). Other methods include blood volume displacement such as head-up tilting (Jrgensen et al. (1993)), lower body negative pressure (Bondar et al. (1994)), surgery (Lundar et al. (1985)) and sleep studies (Balfors and Franklin (1996)). However, for the investigations that induce large changes in mean ABP, it is very possible that parallel shifts would take place in other physiological variables that might also have a strong influence on CBF, which is the main concern with this static approach (Panerai (1998)).

2.3.3 Dynamic cerebral autoregulation

Interest in the dynamics of cerebral autoregulation directly followed the availability of Transcranial Doppler ultrasound which provides excellent temporal resolution for measuring CBF. Studies of dynamic autoregulation are more concerned with the characterisation

of the temporal dynamics of CBF responses to a change in pressure than the absolute value of time-averaged changes. In 1989, Aaslid et al. introduced the thigh cuff technique to invoke a sudden drop in ABP and found that the active CBF response started within approximately 2 seconds, and recovered within 10-15 seconds, as shown in Figure 2.3.

Figure 2.3 Dynamics of cerebral autoregulation during thigh cuff test. All tracings are shown in values relative to control prerelease values. Adapted from Zhang et al. (1998a).



Compared to traditional steady-state autoregulation studies, this dynamic autoregulation test is not time-consuming and, when coupled to the use of non-invasive measurements of blood pressure, can be easily repeated (Aaslid et al. (1989); Birch et al. (1995); Panerai et al. (1996)). More importantly, the short time interval required to perform dynamic tests minimises the influences of other variables such as CO_2 or mental activation, which can compromise assessments based on static methods as discussed previously. As a result, this dynamic approach has become a favorable choice for clinical assessment of autoregulation and has thus been studied extensively in the literature (Aaslid et al. (1989, 1991); Tiecks et al. (1995); Zhang et al. (1998a); Panerai et al. (1999, 2001)).

2.3.4 Autoregulation Stimuli

Measurement of cerebral autoregulation requires a change in blood pressure, which can either be forced or naturally occurring. The type of stimuli can be split into those that intro-

duce a large step change in pressure and follow the dynamic time course of cerebral blood flow (dynamic autoregulation), or look at its steady state value (static autoregulation) and those that investigate the dynamics of the response to spontaneous fluctuations (dynamic autoregulation).

Drug infusion was widely used in early static studies of autotregulation, as well as some dynamic autoregulation studies (Panerai (1998)). For example, ABP can be increased by the infusion of phenylephrine (Tiecks et al. (1995)), angiotensin or noradrenaline and decreased by the infusion of sodium nitropusside or thrimethapan. However, the uptake of a drug has its own temporal dynamics in humans, which clearly makes it difficult to interpret dynamic responses to a drug. Also, for ethical reasons repeated studies are unlikely to be approved.

Besides drugs, changes in cerebral perfusion pressure can also be achieved by changing pressure in the lower limbs, either through changes in posture or through the inflation/deflation of thigh cuffs. This results in a large step change in pressure, which is, again, unethical for some patient groups, such as subjects with severe peripheral disease (Tiecks et al. (1996)). The inflation of thigh cuffs can be quite painful and concerns have been raised that it might produce sympathetic activation (Panerai (1998)). It is also likely that parallel shifts of other physiological variables will take place, and unless these shifts are monitored this will severely impact the repeatability of the results. Other studies have attempted to overcome this difficulty by investigating the CBF response to forced periodic variations in pressure, such as sinusoidal changes in lower body pressure (Birch et al. (2002); Liu et al. (2003)), periodic posture changes due to periodic squatting (Birch et al. (1995)), or periodic blood gas changes due to periodic deep breathing (Diehl et al. (1995)). These techniques require repetition of the test, which can significantly reduce the level of noise present; however sinusoidal lower body negative pressure is not suitable for some patients, and periodic squatting or deep breathing require a certain level of fitness that cannot be guaranteed in all clinical subjects (Rowley (2008)).

As mentioned above, the techniques adopted to stimulate either step changes or slow oscillation in ABP all have inherent problems in the clinical assessment of dynamic autoregulation. It would thus be ideal if the spontaneous fluctuations in ABP could be used to assess the dynamic performance of cerebral autoregulation.

Slow spontaneous variations in cerebral hemodynamics and metabolism have been observed under a wide range of experimental conditions (a comprehensive summary of which can be found in Obrig et al. (2000)). Though the underlying mechanisms of these oscillations are not clear, they are found to share several common features: (1) they occur without any external stimulus (spontaneity); (2) they can be differentiated from other oscillations such as heart beat (slowness); (3) they have been found to be altered by pharmacological and pathological conditions (modulatability).

These oscillations can be decomposed into different fluctuation components by their different spectral features. Variability around $0.3Hz$, termed respiratory sinus arrhythmia (RSA), is observed in NIRS measured O_2Hb , HHb and total hemoglobin (tHb) and also in ABP . Numerous theories have been proposed for the presence of this variability in blood pressure and cerebral haemodynamics. Innes et al. (1993) proposed that changes in pressure in the chest provoke changes in cardiac stroke volume through the baroreflex, contributing to respiratory frequency pressure variability in humans (Cohen and Taylor (2002)). This is, however, controversial as variability at $0.3Hz$ has been reported to occur in direct synchrony with respiratory sinus arrhythmia, suggesting that both oscillations could have a central vagal origin (deBoer et al. (1987); Taylor and Eckberg (1996)).

Oscillations at a lower frequency, around $0.1Hz$, are also observed in cerebral haemodynamics, being termed low-frequency oscillations (LFOs). Hudetz et al. (1992) report oscillations in CBF measured using laser doppler flowmetry (LDF) within a frequency range of $0.06 - 0.1833Hz$ in anaesthetized rats when blood pressure is held constant below $90mmHg$. Mayhew et al. (1996) used reflected light imaging to investigate $0.1Hz$ oscillations in the exposed cerebral cortex of rat and cat. Obrig et al. (2000) demonstrated that similar oscil-

lations can be captured noninvasively in the human brain using NIRS to measure cerebral oxygenation and Elwell et al. (1999) underlined the implications of these oscillations for functional activation studies.

Within the same frequency band, high variability in ABP and HR is also found. These oscillations, called Mayer waves (Mayer (1876)), originate from the action of the baroreflex in the systemic regulation of the cardiovascular system, and can be ascribed to sympathetic nervous activity (Nilsson and Aalkjaer (2003)). Since the cerebrovascular system is a one part of the systemic circulation, it is mediated by both central sympathetic activation and local myogenic or metabolic mechanisms (Priebe (1999)). It is thus very unlikely that LFOs found in cerebral hemodynamic variables are completely independent of their cardiovascular counterparts. Indeed, it has been shown in Katura et al. (2006) that one third of cerebrovascular oscillations in the range of 0.04-0.15 Hz can be tracked back to the systemic cardiovascular fluctuations (HR and ABP) in the same frequency band. Though information transfer entropy used in Katura et al. (2006) is able to assess not only the coupling but also the causality between two variables, it is still not clear how to convert transfer entropy results into the percentage of information transfer from cardiovascular oscillations to cerebrovascular oscillations. Fluctuations in HR ($< 0.1\text{Hz}$) have also recently been identified as an important source of variance in the resting-state fMRI BOLD signal (Shmueli et al. (2007)).

Cerebral autoregulation status can be assessed by considering the bivariate relationship between these resting state fluctuations in systemic variables (primarily ABP) and those related to cerebral hemodynamics (CBFV or O_2Hb) (Zhang et al. (1998a,b); Panerai et al. (1999, 2001)). This assessment method makes best use of the available data from modern, noninvasive measurement techniques, and does not require the use of a strenuous, painful, or even dangerous stimulus, but considerable controversy exists in the literature about the origin and interpretation of these spontaneous fluctuations. These problems are compounded by the fact that the relationship between ABP and CBF is not purely controlled by pressure autoregulation, but also influenced by changes of other physiological

variables such as blood gas tension or functional activation (Latka et al. (2005); Panerai et al. (2005))(This issue will be revisited in detail below). As a result, in dynamic autoregulation studies based on spontaneous fluctuations, sensitive and verifiable data analysis techniques are required to avoid making false conclusions about the autoregulation status.

2.3.5 Physiological modulation of autoregulation

As mentioned above, ABP is not the only determinant of CBF. Other parameters such as arterial gas tension, primarily arterial CO_2 tension ($PaCO_2$) and arterial oxygen tension (PaO_2), have vasodilatory or vasoconstrictory effects on cerebral vessels and thus influence blood flow, this effect being known as cerebrovascular reactivity (Edvinsson et al. (1992)). In humans, 5% and 7% CO_2 inhalation raises CBF by approximately 50% and 100%, respectively (Kety and Schmidt (1948)). Poulin et al. (1996) and Poulin et al. (1998) also observed that there is a lag of around 6 seconds in CBFV changes measured in the middle cerebral artery in response to CO_2 changes. Besides CBF, CO_2 also affects pressure autoregulation status. It has been demonstrated that hypercapnia impairs autoregulation, whereas hypocapnia improves autoregulation (Aaslid et al. (1989); Birch et al. (1995)).

Besides blood gas reactivity, autoregulation status has also been found to be altered by various pathological and pharmacological conditions. It has been known for many years that sympathetic activation will shift the upper limit of autoregulation toward higher pressures, whereas acute denervation may shift the limits of the autoregulation toward lower blood pressure levels (Bill and Linder (1976); Edvinsson et al. (1976)). More recently, Panerai et al. (2001) found that the instantaneous $ABP - CBFV$ relationship was dependent on the choice of manoeuvre, suggesting that differing dynamic autoregulation status associated with different degrees of sympathetic activation. Hypertension and ageing are both found to shift the lower limit of autoregulation to a higher level of pressure, which makes hypertensive patients and elderly people more susceptible to ischemic stroke (Strandgaard et al. (1973); Wollner et al. (1979)).

2.4 Analysis of clinical autoregulation data

2.4.1 Assessment of static autoregulation

The earliest static studies of cerebral autoregulation relied entirely on the absolute values of CBF and ABP, in comparison with the static cerebral autoregulation curve (figure 2.2). This is mainly due to the fact that CBF data obtained using inert indicator washout techniques were severely limited, as discussed in Section 2.3.1. Few studies attempted to reproduce the entire autoregulation curve. Most commonly, investigators induced changes in mean ABP to determine whether a particular group of patients showed active autoregulation or not. In most cases, only two measurements were collected for each individual, before and after a change in ABP (Panerai (1998)). Some studies use an index of static autoregulation ($sARi$) (Bouma and Muizelaar (1990, 1992); Bouma et al. (1992); Strebel et al. (1995)), defined as:

$$sARi = \% \Delta CVR / \% \Delta ABP \quad (2.4)$$

where the cerebrovascular resistance, CVR is given by $CVR = \frac{ABP}{CBF}$. However, estimation of an autoregulation curve from two data points is highly questionable (Panerai (1998)).

Studies which performed more than two measurements adopted linear regression to quantify the relationship between CBF and mean ABP and to recover the slope for the autoregulation curve, which can be used as an objective parameter to assess the static performance of autoregulation. This group of studies includes the use of regression to decide the position of the lower limit or upper limit, or both, of the autoregulation curve (Schmidt et al. (1990); Larsen et al. (1994); Olsen et al. (1996); Strandgaard et al. (1973); Strandgaard (1976)). If the slope is approximately zero, it can be assumed that linear regression coincides with the plateau region of a normal autoregulation curve (figure 2.2). If the slope is significantly positive, this can either represent the linear portion of the curve beyond its autoregulation range (below its lower limit or above its upper limit, see figure 2.2), or the central region of the curve when autoregulation is impaired. Both possibilities represent the absence of active pressure autoregulation. Both correlation coefficient (γ) and averaged

CBF change as a percentage of mean ABP value can be obtained through linear regression analysis. Thresholds of $\gamma = 0.5$ or $0.5 - 4\%/mmHg$ have been proposed for the separation between normal and impaired autoregulation, respectively (Jorch and Jorch (1987); Pryds et al. (1990); Panerai et al. (1995a)). Although the linear regression method is the most reliable approach to study the static properties of autoregulation, both correlation coefficient and slope index would become meaningless if the regression is not statistically significant. As a result, a classification criterion based both on the significance (p -value) and the slope of regression has been proposed (Panerai et al. (1995a)).

The shortcoming of both $sARi$ and linear regression is that they do not take account of changes in other physiological variables which might also affect CBF during the test, as mentioned previously. To solve this problem, additional measurements were collected to monitor the simultaneous changes in P_{aCO_2} and P_{aO_2} and multiple regression analysis was used to compensate their effects (Buijs et al. (1992); Menke et al. (1993); Benders et al. (1995)). For the case of CO_2 , a related method is to correct CBF measurements using equations which describe CO_2 activity (Muizelaar et al. (1984); Schmidt et al. (1990); Olsen et al. (1996); Tominaga et al. (1976); Young et al. (1993)). The risk of not controlling for the effect of confounding variables was demonstrated by the study of Cencetti et al. (1997) where the CBF changes previously attributed to pressure changes in response to tilting (Brooks et al. (1989); Daffertshofer et al. (1991)) were actually partly produced by a reduction in P_{aCO_2} induced by posture change.

2.4.2 Assessment of dynamic autoeulation–mathematical models

Early dynamic studies often used the thigh cuff technique to induce a significant rapid change in ABP and monitored the CBF response (Aaslid et al. (1989, 1991); Lagi et al. (1994); Strebel et al. (1995); Tiecks et al. (1995); Jünger et al. (1997)). With this approach, impaired autoregulation would suggest a mean $CBFV$ pattern passively following mean ABP time course, whereas normal autoregulation would show that $CBFV$ starts to return and reaches its baseline level much sooner than ABP . As a result, Aaslid et al. (1989)

introduced an index, 'rate of regulation (RoR)':

$$RoR = \frac{\Delta CVR}{\Delta ABP \times \Delta t}, \quad (2.5)$$

as a quantification for the speed of *CBFV* recovery and thus dynamic autoregulation status. The function Δ is used to represent changes about the experimentally measured baseline and Δt is the time over which the change is calculated. In Aaslid et al. (1989), *RoR* was measured as a function of P_{aCO_2} and a significant inverse relationship between P_{aCO_2} and *RoR* was demonstrated, suggesting differing autoregulation status. *RoR* was also used to characterise cerebral autoregulation dynamics by Steiger et al. (1994); Newell et al. (1996); Smielewski et al. (1996).

Tiecks et al. (1995) proposed a second order differential equation to model the *CBFV* response to the *ABP* drop provoked by the thigh cuff technique. The equation involves three parameters: an autoregulatory gain, K , a damping factor, D , and a time constant, T . These three parameters were grouped to provide a ten-level autoregulation index, *ARI*, with a value of $ARI = 0$ representing total absence of autoregulation, and a value of $ARI = 9$ corresponding to very efficient autoregulation response (Tiecks et al. (1995)). In clinical settings, the value of *ARI* was determined from the *CBFV* response to pressure change by finding which value of *ARI* provided the best fitted model response to the measured data (Tiecks et al. (1995, 1996); White and Markus (1997)). This dynamic autoregulation index was found to be highly correlated to the static autoregulation index, *sARi* (Tiecks et al. (1995)).

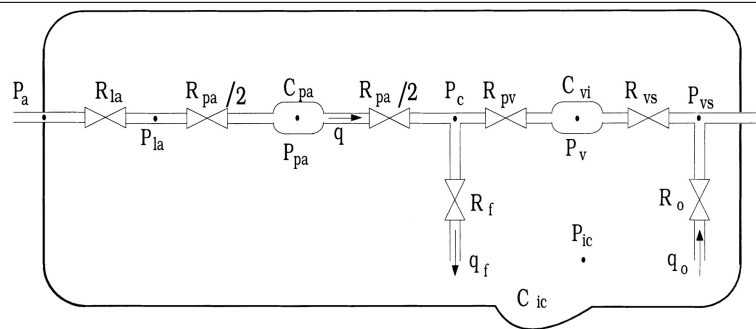
The dynamic autoregulation models presented in Aaslid et al. (1989) and Tiecks et al. (1995) are two typical examples of linear models of autoregulation which relate measured time series to indices representing autoregulation status. Both of them are 'signal-based', recovering model parameters directly from data, yet encapsulating the authors' hypothesis of the dynamics of cerebral autoregulation, such as linearity, with model parameters being physically meaningful, such as cerebrovascular resistance in Aaslid et al. (1989) and time constant in Tiecks et al. (1995). The development of subsequent mathematical models

can then be approximately divided into two approaches. One aims to estimate the purely mathematical relationship between different clinical variables, including Mx autoregulation index (Czosnyka et al. (1996, 1997, 2001); Reinhard et al. (2005)), ARX model (Liu et al. (2003)), impulse response of transfer function analysis (Zhang et al. (1998a); Panerai et al. (1999, 2001)), linear Wiener-Laguerre model (Panerai et al. (1999, 2001); Mitsis et al. (2002)), and second-order Volterra kernels (Panerai et al. (1999); Mitsis et al. (2002, 2004b)). ARX models, impulse response and linear Wiener-Laguerre models are all linear, which cannot explain some aspects of cerebral hemodynamics such as the spontaneous oscillations observed in CBFV and some of them fit data poorly (Giller and Mueller (2003)). Second-order Volterra kernels do not make a linear assumption of $ABP - CBFV$ relationship and are able to characterize nonlinearities in cerebral autoregulation. However, it is hard to gain physical insights from this non-parametric approach (Giller and Mueller (2003)). Mx index of autoregulation is calculated as the correlation coefficient between spontaneous fluctuations in CBFV and ABP over a 3 minute moving window. The advantage of using windowed correlation is that it does not assume that the coupling relationship remains constant with time; this is important when clinical interventions are being carried out, since it is important not to miss or to average out deterioration that may occur in the middle of a test. A recent study (Czosnyka et al. (2008)) shows that Mx agrees well with traditional ARI in diagnosing impaired autoregulation status for head-injured patients.

The second approach relates different clinical parameters through models based on physiological assumptions, for example modelling nonlinearities from tissue elasticity and interactions with intracranial pressure (the extravascular pressure of cerebral vessels), as shown in Figure 2.4. Examples include Ursino and Lodi (1997, 1998); Lodi et al. (1998); Ursino et al. (2000); Payne (2006); Banaji et al. (2005). Many of the variables in such models cannot be measured directly and hence attempts have been made to perform least square fits of some model parameters to clinical data (Ursino et al. (1995); Ursino and Lodi (1997)); however the large number of parameters involved makes such parameter fits computationally intensive and ill-posed for short records of clinical data and hence difficult to

validate the model. As a result, these physiologically-based models are now more applied to theoretically test hypotheses about complex interacting systems (for example, the interaction between pressure autoregulation and CO_2 reactivity in Lodi et al. (1998); Ursino and Lodi (1998); Ursino et al. (2000); Payne (2006); the interaction between autoregulation, CO_2 activity and neural activation and hence BOLD response in Payne (2006)), and less used in a clinical setting for diagnosis of cerebral autoregulation.

Figure 2.4 Biomechanical analog of the dynamic cerebral autoregulation model: P_a , systemic arterial pressure; P_{la} and R_{la} , pressure and resistance of large intracranial arteries, respectively; P_{pa} , R_{pa} , and C_{pa} , pressure, resistance, and compliance of pial arterioles, respectively; P_c , capillary pressure; q , tissue cerebral blood flow; R_{pv} , resistance of proximal cerebral veins; C_{vi} , intracranial venous compliance; P_v , cerebral venous pressure; P_{vs} and R_{vs} , sinus venous pressure and resistance of the terminal intracranial veins, respectively; R_f and R_o , cerebrospinal fluid (CSF) formation and CSF outflow resistance, respectively; q_f and q_o , CSF formation rate and CSF outflow rate, respectively; P_{ic} and C_{ic} , intracranial pressure and intracranial compliance (taken from Ursino et al. (2000) with permission).



Payne and Tarassenko (2006) proposed a combined analysis to link the complex physiologically-based models to experimentally-derived models, which is the first attempt to bridge the gap and thus take the advantage of both approaches. This combined analysis is able to estimate autoregulation status clinically as well as helping to provide physiological insights into the processes that govern cerebral autoregulation. The linearised process used by Payne and Tarassenko (2006) provides a dimensionality reduction of the original complex nonlinear model and thus can be used to recover some variables from the available experimental data through the simplified parameter fitting process. On the other hand, the model simulations are able to recover some key features of the clinical measurement and thus help to understand and interpret the data. As a result, a combined analysis of physiologically-based

modelling and experimental data processing becomes a very attractive process and is used throughout the following Chapters.

2.4.3 Frequency domain analysis

As mentioned in Section 2.3.4, the techniques adopted to simulate step changes in ABP, such as the thigh cuff technique, have inherent problems that limit their clinical use. Techniques are now mainly focused on spontaneous oscillations in ABP, CBFV and blood gas levels, such as P_{aCO_2} and P_{aO_2} , which are well defined in their frequency content. It is therefore natural to use frequency-domain techniques to consider variations in signal power and the interrelationship between signals at different frequencies.

Typical frequency methods for investigating the regulation of cerebral haemodynamics include power spectra analysis under various physiological or pathological conditions. For example, Tachtsidis et al. (2004) reported that the frequency content of NIRS measured O_2Hb was dependent on posture in healthy young subjects. Schroeter et al. (2004) found that the power of low frequency oscillations around $0.1Hz$ in O_2Hb declines with ageing. However, large inter-subject variability are often found in these absolute measurements of power spectra, which makes statistical differences hard to achieve.

More sophisticated techniques, including system identification algorithms have been applied to investigate the bivariate relationship between systemic changes, such as ABP oscillations, and cerebral hemodynamics, $CBFV$ or O_2Hb variations. Transfer function analysis is a standard system identification technique, explained in detail in numerous texts, for example Ljung (1998). Here just an short outline of univariate transfer function analysis is present, with the specific details of practical implementation used in Chapter 4, including multivariate transfer function identification, outlined in that section.

From the time series for ABP , $P(t)$, and $CBFV$, $V(t)$, the frequency-domain transforms $P(f)$ and $V(f)$ are computed with the Fourier transform. Their autospectra, $G_{pp}(f)$ and $G_{vv}(f)$, and the cross-spectrum $G_{pv}(f)$ are estimated using a Welch periodogram (Welch

(1967)) as:

$$G_{pp}(f) = E[P^*(f)P(f)], \quad (2.6)$$

$$G_{vv}(f) = E[V^*(f)V(f)], \quad (2.7)$$

$$G_{pv}(f) = E[P^*(f)V(f)]. \quad (2.8)$$

The complex transfer function $H(f)$ between $P(t)$ and $V(t)$ is then given by:

$$H(f) = \frac{G_{pv}(f)}{G_{pp}(f)}. \quad (2.9)$$

Its absolute value and angle give the gain and phase shift of the system, taking $P(t)$ as the input and $V(t)$ as the output. The univariate coherence function $\Gamma_P^2(f)$ is estimated by:

$$\Gamma^2(f) = \frac{|G_{pv}(f)|^2}{G_{vv}(f)G_{pp}(f)}. \quad (2.10)$$

The squared coherence reflects the fraction of the output power that can be linearly related to the input power at each frequency. $\Gamma(f)$ is an assessment of accuracy in estimation of the transfer function coefficients, gain and phase; the values of the recovered system parameters are only valid where this coherence is high.

For a system that can be described by a univariate linear system of ordinary differential equations (ODEs) with constant coefficients, the Fourier transform of the output is related to the Fourier transforms of the input signals via a linear transfer function, with the gain describing how the two power spectra (input and output) are related, and phase characterising the phase shift between oscillations in the input signal and the output signal. In this case of a pure linear relationship between the input and output signals, $\Gamma^2(f)$ will be 1 at all frequencies, guaranteeing the accuracy of the identified transfer function coefficients. However, as shown in the physiologically-based models outlined above, the cerebral haemodynamic system is not a simple linear time-invariant system; actually it is nonlinear (due to tissue elasticity and interactions with intracranial pressure), time-varying (vasomotion¹ causing varying vessel radius and hence resistance) and multivariate (blood flow is not only

¹Rhythmic oscillations in vascular tone caused by local changes in smooth muscle constriction and dilation.

controlled by pressure change, but also influenced by blood gas concentrations). Therefore, the values of $\Gamma^2(f)$ calculated when assessing the real cerebral autoregulation system are always lower than 1 at some frequencies. Actually, a minimum value of $\Gamma^2(f) > 0.5$ is conventionally adopted to represent a significant linear association between the input and output at a certain frequency (Panerai et al. (1997)). The relationship between values of the coherence function and statistical confidence is explored in Panerai et al. (1997) and Wang and Tang (2004).

The first application of transfer function analysis of autoregulation was performed by Giller (1990) who estimated the amplitude frequency response (gain) and coherence function between spontaneous oscillations in *ABP* and TCD-measured *CBFV*. Giller demonstrated that patients with subarachnoid haemorrhage showed higher values of coherence than normal patients, indicating impaired autoregulation. Though this finding is consistent with the interpretation that active autoregulation reduces the degree of linear dependency between fluctuations in pressure and flow, it could also support the alternative conclusion of increased CO_2 or O_2 reactivity in patients with subarachnoid haemorrhage with equal validity, since oscillations in P_{aCO_2} and P_{aO_2} were not considered in the study. In fact, it has been shown that the impulse response, and thus transfer function, under hypercapnia can easily be classified into the group with abnormal autoregulation because of their similar pattern (Panerai et al. (1996)).

Since the publication of Giller (1990), numerous studies have used transfer function analysis for the recovery of the dynamics of cerebral autoregulation (Zhang et al. (1998a); Panerai et al. (1999, 2001); Oehm et al. (2003); Reinhard et al. (2001, 2003a,b, 2005)). Examination of transfer function coefficients (gain and phase) and coherence as a function of frequency is used to investigate cerebral autoregulation status. As shown in Figure 2.5, the estimated frequency response of the *ABP/CBFV* relationship below 0.50 Hz at normal autoregulation can be divided into three regions:

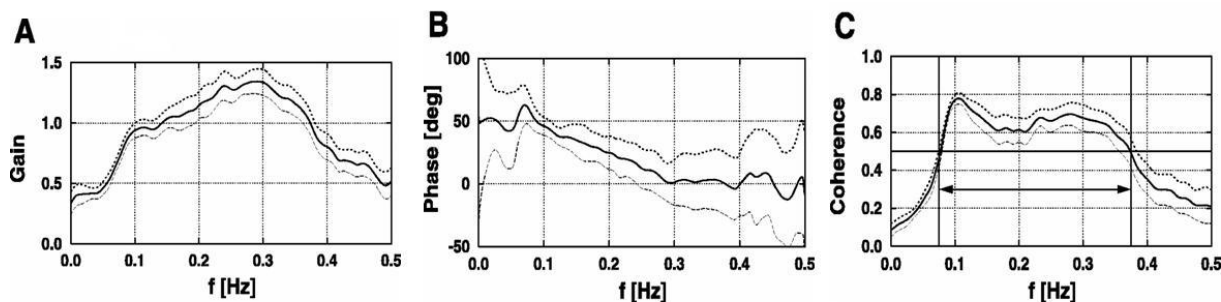
1. Low frequency (< 0.07 Hz): Low coherence, low gain and large phase lead.
2. Intermediate frequency (0.07 – 0.20 Hz): Increasing coherence, increasing gain and de-

creasing phase.

3. High frequency (> 0.20 Hz): High coherence, relatively large gain and minimal phase lead.

Besides gain and coherence, which are used to separate patients from normal autoregulation in Giller (1990), the phase frequency response between CBFV and ABP has also been shown by Panerai et al. (1998) to be an important indicator of autoregulation status, with more positive phase for the group with normal autoregulation in the frequency region $0.06 - 0.20$ Hz, i.e. CBFV oscillations lead ABP oscillations. This finding of positive phase lead indicating active autoregulation is also supported by the results of induced periodic oscillations in Diehl et al. (1995) and Birch et al. (1995). However, it is worth pointing out that we need to be careful adopting transfer function gain and phase in a particular frequency range as criteria as they are no longer valid where the corresponding coherence is low.

Figure 2.5 Transfer function analysis of fluctuations of arterial blood pressure and cerebral blood flow velocity. Group-averaged transfer function: gain (A), phase (B), and magnitude-squared coherence (C) are plotted as solid lines. Dotted lines correspond to Standard Deviation. Adapted from Latka et al. (2005) with permission.



Very few transfer function studies take into account the dynamics of P_{aCO_2} and P_{aO_2} , though they have been demonstrated to play an important role in controlling blood flow, possibly due to the difficulties in obtaining simultaneous measurements. The only transfer function analyses of cerebral autoregulation that include P_{ETCO_2} measurements to account for P_{aCO_2} variability are found in Edwards et al. (2003) and Panerai et al. (2000). They both discussed the effects of CO_2 by using time domain analysis techniques; however

the methods employed do have a direct frequency domain analogue. Panerai et al. (2006) illustrated the importance of considering autoregulation as a multivariate system rather than univariate system identification problem, by using an additive input cerebrovascular resistance index, $CVRI$, defined as $ABP/CBFV$, alongside ABP . The result seems encouraging: the multiple coherence of $CBFV$ for low frequencies is found to be significantly higher than the corresponding values obtained with univariate coherence reported before. However, one system input here, $CVRI$, is directly related to the output, thus it does not contribute to the validity of linear system relationship though it does artificially change the value of the coherence function.

Besides unmeasured variability, nonstationarity is another factor that can invalidate the assumptions of transfer function analysis, especially for measurements taken under certain physiological conditions like exercise or tilting. Normal transfer function analysis simply provides the averaged results, removing any useful time information. As mentioned before, Czosnyka et al. (1996) employed a short time window to obtain Mx index of autoregulation as a time-varying correlation coefficient between spontaneous fluctuations in $CBFV$ and ABP and thus became the first non-stationary investigation in cerebral autoregulation dynamics. Recently, more robust time-varying techniques such as time-varying transfer function analysis (Zhao et al. (2005); Rowley (2008)), wavelet cross-correlation analysis (Rowley et al. (2007); Mizuno-Matsumoto et al. (2005)) and wavelet phase synchronization analysis (Latka et al. (2005); Rowley et al. (2007)) have all been developed to obtain a better estimation of the dynamics of the cerebral autoregulation system.

2.4.4 Time-Frequency Analysis

As mentioned above, the windowed correlation index, Mx , introduced by Czosnyka et al. (1996), characterises the relationship between ABP and $CBFV$ fluctuations as a correlation coefficient over a short window in time. It has the ability to monitor changes that occur in the signal with time, which therefore becomes attractive in clinical settings together with its advantage of low dimensionality. However, it is still a purely time domain analysis and

thus may make it easy to miss the important frequency information of the spontaneous oscillations in physiological variables. Transfer function analysis, in contrast, describes the scaling and phase relationship between fluctuations in ABP and CBFV as a function of frequency, which captures an important aspect of the structure of these fluctuations. However, as discussed before, this transfer function estimation suffers from the big drawback of averaging out all the potential useful time information. To overcome this drawback, it is natural to consider time-frequency analysis which combines the advantages of both time and frequency domain analysis. Several time-frequency algorithms being used for cerebral autoregulation analysis in the literature are thus presented below.

Short-time Fourier transform

The short-time Fourier transform (STFT), first introduced by Gabor (1946), is a Fourier-related transform that determines the sinusoidal frequency and phase content of local sections of a signal as it changes over time. It incorporates a degree of time localisation into the Fourier transform by applying a moving window function of finite length. As the window sliding along the time axis, the resulting two dimensional signal can be expressed as:

$$STFT \{x(t)\} = X(f, \tau) = \int_{-\infty}^{\infty} x(t)w(t - \tau)e^{-j2\pi ft} dt \quad (2.11)$$

where $w(t)$ is the window function, for example, a Gaussian window given by:

$$w(t) = \frac{e^{-t^2/2\sigma^2}}{\sigma\sqrt{2\pi}}, \quad (2.12)$$

the parameter, σ , defining the width of the window in the time domain. A large value of σ increases the frequency resolution of the estimate, however reduces the temporal resolution; a small σ would result in good temporal resolution at the cost of a poor frequency resolution. A frequency vs temporal resolution trade-off exists in the choice of window length, defined by σ here, which is the biggest downfall of the STFT method. Many real signals require good time resolution for high-frequency events, and good frequency resolution for low-frequency events, therefore it is sensible to use a window length that varies

depending upon the frequency being analysed. This is the approach adopted by the wavelet transform (or multi-resolution analysis in general).

The STFT was used in Giller and Mueller (2003) to analyse how the frequency content of TCD measured CBFV changes with time, as a measure of its nonstationary and nonlinear behaviour. Based on the CBFV measurements from 29 healthy subjects, Giller and Mueller (2003) claim that the presence of bifurcations² and chirps³ in the STFT computed spectrograms indicates the presence of non-linearity. This conclusion is questionable: since a short time FFT is a moving average observation, any changes in frequency are smoothed out, and therefore it is more likely that the observed smooth changes in frequency content are artifacts of the process used to compute the STFT (Rowley (2008)). Moreover, changes of the frequency content of *CBFV* are to be expected when the system is driven by multiple inputs. Techniques for investigating the presence of non-linearity in cerebral autoregulation system involves information transfer entropy (Katura et al. (2006)), which is useful in interpreting structure such as directionality in a coupling relationship. However, estimation of the required multivariate probability density functions from short-duration clinical records is a difficult problem. Alternatively, Rowley (2008) overcomes this problem using a Gamma Test which provides similar nonlinear dependency measure, yet with more efficient computation, since it avoids using a kernel based estimation technique.

The Continuous Wavelet Transform

The continuous wavelet transform (CWT) of a signal $x(t)$ is defined for all positive values of scale, a , and time delay, τ , as:

$$W_x(a, \tau) = \frac{1}{\sqrt{a}} \int_{-\infty}^{\infty} x(t) \psi\left(\frac{t-\tau}{a}\right) dt \quad a \in \mathbb{R}^+, \tau \in \mathbb{R}^+, \quad (2.13)$$

where $\psi(t)$ is a continuous function called the mother wavelet and $\psi\left(\frac{t-\tau}{a}\right)$ is a translated and scaled version of the mother wavelet. A valid mother wavelet and its corresponding

²Defined as the smooth splitting of spectral power in a frequency band into two sub-bands over time

³A linear increase in the frequency of most power in the signal with time

Fourier transform, $\Psi(f)$, satisfy the following properties:

$$\int_{-\infty}^{\infty} \psi(t) dt = 0, \quad (2.14)$$

$$\int_{-\infty}^{\infty} |\psi(t)|^2 dt = 1, \quad (2.15)$$

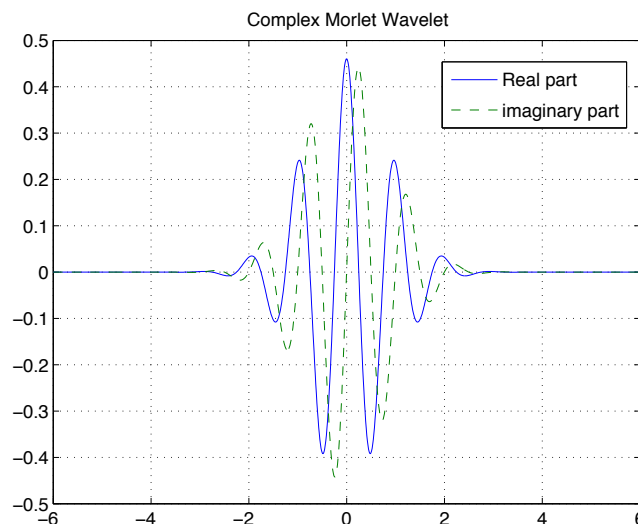
$$\int_0^{\infty} \frac{|\Psi(f)|^2}{f} df < \infty. \quad (2.16)$$

Equation 2.14 ensures that the wavelet has a zero mean value; Equation 2.15 guarantees compact support in the time domain (its nonzero activity is essentially limited to a finite region of time); the last equation is known as the admissibility condition, which is equivalent to compact support in the frequency domain. Some popular mother wavelet of CWT which satisfies all the three conditions are Meyer, Mexican Hat and Morlet wavelets (Percival and Walden (2000)). Mother wavelets can also be in complex form, with one example, the complex Morlet wavelet (Goupillaud et al. (1984)), defined as:

$$\psi(t) = \frac{1}{\sqrt{\pi f_b}} e^{j2\pi f_c t} e^{-t^2/f_b} \quad (2.17)$$

where f_b is the bandwidth and f_c the wavelet centre frequency. The real and imaginary parts of the Morlet wavelet are plotted in Figure 2.6.

Figure 2.6 Complex Morlet Wavelet.



Though the scale a in the wavelet domain mimics frequency in the Fourier transform,

the translation from scale to frequency depends upon the particular choice of wavelet. However, an approximate relationship between wavelet scale a and translated frequency, pseudo-frequency, f_a , for a given wavelet and a sampling period can be computed as (cit):

$$f_a = \frac{f_c}{a \times \Delta}, \quad (2.18)$$

where f_c is the centre frequency of a wavelet in Hz, and Δ is the sampling period. This translation allows a direct comparison to be made between wavelet-based and Fourier-based analysis.

Latka et al. (2005) used the complex Morlet wavelet with the CWT to compute the instantaneous phase of the CBFV and ABP signals and a synchronization index between the two signals, defined as the standard deviation of the phase difference in a wrapped coordinate system (Fisher (1995)):

$$\bar{\Delta\phi}(a) = \tan^{-1} \left\{ \frac{\sum_t \sin(\Delta\phi(a, t))}{\sum_t \cos(\Delta\phi(a, t))} \right\}. \quad (2.19)$$

Studies carried out in healthy subjects showed two distinct peaks in synchronization at around 0.1Hz and 0.33Hz, corresponding to the Mayer wave and respiration rhythms respectively. In contrast, the phase difference in the low frequency region (0.02 – 0.07Hz) showed an almost uniform distribution, involving zero and negative phase, which has been referred to as intermittent autoregulatory failure (Giller and Mueller (2003)). It should be noted, however, that Latka et al. (2005) do not consider any measure of P_{aCO_2} and P_{aO_2} reactivity which could play an important role in the instantaneous phase of CBFV in the low frequency region.

Besides investigating the instantaneous phase difference, wavelet cross-correlation was introduced in Rowley et al. (2007) as the cross-correlation between CWT coefficients of two time series. Compared to ordinary cross-correlation, wavelet cross-correlation is also an measure of similarity between two time series, but localised to different frequencies. This CWT-based technique was used by Rowley et al. (2007) to analyse the coupling between oscillations in ABP and NIRS measured O_2Hb in both autonomic failure patients and age-matched controls. A statistical difference was found in the scales of maximum wavelet

cross-correlation, suggesting that cerebral and systemic changes are coupled at different frequencies for patients and healthy subjects.

Despite the various advantages of CWT, this algorithm is, however, computationally expensive, as it converts a one dimensional signal to a two dimensional matrix of time-frequency wavelet coefficients which introduces redundancy. As a result, discrete wavelet transforms, provide an alternative approach that retains certain key features of the CWT yet with a significant reduction in computational expense.

The Discrete Wavelet Transform

The main idea of the discrete wavelet transform (DWT) is the same as for the CWT, i.e. to obtain a time-scale representation of a signal, but in a more succinct manner (Percival and Walden (2000)). The CWT is computed by changing the scale of the analysis window, shifting the window in time, multiplying by the signal, and integrating over all times. In the discrete case, a time-scale representation is obtained using digital filtering techniques: the signal is passed through a series of high-pass filters to analyse the high frequencies, and it is passed through low-pass filters to analyse the low frequencies. Mathematically, it can be written as:

$$W_1[n] = (x * g)[n] = \sum_{k=-\infty}^{\infty} x[k]g[n - k] \quad (2.20)$$

$$V_1[n] = (x * h)[n] = \sum_{k=-\infty}^{\infty} x[k]h[n - k] \quad (2.21)$$

where g represents the impulse response of high-pass (wavelet) filter and h of low-pass (scaling) filter. The two filters are related to each other and are known as a quadrature mirror filter. The outputs gives the detail coefficients, $W_1[n]$ and approximation coefficients, $V_1[n]$.

However, since half the frequencies of the signal have now been removed, half the samples can be discarded according to Nyquist's rule. So the detail coefficients and the approxima-

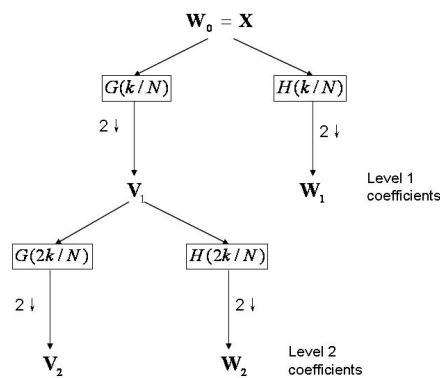
tion coefficients can be subsampled to:

$$(W_1 \downarrow 2)[n] = W_1[2n] = \sum_{k=-\infty}^{\infty} x[k]g[2n - k] \quad (2.22)$$

$$(V_1 \downarrow 2)[n] = V_1[2n] = \sum_{k=-\infty}^{\infty} x[k]h[2n - k] \quad (2.23)$$

This decomposition has halved the time resolution since only half of each of the filter output characterises the signal. However, each output has half the frequency band of the input so the frequency resolution has doubled. This decomposition is repeated on the approximation coefficients which is further decomposed with the high and low pass filters and then down-sampled, allowing higher frequency resolution on the low frequency component. This decomposition of the signal into discrete frequency bands in the discrete filtering stages of the pyramid algorithm are shown in Figure 2.7. $H(\cdot)$ and $G(\cdot)$ in the figure represent the frequency domain transfer function of the discrete filters h and g .

Figure 2.7 DWT decomposition. At each level of the pyramidal algorithm the signal is decomposed into low and high frequencies. Due to the decomposition process the input signal must be a multiple of $2n$ where n is the number of levels.



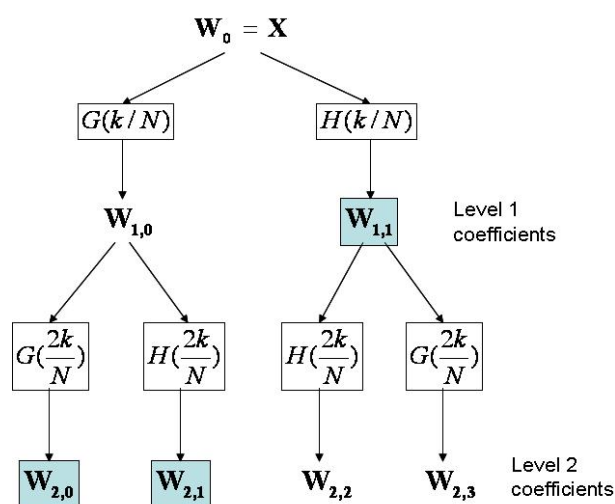
The Maximal Overlap Discrete Wavelet Packet Transform

The Maximal Overlap Discrete Wavelet Packet Transform (MODWPT) has two important advantages over the DWT. First, it is translationally invariant; if a pattern in a time series is translated, translational invariance of a transform technique specifies that the numerical descriptors of the time series in the transform domain are translated from the original time domain but not modified (Mallat (1999)). In contrast to the standard

DWT, MODWPT omits the subsampling in the time domain at each stage of the pyramid algorithm. Instead, it inserts zeros into the discrete filter banks and rescales the coefficients by $\sqrt{2}$, as shown in Figure 2.8. This desired time invariant transform enable the MODWPT details and smooths associated with zero phase filter, thus easy to be lined up with the original time series (Percival and Walden (2000)).

Secondly, the use of the Discrete Wavelet Package transform breaks up the limit of the frequency resolution of DWT that high scales (low frequencies) always have greater frequency resolution than low scales (high frequencies), which may not always be optimal for analysis in the frequency domain. As shown in Figure 2.8, it passes the approximating coefficients into the filter bank as well as the detail coefficients, which gives a library of wavelet coefficients and allows for adaptive selection of frequency resolution (Percival and Walden (2000)).

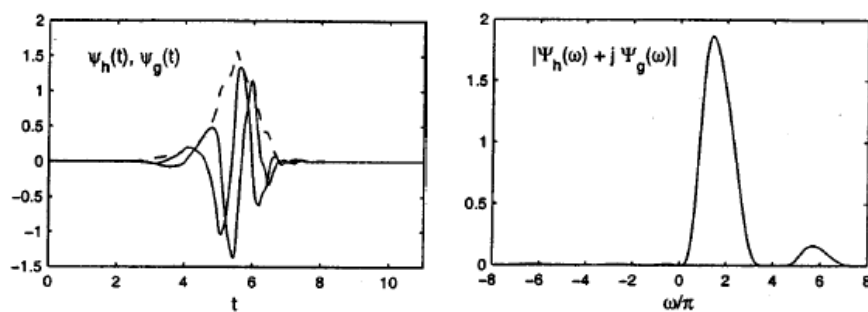
Figure 2.8 MODWPT decomposition. Compared to DWT, the MODWPT pyramidal decomposition avoids the subsampling process and the obtained coefficients have the same length as the original time series. Moreover, MODWPT has more flexible frequency resolution than DWT.



For the MODWPT, complex coefficients can be obtained such that the real and imaginary components of each coefficient form an approximate Hilbert relationship by the use of Hilbert wavelet pair filters (Selesnick (2002); Selesnick et al. (2005); Whitcher and Craig-mille (2004); Whitcher et al. (2005)). An example pair of wavelet filteres forms approxi-

mate Hilbert relationship are shown in Figure 2.9. Similar to the complex Morlet wavelet in CWT, this MODWPT is also able to produce an approximate analytical signal localised at both time and frequency, with the complex magnitude approximating the amplitude of the signal at that frequency and the angle approximating the phase. Based on MODWPT decomposition, time-varying auto and cross power spectral density functions can be estimated, allowing for estimation of a time varying transfer function and coherence functions. The use of the MODWPT in this way was first proposed by Whitcher et al. (2005) to analyse signals obtained from electromyograph (EMG) recording in human subjects. It was further applied to the analysis of dynamic autoregulation in Rowley (2008) as a time-varying multivariate system identification.

Figure 2.9 Approximate Hilbert transform pair of orthonormal wavelet (left) and mid-phase spectral factorization (right). Adapted from Selesnick et al. (2005) with permission.



2.5 Summary

This chapter has provided a comprehensive overview of the literature relevant to the field. The physiological processes of the maintenance and regulation of cerebral blood flow by the systemic cardiovascular control and cerebral vasculature were presented in Section 2.2. Successful monitoring of cerebral autoregulation performed on human subjects in clinical settings was introduced in Section 2.3, where it was also shown that these measurements incorporate numerous artefacts due to unmeasured variability and the limitations of non-invasive measurement procedures. The assessment of autoregulation status used in clinical settings and presented in the literature was then outlined in Section 2.4. In particular,

the multivariate and time-varying characteristics associated with cerebral autoregulation requires techniques that are robust in the presence of unmeasured variability and that can cope with changes in signal statistics due to nonstationarities to obtain a reliable clinical diagnosis of cerebral autoregulation.

Chapter 3 will thus use an existing physiologically-based model, Combined Hemodynamic System (CHS) of Payne (2006), to investigate the interaction among pressure autoregulation, CO_2 reactivity and neural activation processes. It will investigate the effects of P_{aCO_2} variability on the pressure-flow relationship and the neural activity-BOLD signal relationship, both of which could influence the assessment of autoregulation and BOLD response if not accounted for.

Chapter 4 will then demonstrate, using an experimental data-set, how accounting for P_{aCO_2} variability by measurement of P_{ETCO_2} allows improved recovery of the dynamics of cerebral autoregulation using a standard multivariate system identification algorithm, as indicated by the increased multiple coherence values compared to univariate coherence in the low frequency range. This shows that some of the apparent system nonlinearities suggested by the observed low values of coherence at low frequencies in the literature can actually be attributed to unmeasured variability.

Chapter 5 will further address another important characteristic of actual physiological measurements, nonstationarity, which invalidates the precondition of linear transfer function analysis. Using the same data-set as in Chapter 4, it will be demonstrated how P_{aCO_2} variations distort the instantaneous phase relationship between ABP and CBFV and account for the low synchronization index identified by Latka et al. (2005). This suggests that some apparent nonstationarity can also be attributed to other physiological variability not being taken into account.

Chapters 4 and 5 demonstrate the importance of considering P_{aCO_2} variability, yet present a system analysis technique accounting for CO_2 effects, that assumes that the properties of this relationship remain constant with time, which is however not always necessarily

valid. Chapter 6 will demonstrate how the maximal overlap wavelet packet transform may be used to relax this assumption by considering a bivariate relationship in a particular frequency band. This new algorithm will be used to investigate the age-dependency of both cardiovascular and cerebral changes in response to orthostatic stress.

Chapter 7 will investigate sources of low-frequency variation in BOLD signal arising from spontaneous fluctuations in P_{aCO_2} and heart rate in volunteers at rest, suggesting that it is extremely important to consider systemic changes when performing functional imaging studies.

System definition

3.1 Introduction

In Chapter 2, a summary of current physiologically-based models of cerebral autoregulation was given, showing how they can be helpful in testing hypotheses about complex interacting systems. Recently, Payne (2006) proposed a unified mathematical model which incorporated the cerebral blood flow and oxygenation responses to three different local stimuli: changes in ABP, CO_2 and neural activity within a single structure. Despite the physiological fact that all these stimuli act on the same cerebral system, this model is the only one that integrates different models of the cerebral vasculature in order to combine the contributions of different stimuli. The model can thus be used, for example, to explore how variations in CO_2 influence the CBF or BOLD responses to one particular input that is of direct interest, i.e. CBF regulation to pressure change and BOLD response to neural stimulus.

In this chapter, some of the assumptions made in the above model are examined and a revised version of Payne's model, termed the Combined Hemodynamic System (CHS) is presented. The new version of the model makes fewer approximations about a crucial model parameter, and extends the prediction range of the model to include changes in the de-

oxyhaemoglobin (HHb), oxyhaemoglobin (O_2Hb) and total haemoglobin (tHb) responses to neural activity, as well as the CBF and BOLD responses. This enables many more parameters to be compared to experimental results from the literature. Moreover, the transfer functions of cerebral autoregulation and CO_2 reactivity based on CHS are derived, using the same linearisation method proposed by Payne and Tarassenko (2006), linking the complex physiologically-based models to experimentally-derived results. This thus combines the advantages of both approaches and opens up the possibility of estimating autoregulation status clinically as well as helping to provide physiological insights into the processes that govern cerebral autoregulation. Additionally, such a linearised model can be used to test advanced signal processing techniques, which will be presented in the following chapters.

3.2 Model Description

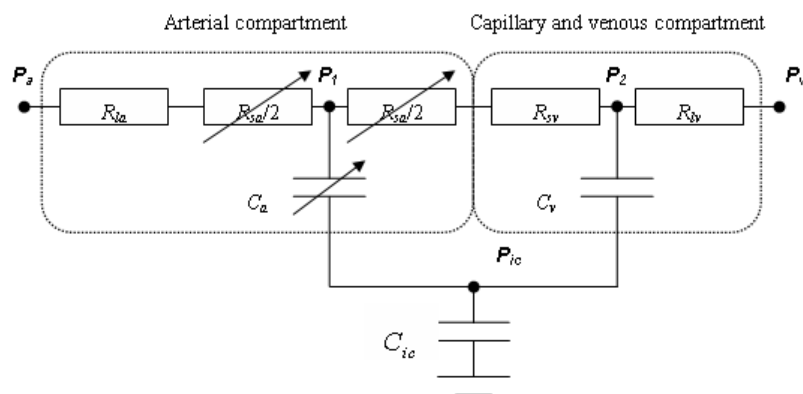
The schematic of the CHS is shown in Figure 3.1, which is very similar to the model used in Payne (2006) and Ursino et al. (2000), the differences being discussed below.

The system is divided into two main subsystems: the arterial compartment and the capillary-venous compartment. The arterial compartment is further divided into regulating and non-regulating compartments: the first segment representing the larger arteries, which are assumed to have fixed resistance, R_{la} , and blood volume, V_{la} ; the second representing the smaller arteries and arterioles, where changes in arterial compliance, C_a , baseline value \bar{C}_a , allow for the changes in arterial volume, V_{sa} , baseline value \bar{V}_{sa} , and thus resistance, R_{sa} , baseline value \bar{R}_{sa} . It is the second segment that is primarily responsible for flow regulation.

The capillaries are assumed to have a fixed resistance and volume, whereas the venous compartment is assumed to have a fixed resistance but varying volume, V_v , baseline value V_{vn} , which is controlled by the venous compliance, C_v . The two resistors in Figure 3.1 represent the capillary and small veins, R_{sv} , and the larger veins, R_{lv} , respectively. In-

tracranial pressure, ICP, P_{ic} , baseline value \bar{P}_{ic} , primarily changes as a result of varying cerebral blood volume (CBV). The modelling of changes in ICP is difficult because of the lack of experimental data in normal subjects. Here a nonlinear compliance C_{ic} is taken to characterize the intracranial pressure-volume (P_{ic} - V_{ic}) relationship, in common with many other authors, for example Ursino et al. (2000) and Lu et al. (2004). This is the main difference between the CHS model presented here and the one in Payne (2006), which assumed ICP to be constant. The difference between their simulation results will be shown below.

Figure 3.1 Schematic of model: P_a , systemic arterial pressure; R_{la} , resistance of non-regulating arterial compartment; P_1 , R_{sa} and C_a , pressure, resistance, and compliance of regulating arterial compartment; R_{sv} , resistance of capillary compartment and small veins; C_v , venous compliance; P_2 , venous pressure; P_v and R_{lv} , venous pressure and resistance of large veins, respectively; P_{ic} , intracranial pressure; C_{ic} , intracranial compliance



The haemodynamic equations are used to relate the pressure, volume and resistance of the different compartments of the cerebral system. In the arterial compartment, the vessel resistance is assumed to vary with the inverse of radius to the power four, where volume is proportional to the radius squared, thus for regulating vessels, volume varies according to the inverse square root of the resistance. Together with the definition of compliance and

the conservation law for blood flow, this gives for the arterial compartment¹:

$$\frac{V_{sa}}{\bar{V}_{sa}} = \sqrt{\frac{\bar{R}_{sa}}{R_{sa}}}, \quad (3.1)$$

$$\frac{dV_{sa}}{dt} = \frac{d(C_a(P_1 - P_{ic}))}{dt}, \quad (3.2)$$

$$\frac{dV_{sa}}{dt} = \frac{P_a - P_1}{R_{la} + R_{sa}/2} - \frac{P_1 - P_2}{R_{sa}/2 + R_{sv}}. \quad (3.3)$$

In the capillary and venous compartment:

$$\frac{dV_v}{dt} = C_v \frac{d(P_2 - P_{ic})}{dt}, \quad (3.4)$$

$$C_v = \frac{1}{k_{ven}(P_2 - \bar{P}_{ic} - P_{v1})}, \quad (3.5)$$

$$\frac{dV_v}{dt} = \frac{P_1 - P_2}{R_{sa}/2 + R_{sv}} - \frac{P_2 - P_v}{R_{lv}}, \quad (3.6)$$

where k_{ven} and P_{v1} are constants. Venous volume can then be directly calculated by substitution of Equation 3.5 into Equation 3.4 and integrating to give:

$$V_v = \left(\frac{1}{k_{ven}} \right) \ln(P_2 - \bar{P}_{ic} - P_{v1}) + V_{vn}. \quad (3.7)$$

The constant of integration, V_{vn} , is set to give a suitable basal venous volume fraction.

Cerebral blood flow can be calculated in big arteries:

$$F_{in,a} = \frac{P_a - P_1}{R_{la} + R_{sa}/2}, \quad (3.8)$$

in the microvasculature:

$$q = F_{out,a} = F_{in,v} = \frac{P_1 - P_2}{R_{sa}/2 + R_{sv}}, \quad (3.9)$$

and in the venous outflow:

$$F_{out,v} = \frac{P_2 - P_v}{R_{lv}}. \quad (3.10)$$

ICP variations can be calculated from:

$$\frac{dV_{ic}}{dt} = C_{ic} \frac{dP_{ic}}{dt}, \quad (3.11)$$

$$C_{ic} = \frac{1}{K_e P_{ic}}, \quad (3.12)$$

$$\frac{dV_{ic}}{dt} = \frac{dV_{sa}}{dt} + \frac{dV_v}{dt}, \quad (3.13)$$

¹In the following equations, capital letters are used to represent the parameter value, the small letter representing the non-dimensional value respectively, i.e. the parameter value divided by its baseline value

where K_e is the rigidity coefficient of the cranium, whose normal values have been estimated to be in the range of 0.7 to 2.9 (Ursino et al. (2000)). The variation of volume ($\frac{dV_{ic}}{dt}$) is the sum of the variations of arterial volume (V_{sa}) and venous volume (V_v) since changes in capillary volume and CSF volume are neglected. All the values of the parameters used in the CHS are given in Table 3.1.

Table 3.1 Parameters Used in the Simulations of CHS

Parameter	Description	Value
R_{la}	Resistance of large (non-regulating) arteries	$1.4mmHg.s/ml$
R_{sa}	Baseline resistance of small (regulating) arteries	$4.03mmHg.s/ml$
R_{sv}	Resistance of small veins (including capillaries)	$1.32mmHg.s/ml$
R_{lv}	Resistance of large veins	$0.56mmHg.s/ml$
P_a	Baseline arterial blood pressure	$100mmHg$
P_v	Venous outlet pressure	$6mmHg$
P_{ic}	Baseline of intracranial pressure	$10mmHg$
P_{vl}	Pressure offset for venous compliance	$-2.25mmHg$
V_{la}	Volume of large (non-regulating) arteries	$1ml$
V_{sa}	Baseline volume of large (non-regulating) arteries	$12ml$
V_{vn}	Offset for venous volume	$28ml$
V_{iv}	Baseline of intracranial volume	$80ml$
C_a	Baseline arterial compliance	$0.205ml/mmHg$
k_{ven}	Elastance coefficient for venous compliance	$0.186/ml$
k_e	Rigidity coefficient of the cranium	$0.08/ml$
G_q	Gain of flow-based feedback mechanism	$3.0ml/mmHg$
τ_q	Time constant of flow-based feedback mechanism	$20s$
Pa_{CO_2}	Baseline arterial CO_2 pressure	$40mmHg$
τ_{CO_2}	Time constant of arterial CO_2 pressure	$40s$
ΔC_a^+	Amplitude of positive change in arterial compliance	$2.87ml/mmHg$
ΔC_a^-	Amplitude of negative change in arterial compliance	$0.164ml/mmHg$
τ_1	First time constant for neural feedback	$2s$
τ_2	Second time constant for neural feedback	$6s$
g	Baseline non-dimensional tissue oxygen concentration	0.2
E	Baseline Oxygen Extraction Fraction	$0, 4$
τ_g	Time constant for tissue oxygen concentration	$1s$
K	Scaling between activation and oxygen demand	0.05
ϵ	Scaling factor for neuronal efficacy	1
V_0	Scaling factor for BOLD response	0.02

The feedback system is assumed to consist of three stimulating mechanisms for adjusting arterial compliance: CBF (q), arterial CO_2 concentration (Pa_{CO_2}) and neural stimulation

(*u*). As in Payne (2006), these are assumed to be of the form:

$$\tau_q \frac{dx_q}{dt} + x_q = G_q \left(\frac{q - \bar{q}}{\bar{q}} \right), \quad (3.14)$$

$$\tau_{CO_2} \frac{dx_{CO_2}}{dt} + x_{CO_2} = fn \left(\frac{Pa_{CO_2}}{Pa_{CO_2}} \right), \quad (3.15)$$

$$\tau_1 \tau_2 \frac{d^2 x_M}{dt^2} + (\tau_1 + \tau_2) \frac{dx_M}{dt} + x_M = \epsilon u, \quad (3.16)$$

where changes in CBF and arterial CO_2 from their baseline values act to stimulate delayed changes in their respective state variables. The delays are mimicked by first order filters with time constants of τ_q and τ_{CO_2} respectively. For CO_2 the function in Equation 3.15 is selected to provide the best fit to the data of Reivich (1964):

$$fn \left(\frac{Pa_{CO_2}}{Pa_{CO_2}} \right) = 0.3 + 3 \tanh \left(\frac{Pa_{CO_2}}{Pa_{CO_2}} - 1.1 \right). \quad (3.17)$$

In Equation 3.16, the scaling factor ϵ represents the efficacy with which neuronal activity causes an increase in the state variable. τ_1 and τ_2 are the time constants for neural activation. It is then assumed that the three feedback mechanisms act in a linearly additive manner:

$$x = x_M + x_{CO_2} - x_q, \quad (3.18)$$

and that x then modifies C_a by means of the following sigmoidal relationship, Ursino et al. (2000):

$$C_a = \bar{C}_a + \frac{1}{2} \left\{ \begin{array}{l} \Delta C_a^+ \tanh \left(\frac{2x}{\Delta C_a^+} \right) \text{if } x > 0, \\ \Delta C_a^- \tanh \left(\frac{2x}{\Delta C_a^-} \right) \text{if } x < 0 \end{array} \right\}. \quad (3.19)$$

Previous studies (Aaslid et al. (1989)) have indicated that CO_2 level has a major effect on CBF autoregulation. Specifically, during hypercapnia, the CBF increases and autoregulation is impaired, whereas in hypocapnia, CBF decreases and autoregulation is improved, which suggests the two mechanisms are not actually linearly additive. This relationship will be further discussed in the next section.

The deoxyhaemoglobin transport equation previously derived in Buxton et al. (1998), based on mass transport, is used here:

$$\tau_v \dot{h}_v = f_{in,v} \frac{E}{E_0} - f_{out,v} \frac{h_v}{v_v}, \quad (3.20)$$

where h_v is the venous deoxyhaemoglobin, and τ_v is the venous transit time defined as $\tau_v = \frac{\bar{V}_v}{\bar{q}}$, the ratio of baseline venous volume to baseline flow. CBF, $f_{in,v}$, venous outflow, $f_{out,v}$ and venous volume, v_v , are all derived from the haemodynamic model. The OEF, E , is related to CBF by the oxygen transport model for steady flow described in Zheng et al. (2002). Similarly, the venous oxyhaemoglobin transport equation, based on mass balance, is:

$$\tau_v \dot{o}_v = f_{in,v} \frac{1 - E}{1 - E_0} - f_{out,v} \frac{o_v}{v_v}, \quad (3.21)$$

and finally BOLD response is calculated using the following equation proposed in Obata et al. (2004):

$$\frac{\Delta B}{B} = V_0(a_1(1 - h_v)) - a_2(1 - v_v), \quad (3.22)$$

where $a_1 = 3.4E_0/0.4$ and $a_2 = 0.57E_0/0.4 + 0.43$ for $B_0 = 1.5T$ and $TE = 40ms$.

Finally, the oxygen haemoglobin and deoxyhaemoglobin and total haemoglobin in the cerebral blood flow can be estimated as the weighted volume sum of the oxyhaemoglobin, deoxyhaemoglobin and total haemoglobin in the arterial compartment and venous compartment²:

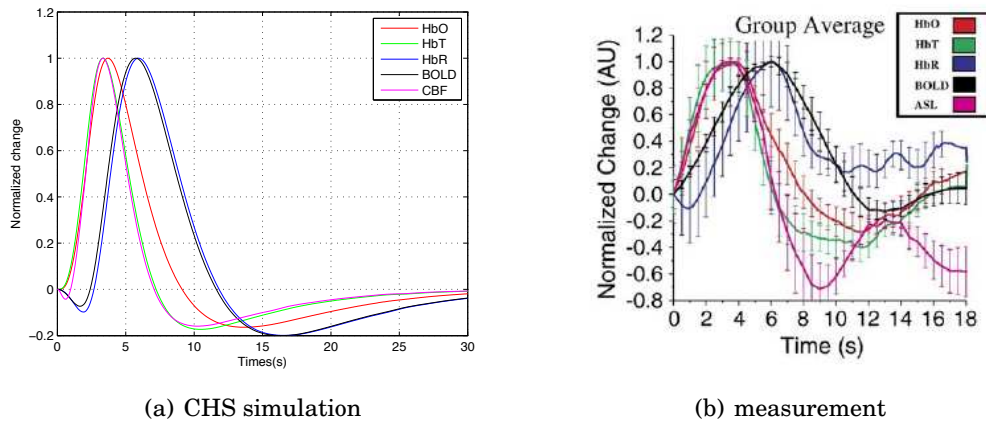
$$HbO = \frac{o_a(1 - r_v) + o_v r_v(1 - E_0)}{1 - r_v + r_v(1 - E_0)}, \quad (3.23)$$

$$HbR = \frac{h_a(1 - r_v) + h_v r_v E_0}{r_v E_0}, \quad (3.24)$$

$$HbT = o_a + h_a(1 - r_v) + o_v r_v(1 - E_0) + h_v r_v E_0, \quad (3.25)$$

where r_v is the ratio of baseline venous volume to the total cerebral blood volume, which can be calculated as $\bar{V}_v / (V_{la} + \bar{V}_{sa} + \bar{V}_v)$. o_a can be estimated as 1 and h_a as 0 based on the assumption that there is no deoxyhaemoglobin in arterial flow.

Figure 3.2 a) Model-predicted haemodynamic response of CHS; b) Group-averaged response functions from simultaneous NIRS and ASL-fMRI scans (Huppert et al. (2005)) to 2s neural stimulus.



3.3 Simulation results

3.3.1 Neural activation

The model response of the model simulation to a 2s neural stimulus under normal conditions are shown in Figure 3.2(a) including *HbO*, *HbR*, *HbT*, CBF and the BOLD response. Simulation results have been normalized to the maximum change of each parameter, and the *HbR* traces have been inverted to allow better visual comparison with experimental data. Measured haemodynamic responses using NIRS and ASL-fMRI instruments are also presented in Figure 3.2(b) for comparison (Huppert et al. (2005)).

Table 3.2 The time-to-peak of the region-of-interest averaged responses for the five haemodynamic parameters measured in Huppert et al. (2005) and simulation result of CHS

Parameter	Experiment TTP (s)	Simulation TTP (s)
CBF	3.4 ± 0.7	3.3
<i>HbO</i>	4.0 ± 1.4	3.6
<i>HbT</i>	3.9 ± 1.5	3.3
<i>HbR</i>	6.0 ± 1.0	6.0
<i>BOLD</i>	5.9 ± 1.0	5.8

Table 3.2 is a summary of values of the time-to-peak (TTP) of the region-of-interest averaged responses for the five haemodynamic parameters measured in Huppert et al. (2005)

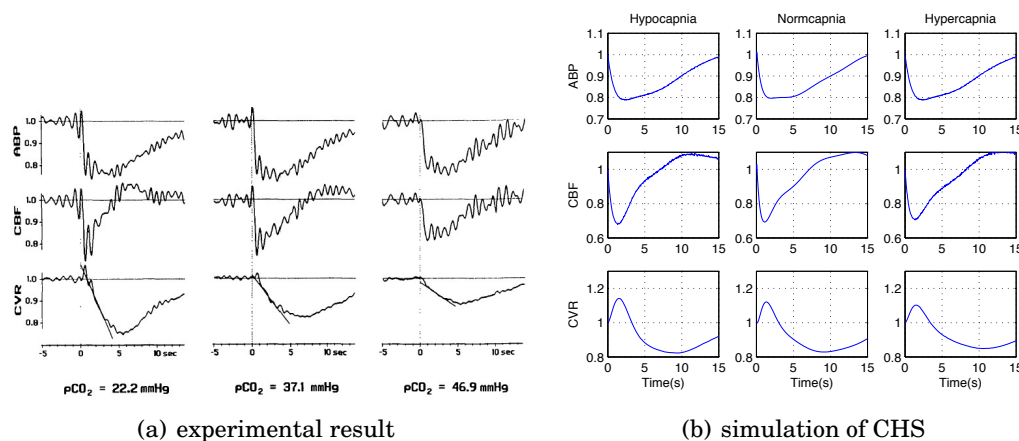
²These are fractional values

to a short 2-s finger-tapping task, in comparison with the model prediction. The simulation results agree very well with the experimental data, which predicts a lag between the peak HbR and HbO (HbT) responses and the BOLD and CBF responses of approximately 2 seconds.

3.3.2 CO_2 effect

Chapter 2 outlined the importance of P_{aCO_2} in the modulation of pressure autoregulation. It has been demonstrated in Aaslid et al. (1989) that hypercapnia impairs autoregulation, whereas hypocapnia improves it, this being by examination of the CBF response in a thigh-cuff experiment at different P_{aCO_2} levels, as shown in Figure 3.3(a). In the CHS, this CO_2 effect was modelled as an additional input of the feedback system controlling CBF. Note that is, the CHS model presented here, ICP is not assumed constant, unlike in Payne (2006), since hypercapnic or hypocapnic conditions will induce relatively large changes in CBV and thus ICP. The simulation results of CHS are shown in Figure 3.3(b), compared to the experimental results.

Figure 3.3 Simulation of thigh cuff experiments using CHS. Thigh cuffs are deflated at 0s. From left to right: hypocapnia, normocapnia, and hypercapnia.



In hypocapnia (Figure 3.3(a), left), autoregulatory action was very rapid; after only 1.9 seconds ΔCBF was reduced by half and after 4.2 seconds it was greater than its initial value. The autoregulatory response was slower in normocapnia (Figure 3.3(a), middle);

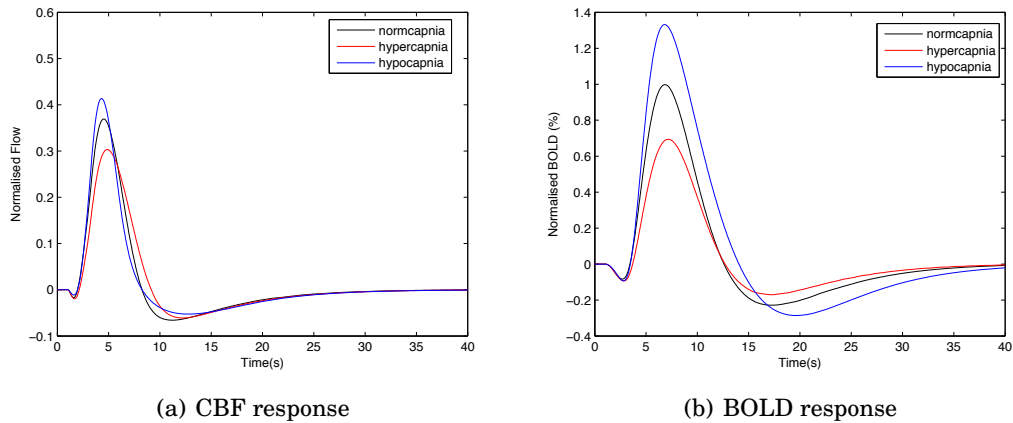
the time for half-maximal response being 3.4 seconds, with overshoot being smaller than that found in hypercapnia. No overshoot and a much-delayed half-maximal response were found in hypercapnia (Figure 3.3(a), right). Calculated cerebrovascular resistance, CVR, is presented in the bottom of the figure. In the simulation results (Figure 3.3(b)), CBF response and CVR of normcapnia (Figure 3.3(b),middle) is most consistent with the experimental result except for a larger initial overshoot of CVR. The CBF response and CVR of both hypercapnia (Figure 3.3(b), left) and hypocapnia (Figure 3.3(b), right) are significantly different from the experimental results, which suggests that autoregulation gain G_q and time constant τ_q cannot be assumed to be constant in different Pa_{CO_2} state. In other words, the model assumption that the two stimuli, ABP and CO_2 are linearly added, does not hold; their interaction relationship is more complex.

Another phenomenon worth noticing is the initial overshoot of CVR (calculated by dividing ABP by CBF). The initial overshoot of CVR illustrates that there is a time lag of active autoregulation to changes in ABP , and the immediate passive response of blood vessels to the drop of ABP is volume dilation rather than constriction, which makes the proportional CBF change even bigger than the ABP change. There is a vasodilatory peak of CVR simultaneous with the ABP rise which represents a large passive arterial dilatation due to the ABP transients (Panerai et al. (2005)). The CHS models this process well by using a first-order linear system to introduce delay into the active autoregulation response.

The effects of CO_2 on the dynamics of the CBF and $BOLD$ responses to neural stimulus are more controversial, as illustrated by the debate over experimental results in current literature, as presented in Chapter 2. With the CHS model, which incorporates neural activation and physiological variation together, we are able to investigate the $BOLD$ response at different CO_2 levels by model simulation.

The $BOLD$ responses predicted by the proposed model for a 4s stimulus of magnitude 0.3 starting at 1s in hypocapnia ($Pa_{CO_2} = 30mmHg$), normocapnia ($Pa_{CO_2} = 40mmHg$) and hypercapnia ($Pa_{CO_2} = 50mmHg$) are shown in Figure 3.4.

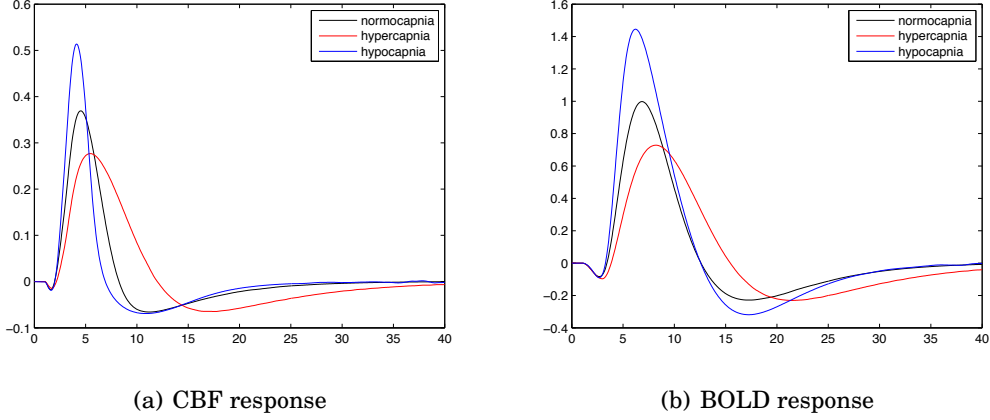
Figure 3.4 Model predicted CBF and BOLD responses in normocapnic, hypercapnic and hypocapnic conditions.



The magnitude of the BOLD response decreases with increasing CO_2 level, which is consistent with the finding of Bandettini and Wong (1997) and Cohen et al. (2002), whilst contradicting those of other studies, Corfield et al. (2001), Posse et al. (2001), Kemna and Posse (2001). The TTP of predicted CBF slightly increases with the increasing CO_2 level, which reflects the trend that the CBF response slows down in hypercapnia whereas it speeds up in hypocapnia, according to the finding of Kemna and Posse (2001). However, the TTP of predicted BOLD response is almost the same, rather than increasing with elevated CO_2 , as shown in the experiments of Cohen et al. (2002), Kemna and Posse (2001) and Posse et al. (2001).

As mentioned above, the three stimuli are added linearly, so the gains and time constants governing each stimulus are independent of each other. In Section 3.4.3 it will be shown that the system coupling the neural activity to CBF can be estimated by a fourth order linear system, whose dominant time constants are τ_1 and τ_2 . Thus, the response time of CBF will be in predominantly determined by these time constants, rather than by the other model parameters, which should be the main reason for the model failing to predict the variation in the time constant of the haemodynamic response with varying CO_2 . If the assumption that the feedback parameters are constant is relaxed, i.e. that the haemodynamic response slows down with increasing CO_2 level, as shown in Figure 3.5, this shows

Figure 3.5 Model predicted CBF and BOLD response in normocapnia, hypercapnia and hypocapnia condition, with the three feedback systems correlated. $\tau_1 = 2.0$, $\tau_2 = 6.0$, $\tau_q = 20$ in normocapnia; $\tau_1 = 2.0$, $\tau_2 = 8.0$, $\tau_q = 40$ in hypercapnia; and $\tau_1 = 2.0$, $\tau_2 = 4.0$, $\tau_q = 15$ in hypocapnia.



much better agreement with the trends found in the literature.

3.4 Model linearisation

3.4.1 Linear transfer function of autoregulation

To derive the linear transfer function, small changes about the basal conditions are assumed using a Taylor series expansion. Since the resulting equations will all be linear, the Laplace transform is used to convert the differential equations into a transfer function. The differential equations governing the flow autoregulation from Section 3.2 are thus linearised to the difference equations presented below.

Equation 3.1 becomes:

$$\Delta R_{sa} = -2 \frac{\Delta V_{sa}}{V_{sa}} R_{sa}. \quad (3.26)$$

Equation 3.2 becomes:

$$s\Delta V_{sa} = sC_a(\Delta P_1 - \Delta P_{ic}) + s\Delta C_a(P_1 - P_{ic}). \quad (3.27)$$

Equation 3.3 becomes:

$$s\Delta V_{sa} = \frac{\Delta P_a - \Delta P_1}{R_{la} + R_{sa}/2} - q \frac{\Delta R_{sa}}{R_{la} + R_{sa}/2} - \Delta q. \quad (3.28)$$

Equation 3.4 and Equation 3.6 become:

$$\begin{aligned} s\Delta V_v &= sC_v\Delta P_2 \\ &= \frac{\Delta P_1 - \Delta P_2}{R_{sa}/2 + R_{sv}} - q \frac{\Delta R_{sa}/2}{R_{sa}/2 + R_{sv}} - \frac{\Delta P_2}{R_{lv}}. \end{aligned} \quad (3.29)$$

Equation 3.11 and Equation 3.13 combine to give:

$$\begin{aligned} s\Delta V_{ic} &= sC_{ic}\Delta P_{ic} \\ &= s\Delta V_{sa} + \Delta V_v. \end{aligned} \quad (3.30)$$

Equation 3.19 is simplified to:

$$C_a = \bar{C}_a - x, \quad (3.31)$$

which together with Equation 3.14 gives:

$$\Delta C_a = -G_q \frac{\Delta q}{q(1 + s\tau_q)}. \quad (3.32)$$

Equation 3.9 becomes:

$$\Delta q = \frac{\Delta P_1 - \Delta P_2}{R_{sa}/2 + R_{sv}} - q \frac{\Delta R_{sa}/2}{R_{sa}/2 + R_{sv}}. \quad (3.33)$$

q is the microvascular CBF, which drives the BOLD response in the CHS. However, what can be measured directly by Transcranial Doppler is actually the velocity of flow in the middle cerebral artery (V_{MCA}), which is equivalent to $f_{in,a}$ in the CHS. The expression for V_{MCA} can be derived from Equation 3.8:

$$V_{MCA} = \frac{1}{A} \frac{P_a - P_1}{R_{la} + R_{sa}/2}, \quad (3.34)$$

where A is the cross-sectional area of the MCA, which is assumed to be invariant here. Angiographic studies and direct visualization of the MCA during surgery have suggested that, during a variety of stimuli known to affect cerebral blood flow, the diameter of the MCA changes minimally ($< 3.0\%$) (Zhang et al. (1998a)). However, small changes in diameter are difficult to measure and may produce large changes in velocity. The assumption made in this study is that changes in diameter of the MCA are minimal; therefore, beat-to-beat

changes in mean velocity may represent predominantly beat-to-beat changes in cerebral blood flow. Hence for small pressure changes, velocity changes will be:

$$\frac{\Delta V_{MCA}}{V_{MCA}} = \frac{\Delta P_a - \Delta P_1}{P_a - P_1} - \frac{\Delta R_{sa}/2}{R_{la} + R_{sa}/2}. \quad (3.35)$$

By eliminating other unwanted parameters, the transfer functions for both CBF and V_{MCA} can be derived from the above difference equations:

$$\begin{aligned} H_1(s) &= \frac{\Delta q/\bar{q}}{\Delta P_a/\bar{P}_a} \\ &= \frac{(\alpha_3 + 1)\alpha_1 + 1}{\beta_1(1 + (\alpha_3 + 1)\alpha_1) - (\beta_2 + \frac{\beta_3}{1+s\tau_v})(1 - (\alpha_3 + 1)\alpha_1 - s\alpha_1\tau_a) + (\frac{\alpha_2}{1+s\tau_q})(2 - s\alpha_1\tau_a)}, \end{aligned} \quad (3.36)$$

$$\begin{aligned} H_2(s) &= \frac{\Delta V_{MCA}/V_{MCA}}{\Delta P_a/\bar{P}_a} \\ &= \frac{1}{\beta_1} \left\{ 1 + \frac{(\beta_2 + \frac{\beta_3}{1+s\tau_v})(1 - (\alpha_3 + 1)\alpha_1) - \frac{2\alpha_2}{1+s\tau_q}}{\beta_1(1 + (\alpha_3 + 1)\alpha_1) - (\beta_2 + \frac{\beta_3}{1+s\tau_v})(1 - (\alpha_3 + 1)\alpha_1 - s\alpha_1\tau_a) + (\frac{\alpha_2}{1+s\tau_q})(2 - s\alpha_1\tau_a)} \right\}, \end{aligned} \quad (3.37)$$

where the relevant non-dimensional parameters and time constants are:

$$\alpha_1 = \frac{\bar{V}_{sa}/\bar{q}}{\bar{R}_{sa}\bar{C}_a}, \quad (3.38)$$

$$\alpha_2 = G_q \left[\left(\frac{\bar{P}_a - \bar{P}_{ic}}{\bar{P}_a - \bar{P}_{vs}} \right) - \beta_1 \right] / \bar{C}_a, \quad (3.39)$$

$$\alpha_3 = \frac{\bar{C}_a}{\bar{C}_{ic}}, \quad (3.40)$$

$$\beta_1 = \frac{R_{la} + \bar{R}_{sa}/2}{R_{total}}, \quad (3.41)$$

$$\beta_2 = \frac{\bar{R}_{sa}/2 + R_{sv}}{R_{total}}, \quad (3.42)$$

$$\beta_3 = \frac{R_{lv}}{R_{total}}, \quad (3.43)$$

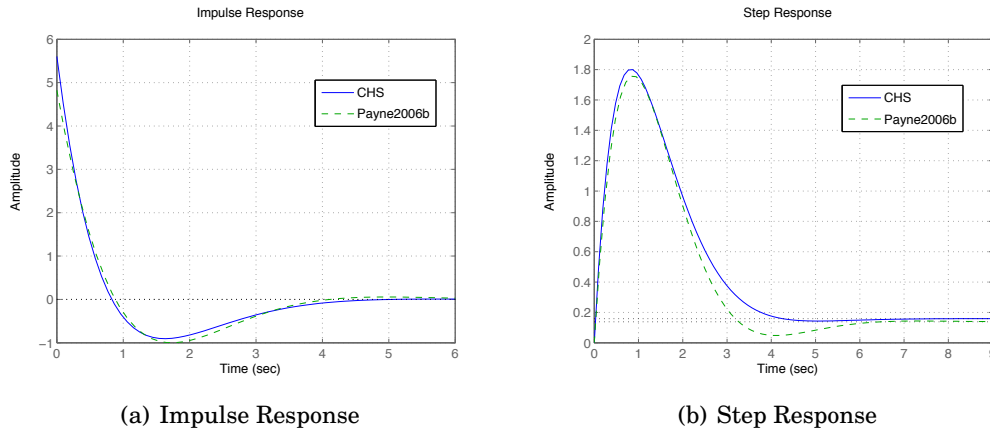
$$\tau_a = (R_{la} + \bar{R}_{sa}/2)\bar{C}_a, \quad (3.44)$$

$$\tau_v = R_{lv}\bar{C}_v. \quad (3.45)$$

The first parameter is a ratio of time constants, the second a measure of feedback gain, the third is a ratio between arterial compliance and intracranial compliance, the fourth to the sixth the fractions of different compartments of resistance, linked by $\beta_1 + \beta_2 + \beta_3 = 1$, and

the seventh and the eighth are time constants related to the arterial and venous compartments respectively. The CBF transfer function has a numerator of order 2 and a denominator of order 3, whereas the V_{MCA} transfer function has numerator and denominator both of order 3, which means that a sudden increase (or decrease) in blood pressure will produce a sudden increase (or decrease) in velocity. The two transfer functions are very similar to those derived in Payne (2006), as the nonlinear systems are quite similar to each other. The influence of changes in intracranial pressure is solely reflected in the non-dimensional parameter α_3 in the modified transfer function, which will be discussed below.

Figure 3.6 a) Impulse response of CBF transfer functions of CHS and that derived in Payne and Tarassenko (2006). b) Step response of CBF transfer function of CHS and that derived in Payne and Tarassenko (2006). The dotted lines in 3.6(b) represent the final values of the step responses.



Since R_{sa} comprises the majority of the resistance to flow, β_3 is relatively small compared to β_1 and β_2 ; it is thus assumed to be close to zero. The transfer functions then approximate to:

$$H_1(s) = \frac{(\alpha_3 + 1)\alpha_1 + 1}{((\alpha_3 + 1)\alpha_1 + 2\beta_1 - 1) + (1 - \beta_1)s\alpha_1\tau_a + \left(\frac{\alpha_2}{1+s\tau_q}\right)(2 - s\alpha_1\tau_a)}, \quad (3.46)$$

$$H_2(s) = \frac{1}{\beta_1} \left\{ 1 + \frac{(1 - \beta_1)(1 - (\alpha_3 + 1)\alpha_1) - \frac{2\alpha_2}{1+s\tau_q}}{((\alpha_3 + 1)\alpha_1 + 2\beta_1 - 1) + (1 - \beta_1)s\alpha_1\tau_a + \left(\frac{\alpha_2}{1+s\tau_q}\right)(2 - s\alpha_1\tau_a)} \right\}. \quad (3.47)$$

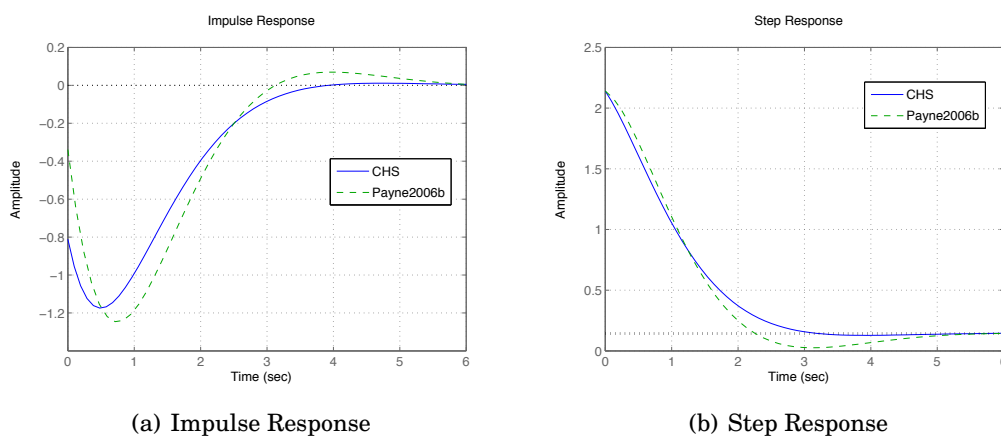
The simplified transfer functions for both CBF and V_{MCA} are second order, and the parameters in the transfer function are reduced to $(\alpha_1, \alpha_2, \alpha_3, \beta_1, \tau_q, \tau_a)$. By using the parameter

values given earlier, the values of the non-dimensional parameters in the transfer function are found to be:

$$\begin{aligned}\alpha_1 &= 0.8738 & \alpha_2 &= 5.5503 & \alpha_3 &= 0.1640 \\ \beta_1 &= 0.4672 & \tau_q &= 20s & \tau_a &= 0.9231s\end{aligned}$$

The impulse response (IR) and the step response (SR) of the CBF and V_{MCA} transfer functions are shown in Figure 3.6 and Figure 3.7 respectively. The impulse response and step response of the transfer function for both CBF and V_{MCA} , as derived by Payne (2006) are also presented for comparison.

Figure 3.7 a) Impulse response of V_{MCA} transfer function of CHS and CBF transfer function derived in Payne (2006). b) Step response of V_{MCA} transfer function of CHS and V_{MCA} transfer function derived in Payne (2006). The dotted lines in 3.7(b) represent their final values.



As shown in Figure 3.6 and Figure 3.7, the CBF and V_{MCA} responses are quite different from each other. The step response of CBF starts from zero, which illustrates that CBF does not show a sudden change in response to a sudden ABP change. The different dynamic behaviour of CBF and V_{MCA} is due to the passive storage properties of small arteries and arterioles, modelled as a compliance in the haemodynamic circuit. In some other models, the two are not properly distinguished. The classic Tiecks model of Tiecks et al. (1995) models the flow autoregulation through a feedback term in the V_{MCA} , rather than in the microvascular CBF.

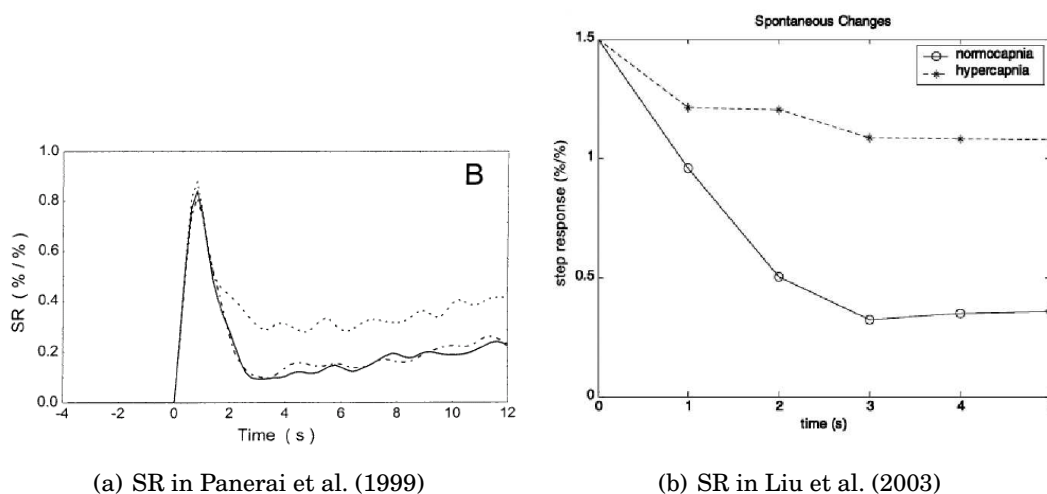
The influence of ICP changes on autoregulation is reflected by the longer time constant

of the IR and SR of CHS compared to that of the fixed ICP model. Most studies of cerebral autoregulation in humans assume that ICP is low and that it is not affected by the induced changes in ABP, due to the difficulty of obtaining accurate measurements of ICP. However, Panerai et al. (2002) applied the transfer function approach to measurements of ABP, V_{MCA} and ICP performed in head injury patients and demonstrated that ICP can influence estimates of dynamic cerebral autoregulation, including in the patient group whose ICP were relatively low and ABP- V_{MCA} transfer function were similar to normal subjects. In the CHS, all the values of parameters related to ICP oscillation are in the normal range, resulting in similar IR and SR of calculated transfer function compared to that of the fixed ICP model, which suggests that the changes in ICP of normal subjects have little effect on the autoregulation status.

As mentioned in Chapter 2, many different linear and nonlinear models have been used in the literature to obtain the IR and SR of V_{MCA} , including ARX models (Liu et al. (2003)), the Tiecks model (Tiecks et al. (1995), Panerai et al. (1999)), fast Fourier transforms (Panerai et al. (1999), Zhang et al. (1998a)), Linear Wiener-Laguerre models (Panerai et al. (1999), Panerai et al. (2001), Mitsis et al. (2002)) and Quadratic Wiener-Laguerre models (Panerai et al. (1999), Mitsis et al. (2002)). In addition, different types of manoeuvre have been adopted to produce pressor or depressor changes, including thigh cuff test, Valsalva maneuver, cold pressor test, lower body negative pressure, and hand grip test, as well as continuous baseline recording (Panerai et al. (2001), Liu et al. (2003)). The patterns of IR and SR obtained by different models and different stimuli however vary widely, as shown in Figure 3.8 cited from two different experiments. Payne and Tarassenko (2006) use their derived IR to fit one set of the experimental data, connecting the physiologically based models with the experimentally based transfer function analysis. However, the fitted values of some parameters such as the time constant of autoregulation, τ , found by Payne and Tarassenko (2006), were much smaller than the values expected from the literature. This is mainly due to two reasons: first, the theoretical IR, calculated from the continuous system in Payne and Tarassenko (2006), is not exactly the same as the discrete IR

obtained from the experimental data through the system identification techniques. Second, since the values of some model parameters are quite sensitive to the precise values of the experimentally obtained IR, it is hard to achieve very accurate values especially when the signal-to-noise ratio of the experimental data is low.

Figure 3.8 a) Step response from Panerai et al. (1999): Full curve and dash-dotted curve represent SR in normocapnia, dotted curve represent SR in hypercapnia. b) Step responses in Liu et al. (2003), circular line represent SR in normocapnia and star line hypercapnia.

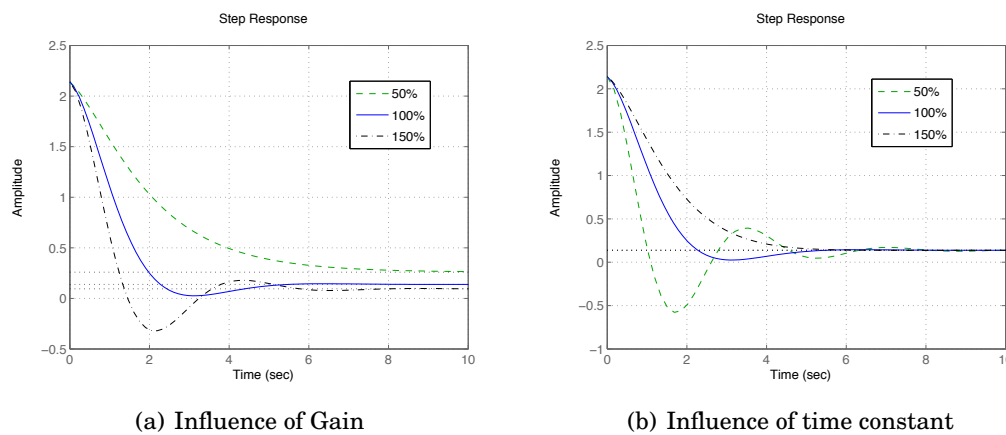


As a result, the IR or SR will not be used here to fit a particular set of experimental data from the literature; instead, the derived transfer function will be compared with some of the features that are agreed generally in the literature. The first is transit time: from Figure 3.7, IR and SR take about 3 seconds before they return to the static state, which is consistent with the literature. The influence of the two parameters governing the flow feedback, G_q and τ_q , on the speed of autoregulation are shown in Figure 3.9. As the feedback gain is elevated, the response becomes increasingly oscillatory, with a deeper trough occurring earlier: the response time thus speeds up, but becomes less stable. As the feedback time constant is elevated, the reverse response occurs. The second feature relates to the final value of the SR, which is equivalent to the static state of autoregulation. The expression of final value of SR can be derived from Equation 3.47:

$$FV = \frac{1}{\beta_1} \left[1 + \frac{(1 - (1 + \alpha_3)\alpha_1)(1 - \beta_1) - 2\alpha_2}{(1 + \alpha_3)\alpha_1 - 1 + 2\alpha_2} \right], \quad (3.48)$$

which is related to G_q through α_2 . A decreased flow feedback gain, G_q , representing impaired autoregulation status in hypercapnia, can be used to explain the findings of Panerai et al. (1999) and Liu et al. (2003) that the final value of SR in hypercapnia stays at a higher value. as shown in Figure 3.8.

Figure 3.9 Variation in V_{MCA} SR for changes in: (a) feedback gain; (b) feedback time constant.



3.4.2 The CO_2 response

Alongside cerebral pressure autoregulation, the other main mechanism responsible for controlling CBF is the reactivity of cerebral vessels to the arterial CO_2 level. A number of physiological studies have shown that CBF response to a step change in CO_2 is not instantaneous but shows a relatively slow rise. Poulin et al. (1996) and Poulin et al. (1998) describe the rising phase of V_{MCA} by a simple exponential equation with a time constant of 45s and a pure delay of 6s to step changes of end-tidal CO_2 ($EtCO_2$) (Poulin et al. (1996)). Panerai et al. (2000) and Mitsis et al. (2004b) studied the dynamic characteristics of the Pa_{CO_2} - V_{MCA} relationship through the measurement of breath-by-breath variability in $EtCO_2$ in continuous recordings obtained from normal subjects at rest. It was found that $EtCO_2$ fluctuations and the interactions between $MABP$ and $EtCO_2$ have a considerable effect in the low frequency of V_{MCA} variation. Since CHS has coupled the flow autoregulation and CO_2 reactivity together, it is thus valuable to calculate the transfer function

of the flow reponse to CO_2 and to compare it to Poulin et al.'s model and other available experimental data. This is similar to the approach of Payne and Tarassenko but applied to CO_2 changes.

The differential equations governing CO_2 cerebrovascular reactivity are almost the same as those governing flow autoregulation. The difference exists only in two equations: Equation 3.3 becomes:

$$s\Delta V_{sa} = -\frac{\Delta P_1}{R_{la} + R_{sa}/2} - q\frac{\Delta R_{sa}}{R_{la} + R_{sa}/2} - \Delta q, \quad (3.49)$$

since there is no arterial pressure change, the compliance equation (Equation 3.19) becomes:

$$\Delta C_a = -G_q\frac{\Delta q}{q(1 + s\tau_q)} + G_{CO_2}\frac{\Delta Pa_{CO_2}}{Pa_{CO_2}(1 + s\tau_{CO_2})}. \quad (3.50)$$

After simplification, the transfer function of both CBF and V_{MCA} to CO_2 changes are obtained:

$$\begin{aligned} J_1(s) &= \frac{\Delta q/q}{\Delta Pa_{CO_2}/Pa_{CO_2}} \\ &= \frac{\alpha_2(2 - s\alpha_1\tau_a)}{((\alpha_3 + 1)\alpha_1 + 2\beta_1 - 1) + (1 - \beta_1)s\alpha_1\tau_a + (\frac{\alpha_2}{1+s\tau_q})(2 - s\alpha_1\tau_a)} \\ &\quad * \frac{G_{CO_2}/G_q}{1 + s\tau_{CO_2}}, \end{aligned} \quad (3.51)$$

$$\begin{aligned} J_2(s) &= \frac{\Delta V_{MCA}/V_{MCA}}{\Delta Pa_{CO_2}/Pa_{CO_2}} \\ &= \frac{1}{\beta_1} \left\{ 1 + \frac{\alpha_2(2\beta_1 + (1 - \beta_1)s\alpha_1\tau_a)}{((\alpha_3 + 1)\alpha_1 + 2\beta_1 - 1) + (1 - \beta_1)s\alpha_1\tau_a + (\frac{\alpha_2}{1+s\tau_q})(2 - s\alpha_1\tau_a)} \right\} \\ &\quad * \frac{G_{CO_2}/G_q}{1 + s\tau_{CO_2}}. \end{aligned} \quad (3.52)$$

where the definitions of $[\alpha_1, \alpha_2, \alpha_3, \beta_1, \tau_q, \tau_a]$ are the same as before. Compared to Equation 3.47, only two new parameters, G_{CO_2}/G_q and τ_{CO_2} , are introduced. The impulse response and step response of the V_{MCA} transfer function are shown in Figure 3.10, with the experimentally derived IR and SR in Figure 3.11 for comparison.

The step reponse (Figure 3.10(b)) is in good agreement with previous observations of the V_{MCA} response to step-like changes in CO_2 , such as Wilson et al. (1985), Ellingsen et al.

Figure 3.10 Model predicted: a) Impulse response; b) Step response of V_{MCA} to CO_2 change.

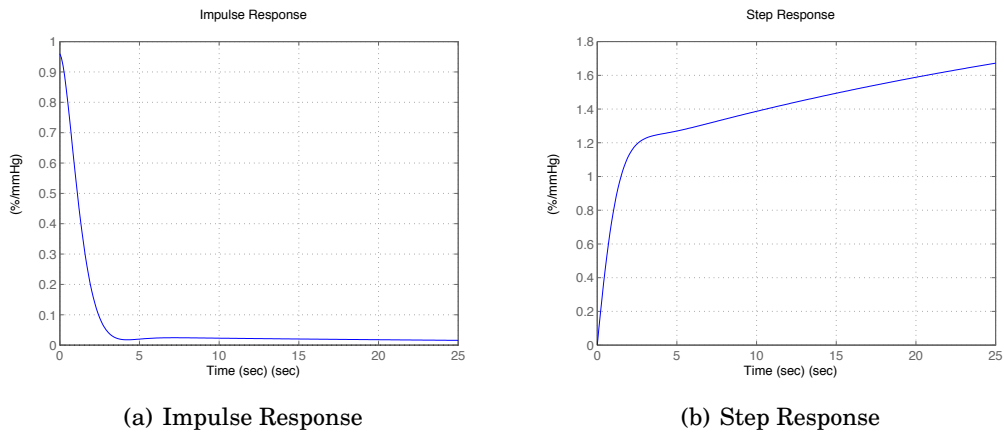


Figure 3.11 Experimentally derived: a) Impulse response; b) Step response of V_{MCA} to CO_2 change (Panerai et al. (2000)).

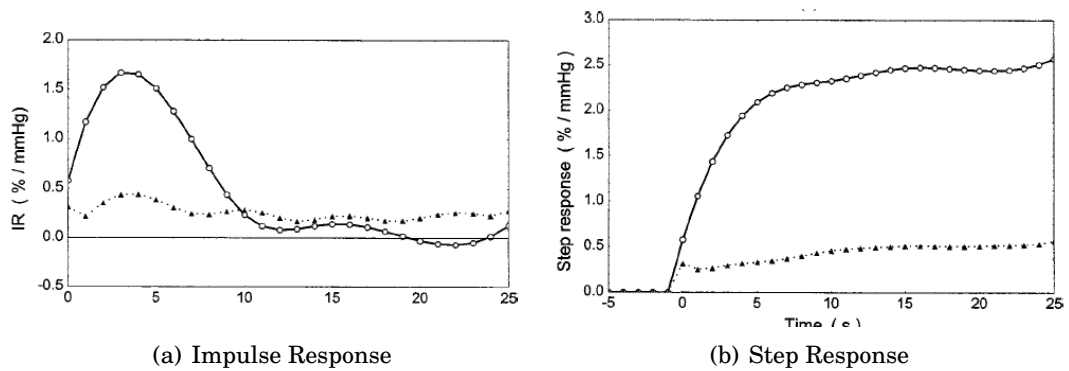
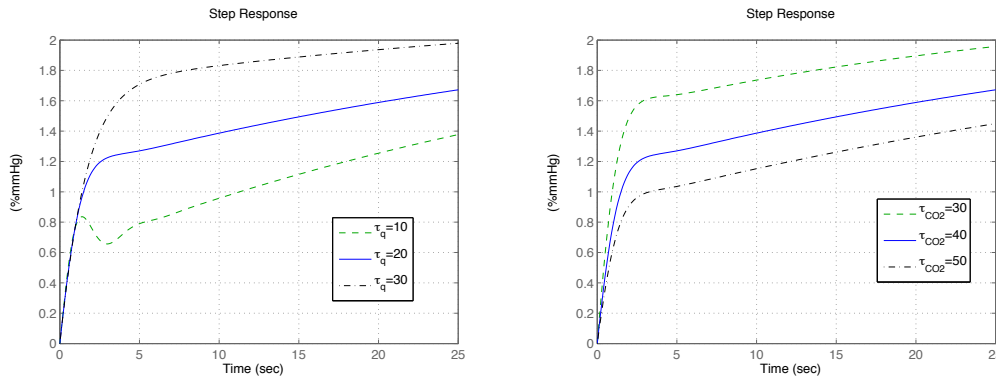


Figure 3.12 a) Variation in V_{MCA} impulse response for changes in: (a) Flow regulation time constant; (b) CO_2 reactivity time constant.



(a) Influence of flow regulation time constant

(b) Influence of CO_2 reactivity time constant

(1987), Poulin et al. (1996) and Poulin et al. (1998). In particular, the simulations illustrate that there are two different time constants in the step response, which is consistent with the experimental result of Panerai et al. (2000). However, the fast increase occurs in 0 – 2.5 seconds in the model predicted SR, which is different from 6 seconds observed in Panerai et al. (2000). Poulin et al. (1996) and Poulin et al. (1998) also mentioned the existence of fast and slow components of cerebral blood flow response to step change in $EtCO_2$. The current model gives a possible explanation of the observed two phases: the initial shape rise of the flow response is vessel dilation in response to the increasing CO_2 level, and then the increase slows down as increased CBF activates the competitive flow feedback mechanism and thus offsets the influence of the dilation stimulus of CO_2 . Thus the speed of response of CO_2 reactivity is not only determined by the CO_2 feedback time constant, τ_{CO_2} , but also by the flow feedback time constant, τ_q , as shown in Figure 3.12.

In Poulin et al. (1996), an asymmetry in the transient response to a positive and negative step in the $EtCO_2$ was observed, which is due to the asymmetry of wash in and out times of the CO_2 stimulus (Garnham et al. (1999)). The above simulation results suggest another possible cause: flow autoregulation status is different at different CO_2 levels, which implied that different values of flow regulation time constant are found in the "on" and "off" responses, thus resulting in a different response speed.

Panerai et al. (2000) also provide the impulse response of CO_2 reactivity, which shows a peak at approximately 4s. It should be noticed that the simulation result (Figure 3.10(a)) is significantly different from the experiment result (Figure 3.11(a)). This could be due to changes in some model parameter values, as in the fitted parameters of $ABP - V_{MCA}$ transfer function in Payne and Tarassenko (2006). Another possible reason is a pure time delay, as introduced in Poulin et al. (1996), shifting the peak of the equivalent impulse response and thus the model fitting improved considerably.

3.4.3 BOLD response

The physiological basis of the BOLD response in fMRI studies was explained in Chapter 2. Several mathematical models have been proposed to link the changes in measured BOLD signal to changes in neural activity. Models are described relating: (1) neural activity to changes in CBF; (2) flow changes to oxygen delivery to tissue through capillaries, and thus HHb concentration in the venous compartment; (3) flow changes to changes in CBV; (4) changes of CBV and HHb to the BOLD response. Friston et al. (2000) proposed a second-order haemodynamic model which simulates the CBF response to underlying neural activity u . When coupled with the well known Balloon model linking CBF and BOLD (Buxton et al. (1998); Obata et al. (2004)), it is able to predict the dynamics of the BOLD response to neural activation. As shown in Figure 3.14(b), the predicted first-order Volterra Kernel emulate the empirical kernels in every way except for the protracted undershoot. In this section, the linearised version of CHS is used to predict the linear kernel and thus to demonstrate its advantage over the second-order haemodynamic model of Friston et al. (2000).

CHS models the CBF response to neural activity u through a compliance change:

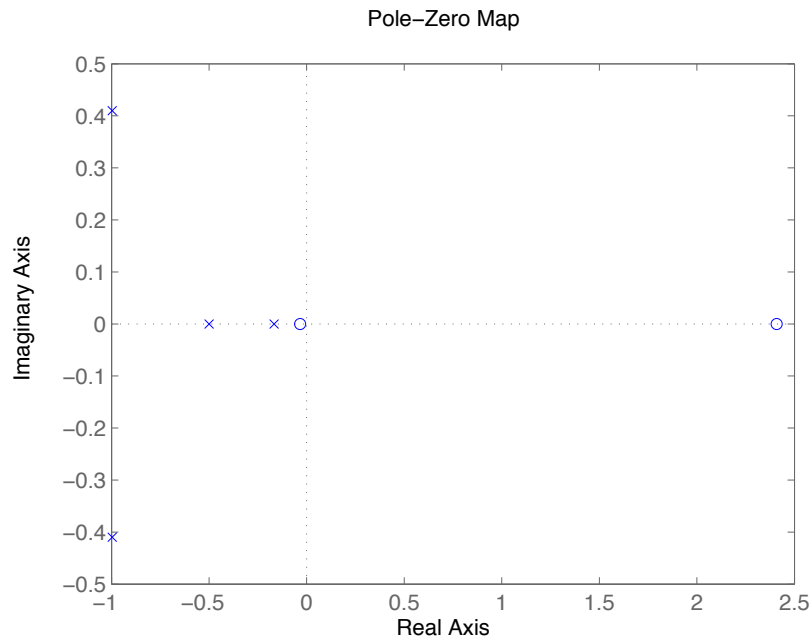
$$\Delta C_a = -G_q \frac{\Delta q}{q(1 + s\tau_q)} + \frac{\epsilon u}{(s\tau_1 + 1)(s\tau_2 + 1)}. \quad (3.53)$$

The derived transfer function linking the neural activity (u) to the CBF response is:

$$\begin{aligned}
 M_1(s) &= \frac{\Delta q/q}{u} \\
 &= \frac{\alpha_2(2 - s\alpha_1\tau_a)}{(\alpha_3 + 1)\alpha_1 + 2\beta_1 - 1 + (1 - \beta_1)s\alpha_1\tau_a + \left(\frac{\alpha_2}{1+s\tau_q}\right)(2 - s\alpha_1\tau_a)} \\
 &\quad * \frac{\epsilon}{(1 + s\tau_1)(1 + s\tau_2)}.
 \end{aligned} \tag{3.54}$$

where the definitions of $[\alpha_1, \alpha_2, \alpha_3, \beta_1, \tau_q, \tau_a]$ are the same as before. As shown in its pole-zero map (Figure 3.13), $1/\tau_1$ and $1/\tau_2$, two poles most close to Y axis, control the speed of CBF response to neural activation.

Figure 3.13 Pole-zero map of $u - CBF$ transfer function. Two poles most close to Y axis corresponds to $1/\tau_1$ and $1/\tau_2$.



CHS also incorporates oxygen delivery equation derived in Buxton et al. (1998) and Zheng et al. (2002), which extends the cerebral circuit to a full BOLD signal model. The differen-

tial equations governing the regional CBF to BOLD response are:

$$E = (1 - g)(1 - (1 - \frac{E_0}{1 - g_0})^{1/q}), \quad (3.55)$$

$$\tau_g \dot{g} = \frac{E}{E_0} q - k u, \quad (3.56)$$

$$\tau_v \dot{v}_v = q - f_{out,v}, \quad (3.57)$$

$$\dot{f}_{out,v} = \frac{\bar{V}_v/\bar{q}}{R_{lv}\bar{C}_v} \dot{v}_v, \quad (3.58)$$

$$\tau_v \dot{h}_v = q \frac{E}{E_0} - f_{out,v} \frac{h_v}{v_v}, \quad (3.59)$$

$$y = V_0(a_1(1 - h_v)) - a_2(1 - v_v). \quad (3.60)$$

The corresponding linearized equations are:

$$\Delta E = -\Delta g(1 - C) + (1 - g_0)C \ln C \frac{\Delta q}{q}, \quad (3.61)$$

$$\tau_g s \Delta g = \frac{\Delta E}{E_0} + \frac{\Delta q}{q}, \quad (3.62)$$

$$\tau_v s \Delta v_v = \frac{\Delta q}{q} - \Delta f_{out,v}, \quad (3.63)$$

$$\Delta f_{out,v} = \alpha_v \Delta v_v, \quad (3.64)$$

$$\tau_v s \Delta h_v = \frac{\Delta E}{E_0} + \frac{\Delta q}{q} - \Delta f_{out,v} - \Delta h_v + \Delta v_v, \quad (3.65)$$

$$\Delta y = V_0(-a_1 \Delta h_v + a_2 \Delta v_v), \quad (3.66)$$

where $C = (1 - \frac{E_0}{1 - g_0})^{1/q}$, $\alpha_v = \frac{\bar{V}_v/\bar{q}}{R_{lv}\bar{C}_v}$. The corresponding transfer function is:

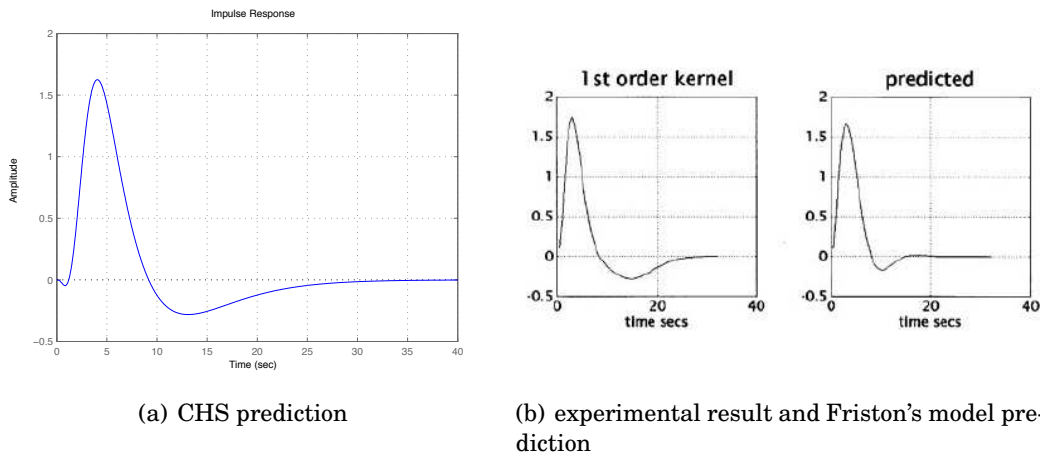
$$\begin{aligned} K(s) &= \frac{\Delta y/y}{\Delta q/q} \\ &= \frac{(a_2 - a_1)V_0}{\alpha_v + s\tau_v} + \frac{a_1 V_0}{1 + s\tau_v} - \frac{a_1 V_0 s (E_0 + (1 - g_0 - E_0) \ln C)}{\frac{E_0}{1 - g_0} (1 + s\tau_g (1 - g_0)) (1 + s\tau_v)}. \end{aligned} \quad (3.67)$$

The transfer function linking neural activity u to BOLD response y is finally:

$$\begin{aligned} M(s) &= \frac{\Delta y/y}{u} \\ &= M_1(s) * K(s). \end{aligned} \quad (3.68)$$

The impulse response of $K(s)$, which is the exact equivalent of the 1st-order kernel, is shown in Figure 3.14(a), in comparison with the empirical and model-based kernel of Friston et al. (2000) (Figure 3.14(b)).

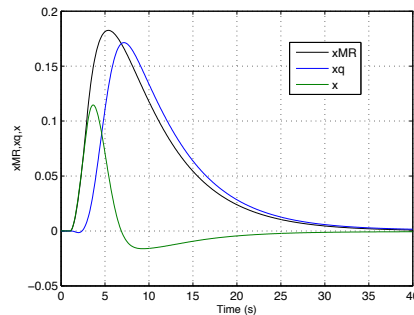
Figure 3.14 a) Predicted first-order kernel of the CHS model. b) The left-hand panel is the first-order kernel based on parameter estimates from the experimental data. The right-hand panel is the first-order kernel predicted by the haemodynamic model of Friston et al. (2000).



It can be seen that there is a remarkable agreement in the first order kernel, especially in the protracted post-stimulus undershoot, which is not predicted by the model of Friston et al. but is predicted by the CHS model. This is important because it suggests that the time constants governing the positive BOLD signal and its post-stimulus undershoot are different, which is natural as the former is caused by the neural stimulus whereas the latter is proposed to be due to flow autoregulation here. In the CHS, the protracted undershoot of BOLD originates from the protracted undershoot of x , the state variable modifying arterial compliance, which is further controlled by both the neural stimulus and flow autoregulation mechanism, as shown in Figure 3.15. In the absence of autoregulation, the post-stimulus undershoot will disappear (Payne (2006)). This finding, again, agrees well with the experimental results of Cohen et al. (2002), suggesting a prolonged undershoot in the hypocapnic and normocapnic conditions which is absent in the hypercapnic condition, where the autoregulation mechanism is impaired.

As mentioned in Chapter 2, besides neural activation, changes in P_{aCO_2} will also modulate global CBF and thus global BOLD signal (Grubb et al. (1974); Hoge et al. (1999a,b)). For the CHS, the transfer function linking P_{aCO_2} to the BOLD response y can be also derived

Figure 3.15 State variable governing arterial compliance, x , the neural activity feedback factor, x_{MR} and the flow autoregulation feedback factor, x_q in response to a 2 s neural stimulus starting at 1s. x is calculated as $x_{MR} - x_q$.



as:

$$\begin{aligned}
 J(s) &= \frac{\Delta y/y}{\Delta P_{aCO_2}/P_{aCO_2}} \\
 &= J_1(s) * K(s).
 \end{aligned}
 \tag{3.69}$$

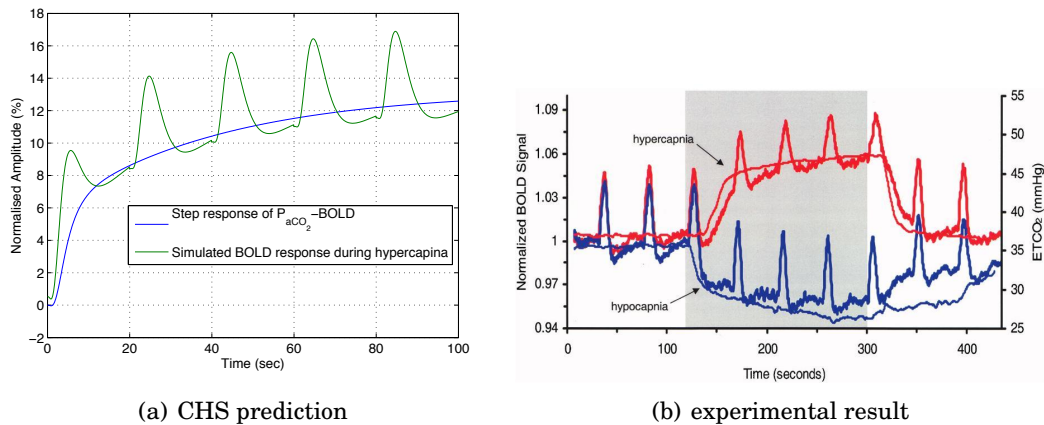
where J_1 is Equation 3.51, the $P_{aCO_2} - CBF$ transfer function derived above.

The step response of $J(s)$, which predicts the global BOLD response to a sudden change in P_{aCO_2} , is shown in Figure 3.16(a), together with the simulated BOLD response to neural activation in hypercapnia. Similar to the CBF step response to P_{aCO_2} changes, the global BOLD response to step-like changes in CO_2 also shows two different time constants, a fast increase followed by a slow change, in good agreement with previous observations of Cohen et al. (2002), shown in Figure 3.16(b). The activation of autoregulation mechanisms, again, was hypothesized to slow down the BOLD response here. It also be worth to notice the time constant of fast response at hypercapnia is longer than hypocapnia (Figure 3.16(b)), which could be due to the increased time delay of impaired autoregulation at hypercapnia.

3.5 Discussion

A compact model of the haemodynamic response to changes in ABP, CO_2 level, and neural activity has been presented, and it has been shown how this agrees qualitatively with the available data, and captures some of the key experimental observations in qualitative form,

Figure 3.16 a) Step response of BOLD to CO_2 change (blue line) and simulated BOLD response to neural activation in hypercapnia (green line). b) Averaged blood oxygenation level dependent (BOLD) time courses (thick lines) and averaged end-tidal CO_2 (ETco2) level (thin lines) during the normocapnia/hypercapnia (red lines) and the normocapnia/hypocapnia (blue lines) experiments (Cohen et al. (2002)).



the reasons for poor prediction of others also being explored. The model is not expected to be a complete mathematical explanation of autoregulation and the BOLD response and to recover the experimental data perfectly; advantage has simply been taken of the numerous computational tools available to develop models directly from the experimental literature which can reproduce similar results in order that the most important pathways can be simulated, and the effects of interventions to various pathways modelled.

In the arterial compartment of the CHS, the regulating compliance, C_a , is in the middle of the regulating resistance, R_{sa} , as in the haemodynamic circuit first developed by Ursino et al. (2000). Alternatively, Lu et al. (2004) placed the compliance in front of the resistance, while others, de Mul et al. (2005), assumed that compliance comes after the resistance. All three use the lumped structure as a simplification of the real system: although they share the same steady response, their dynamic responses are quite different. Ursino et al.'s structure is preferred here because P_1 , which is another parameter to control the change of arterial volume (refer to Equation 3.2), can be kept almost constant with varying CBF because of the large and dominating value of regulating resistance, R_{sa} . In that case, the arterial volume is mainly controlled by the arterial compliance, which is the direct recipient of the stimulus feedback.

Though pressure autoregulation has been studied intensively in the literature, its interaction with CO_2 reactivity and BOLD response to neural activation is less well investigated, neither by experimental nor modelling methodology. By analysing the linear dynamic behavior of CHS, autoregulation was found to have a large effect on the cerebral vasculature response to both CO_2 reactivity and neural activation: $P_{aCO_2} - CBF$ and $P_{aCO_2} - BOLD$ transfer function analysis shows that autoregulation, corresponding to slow increase of CBF/BOLD to step changes of CO_2 , is consistent with the experimental results of Poulin et al. (1996, 1998); the linearised neural activity-BOLD signal model further links autoregulation with the experimentally observed prolonged post-stimulus BOLD undershoot (Friston et al. (2000); Cohen et al. (2002)). However, these hypotheses about the role of autoregulation in these processes still need direct experimental design and reliable measurements of CBF, BOLD and other crucial variables to be validated.

3.6 Summary

Starting from a combined haemodynamic system that predicts the haemodynamic response to changes in arterial blood pressure, arterial CO_2 concentration and neural stimulation very similar to that developed by Payne (2006), every compartment of the system has been carefully examined and evaluated. First, the model simulation results were generated and were found to be in agreement with available experimental data. Second, the effect of changes in ICP on the CBF and BOLD response was explored, suggesting that it cannot be neglected, especially in hypercapnia and hypocapnia. Finally, model simulations of autoregulation and the CBF and BOLD responses at different P_{aCO_2} states were compared with the existing experimental data, showing that the gain and time constant governing flow autoregulation and neural activity are not independent of CO_2 level.

By linearising the original nonlinear CHS model, the linear dynamic behavior of cerebral blood flow in response to both pressure changes and CO_2 reactivity has been examined and compared to experimental data taken from the literature. The complex flow feedback

mechanism acting on the arterial compliance of CHS is approximated as a second order transfer function for V_{MCA} in response to ABP changes, which is consistent with the experimental data. The crucial parameters influencing the speed of autoregulation have also been analysed and discussed, and thus might be estimated by the experimentally-derived IR and SR results. Besides CBF autoregulation, the BOLD response of CO_2 reactivity and neural activity based on CHS has been linearised and found to be in very good agreement with available experimental data. Especially, the success in predicting the prolonged BOLD undershoot illustrates the advantage of CHS in generating CBF through arterial compliance feedback system over other existing models.

CHS model simulations show that CBF/BOLD is controlled by multiple stimuli and thus, in clinical settings, it is necessary to consider the effects of other stimuli when attempting to identify the relationship between a particular stimulus and the CBF/BOLD responses. In the following chapters, both the nonlinear and linear models will be used as the basis for interpreting multivariate experimental data, where system identification techniques will be examined in detail and compared to the model predictions. The value of using this combined model-analysis approach will thus be clearly seen.

Multivariate system identification for cerebral Autoregulation

The effect of spontaneous beat-to-beat mean arterial blood pressure (ABP) fluctuations and breath-to-breath end-tidal carbon dioxide (P_{ETCO_2}) and end-tidal oxygen (P_{ETO_2}) fluctuations on beat-to-beat cerebral blood flow velocity (CBFV) variations is studied using a multiple coherence function. Multiple coherence is a measure of the extent to which the output, CBFV, can be represented as a linear time invariant system of multiple input signals. Analysis of experimental measurements from 13 different healthy subjects reveal that, with additional inputs, P_{ETCO_2} and P_{ETO_2} , the multiple coherence for frequencies $< 0.05\text{Hz}$ is significantly higher than the corresponding values obtained for univariate coherence with a single input of ABP. The result illustrates that the low value of univariate coherence at small frequencies may be due to the effects of P_{ETCO_2} and P_{ETO_2} fluctuations on CBFV variability. Moreover, it is also found that the transfer function between ABP and CBFV time series identified from previous univariate techniques at low frequencies can be modified by CO_2 and O_2 reactivity and no longer represents pressure autoregulation only. Multivariate system identification provides a technique of incorporating additional variability and recovering from this artifact. Finally, a physiologically-based model and its linear transfer function are used as a simulation tool to investigate possible causes

of low univariate coherence ¹.

4.1 Introduction

The autoregulation of cerebral blood flow, CBF , is normally defined as the ability of the brain to maintain adequate blood flow despite variations in a number of external factors such as arterial blood pressure, ABP , heart rate and respiration rate. Assessment of cerebral autoregulation is an important adjunct to measurements of cerebral blood flow for diagnosis, monitoring or prognosis of cerebrovascular disease, such as atherosclerosis. Given the high temporal resolution of transcranial Doppler ultrasound (TCD) which measures cerebral blood flow velocity, $CBFV$, normally in the middle cerebral artery, a large number of methods have been used to interpret the status of cerebral autoregulation by analysing the dynamic relationship between ABP and $CBFV$.

Existing work can be broadly divided into two approaches: linear and nonlinear. Linear techniques represent the ABP - CBF system as a transfer function and identification techniques are used to recover the model from data (Panerai et al. (1999, 2001); Zhang et al. (1998a)). It is generally hypothesized that the system behaves like a high-pass filter, i.e. variations in cerebral blood flow due to changes in arterial pressure are effectively damped in the low-frequency range whilst in the high frequency range, where autoregulation may be less effective, changes in arterial pressure may transfer simply to changes in cerebral blood flow (Zhang et al. (1998a)). Nonlinear models include high-order Volterra kernels (Panerai et al. (1999); Mitsis et al. (2002, 2004b)) and physiologically-based models, representing the nonlinearities from tissue elasticity and interactions with intracranial pressure (Ursino and Lodi (1998); Ursino et al. (2000); Payne (2006)). These models can be related to the transfer functions identified from the experimental data using a combined analysis, as described in Payne and Tarassenko (2006).

In linear transfer function analysis, the Frequency Response (FR) identified from experi-

¹This study has been published as Peng et al. (2007).

mental data has been widely used to characterize the system behaviour. The FR is comprised of three parameters: gain, phase and coherence. Gain represents the estimated scaling between the output and input as a function of frequency. Phase is a measure of the time delay normalized to one period. The squared coherence function is a measure of the fraction of the output power that can be linearly related to the input power, using the estimated transfer function, and thus is a good measurement of the linearity of the system. Existing studies appear to agree that the estimated frequency response of *ABP/CBFV* relationship below 0.50 Hz can be divided into three regions:

1. Low frequency (< 0.07 Hz): Low coherence, low gain and large phase lead.
2. Intermediate frequency (0.07 – 0.20 Hz): Increasing coherence, increasing gain and decreasing phase.
3. High frequency (> 0.20 Hz): High coherence, relatively large gain and minimal phase lead.

Gain and phase together can be used to reconstruct the Impulse Response (IR) through the inverse Fourier Transform. However, the spectral estimation of gain and phase is only accurate when the corresponding coherence is high. The observed low coherence in the low frequency band thus indicates that a linear time-invariant system model is not a valid representation of the dynamic of cerebral autoregulation in that range. Numerous authors use this experimentally observed low coherence in the low frequency band to question entirely the validity of transfer function estimation techniques for cerebral autoregulation (Latka et al. (2005); Rowley et al. (2007); Giller and Mueller (2003)). This has motivated many attempts to perform more sophisticated nonlinear system identification procedures on the system (Mitsis et al. (2002, 2004b)).

In contrast, Panerai *et al.* (Panerai et al. (2006)) argued that the low values of coherence in the low frequency region mean that the system is more effectively modelled as a multiple-input system, having blood flow as its output. The validity of a linear model must thus be assessed using a multiple coherence function. In Panerai et al. (2006), alongside *ABP*, an additive input cerebrovascular resistance index, *CVRI*, was introduced, defined

as $ABP/CBFV$. The result seems encouraging: the multiple coherence of $CBFV$ for low frequencies is found to be significantly higher than the corresponding values obtained with univariate coherence. However, since one system input, $CVRI$, is directly related to the output, it does not contribute to the validity of linear system relationship though it does artificially change the value of the coherence function.

It is also known that $CBFV$ variation is not entirely determined by pressure. Alongside cerebral pressure autoregulation, the other main mechanism responsible for controlling blood flow is the reactivity of cerebral vessels to arterial CO_2 (P_{aCO_2}) and O_2 (P_{aO_2}) levels. Since P_{aCO_2} and P_{aO_2} reactivity can be assessed by end-tidal CO_2 (P_{ETCO_2}) and end-tidal O_2 (P_{ETO_2}) measurements, a number of physiological studies have investigated the dynamic characteristics of the $CO_2 - CBFV$ relationship through measuring both the $CBFV$ response to a step change in P_{ETCO_2} (Poulin et al. (1996, 1998)) and the continuous recording of breath-by-breath spontaneous fluctuations in P_{ETCO_2} (Mitsis et al. (2004b); Panerai et al. (2000)). Mitsis *et al.* (Mitsis et al. (2004b)) modelled a multiple-input nonlinear system (with both ABP and P_{ETCO_2} as inputs) using the Laguerre-Volterra network methodology and demonstrated that CO_2 fluctuations, as well as the interactions between ABP and CO_2 have a considerable effect on $CBFV$ variation at low frequencies, which suggests ABP alone is not enough to explain low frequency $CBFV$ variability.

In this Chapter, we thus explore the cerebral system using two important physiological variables, P_{ETCO_2} and P_{ETO_2} , as extra inputs to the system. Multiple coherence is used to assess the validity of this multiple-input model, particularly in the low frequency range, to investigate the validity of performing linear system identification on this system. An existing Ordinary Differential Equation (ODE) model of cerebral autoregulation (Payne (2006)) is also used to simulate the effect of various hypotheses about the observed low univariate coherence in the transfer function identification process.

4.2 Method

4.2.1 Experimental Methods

Thirteen healthy subjects participated in the study. All subjects received verbal and written instructions outlining the experiment procedure; written informed content was obtained, studies conformed to the standards set by Declaration of Helsinki, and research study was approved by the Conjoint Health Research Ethics Board at the University of Calgary (Grant ID 15671). Participants were not taking any medication, all were non-smokers, and none had any history of cardiovascular, cerebrovascular, or respiratory disease. The experimental data were collected under supine, free-breathing conditions (Mitsis et al. (2004a)).

The experimental variables P_{ETCO_2} and P_{ETO_2} were monitored using a mass spectrometer (AMIS2000, Innovision, Odense, Denmark) and were sampled every 20ms. ABP was monitored continuously in the finger by photoplethysmography (Portapress, TPD Biomedical Instrumentation, the Netherlands). $CBFV$ was measured with a 2-MHz Doppler ultrasound system (TC22, SciMed, Bristol, U.K.) in the right middle cerebral artery. Both the pressure and velocity signals were sampled every 10 ms. The time series of all experimental variables were further resampled to 1Hz using cubic spline interpolation (a low-pass filtered with a cut-off frequency of 0.4Hz was applied to remove any frequency above Nyquist frequency prior to resampling). This frequency was chosen to be consistent with existing value widely used in the literature (Zhang et al. (1998a); Mitsis et al. (2004b,a)). The resampled data were then high pass filtered using a fifth-order Butterworth filter with a cut-off frequency of 0.005Hz to remove the very slow variation and baseline shift (Rowley et al. (2007); Mitsis et al. (2004b,a)). Sections of the time series having a duration of 2000 seconds were selected for spectral and transfer function analysis.

4.2.2 Mathematical Methods

From the time series for *ABP*, $P(t)$, and *CBFV*, $V(t)$, the frequency-domain transforms $P(f)$ and $V(f)$ were computed with an FFT algorithm. The power spectrum of $P(t)$, $G_{pp}(f)$, is calculated as:

$$G_{pp}(f) = E[P^*(f)P(f)], \quad (4.1)$$

where the expected value of the complex product $E[P(f) * P(f)]$ is obtained with the Welch technique (Welch (1967)) by smoothing the spectra with a 128-point (128-second) Hanning window with 50% overlap. Similarly, the cross-spectrum $G_{pv}(f)$ is computed as:

$$G_{pv}(f) = E[P^*(f)V(f)]. \quad (4.2)$$

The univariate coherence function $\Gamma_P^2(f)$ is estimated by:

$$\Gamma_P^2(f) = \frac{|G_{pv}(f)|^2}{G_{vv}(f)G_{pp}(f)}, \quad (4.3)$$

where $G_{vv}(f)$ is the power spectrum of $V(t)$. The squared coherence reflects the fraction of output power that can be linearly related to the input power at each frequency. Similarly to a correlation coefficient, it varies between 0 and 1: a value of 0 indicates that the output is linearly independent of the input whilst a value of 1 reveals a pure linear relationship between the input and output.

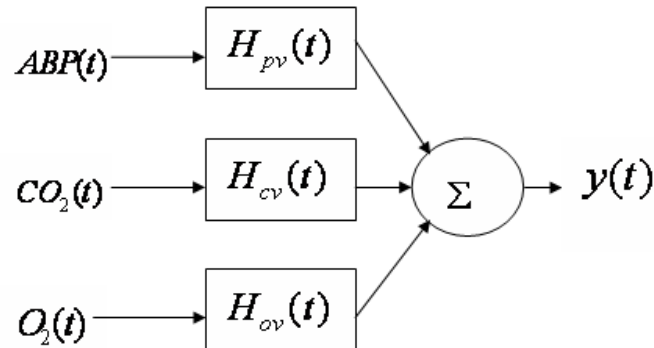
The complex transfer function $H(f)$ between $P(t)$ and $V(t)$, is given by:

$$H(f) = \frac{G_{pv}(f)}{G_{pp}(f)}. \quad (4.4)$$

However, in addition to *ABP*, P_{ETCO_2} and P_{ETO_2} are known to be physiological parameters that control the changes in velocity. Those can be added into the system as two extra inputs, as shown in Figure 4.1. The proportion of output that can be linearly related to the inputs is thus written as (Bendat and Piersol (2000)):

$$Y(f) = H_{PV}(f)P(f) + H_{CV}(f)C(f) + H_{OV}(f)O(f). \quad (4.5)$$

Figure 4.1 Schematic of the multiple-input system. Measured ABP , P_{ETCO_2} and P_{ETO_2} are model inputs and $y(t)$ is model output: model predicted $CBFV$.



Defining the matrix of autospectra and cross-spectra for the input signals as:

$$G_i = \begin{bmatrix} G_{PP} & G_{PC} & G_{PO} \\ G_{CP} & G_{CC} & G_{CO} \\ G_{OP} & G_{OC} & G_{OO} \end{bmatrix}, \quad (4.6)$$

the cross-spectra between the inputs and cerebral blood flow velocity as:

$$G_o = \begin{bmatrix} G_{PV} \\ G_{CV} \\ G_{OV} \end{bmatrix}, \quad (4.7)$$

and the vector of system partial transfer functions as:

$$H = \begin{bmatrix} H_{PV} \\ H_{CV} \\ H_{OV} \end{bmatrix}, \quad (4.8)$$

the corresponding autospectrum of the model output can be written in matrix form as (Bendat and Piersol (2000); Perreault et al. (1999)):

$$\begin{aligned} G_{YY}(f) &= E[Y^*(f)Y(f)] \\ &= H^T G_i H, \end{aligned} \quad (4.9)$$

where the different auto- and cross-spectra can be calculated according to Equations 4.1 and 4.2. The partial transfer function H can be estimated by solving the following matrix equation:

$$G_i * H = G_o. \quad (4.10)$$

The multiple coherence is defined as the ratio between the linear system output spectrum to the measured velocity spectrum (Bendat and Piersol (2000); Perreault et al. (1999)):

$$\Gamma_M^2(f) = \frac{G_{YY}(f)}{G_{VV}(f)}. \quad (4.11)$$

4.2.3 Simulation Study

A typical physiologically-based nonlinear model and its linear approximation were used to explore three possible reasons for the drops of coherence function: *1. noise; 2. nonlinearities; 3. contribution of additional inputs such as P_{ETCO_2} and P_{ETO_2}* . The detailed description of the nonlinear model used here can be found in Payne (2006). The linearised approximation of this model comprises transfer functions for $ABP - CBFV$ and $P_{ETCO_2} - CBFV$. The linearisation procedure can be found in Payne and Tarassenko (2006), and all equations are given in the Appendix. The simulation processes for both linear and nonlinear models comprise the following steps:

- 1. Measured ABP for a single patient is used as the single system input to predict CBFV. The univariate coherence between the model input and output is calculated at all frequencies.*
- 2. Total power spectral power in ABP and CBFV was calculated as the standard deviation of the ABP and predicted CBFV time series. The input and output Gaussian white noise are generated by two random time series with a uniform power over frequencies from 0 to 0.05 Hz, whose standard deviations are 10% of the standard deviation of ABP and predicted CBFV time series respectively. The input and output noise were added to model input and model output to mimic measurement noise, the univariate coherence then being obtained from the new signals with noise.*
- 3. Measured P_{ETCO_2} of the same patient is included as an extra system input. The univariate coherence between one model input, ABP, and model predicted CBFV is obtained. The multiple coherence between all model input signals and model output signals is also provided for comparison.*

4.3 Results

4.3.1 Experimental Study

The mean values of the ABP , P_{ETCO_2} , P_{ETO_2} and $CBFV$ time series, averaged over the 2000-second recordings for the 13 subjects, are given in Table 5.1, together with the inter-subject variability. Typical 5 minute data segments are shown in Figure 4.2, and the corresponding power spectra in Figure 4.3. Most of the ABP and $CBFV$ power is found below $0.1Hz$, while most of the P_{ETCO_2} and P_{ETO_2} power lies below $0.05Hz$.

Table 4.1 Mean Values (\pm Standard Deviation) for ABP , P_{ETCO_2} , P_{ETO_2} , and $CBFV$, averaged over 2000 second recording from 13 subjects

ABP [mm Hg]	P_{ETCO_2} [mm Hg]	P_{ETO_2} [mm Hg]	$CBFV$ [cm/sec]
76.6 ± 7.0	37.4 ± 1.8	87.7 ± 2.7	53.5 ± 5.2

Figure 4.2 Time series of typical data segments.

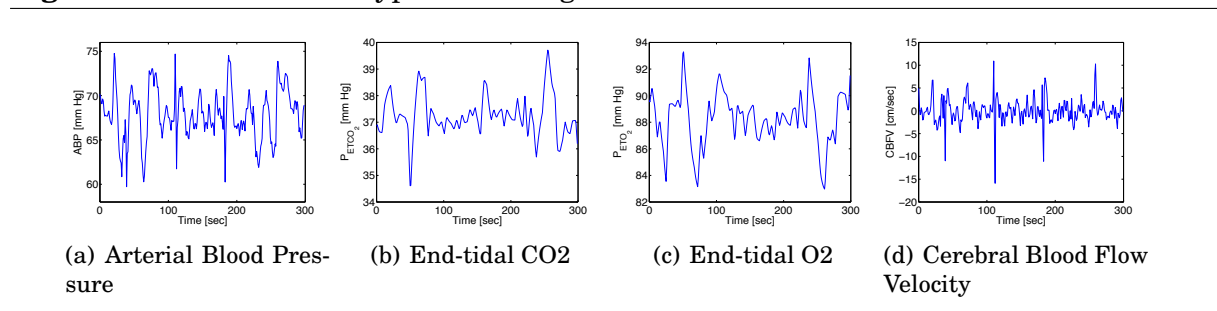


Figure 4.3 Power spectra of typical data segments.

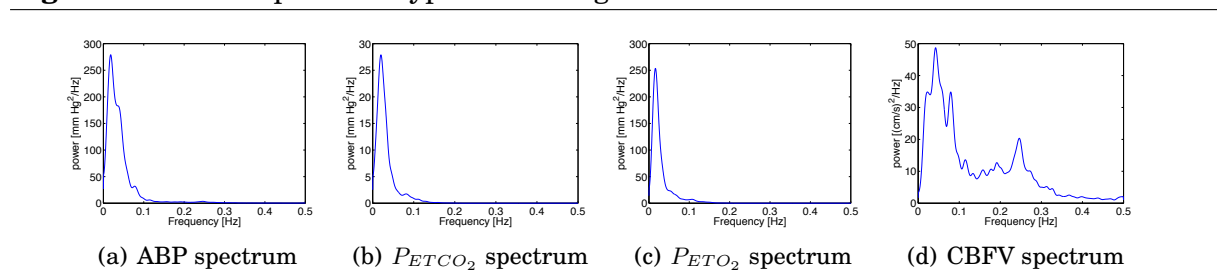
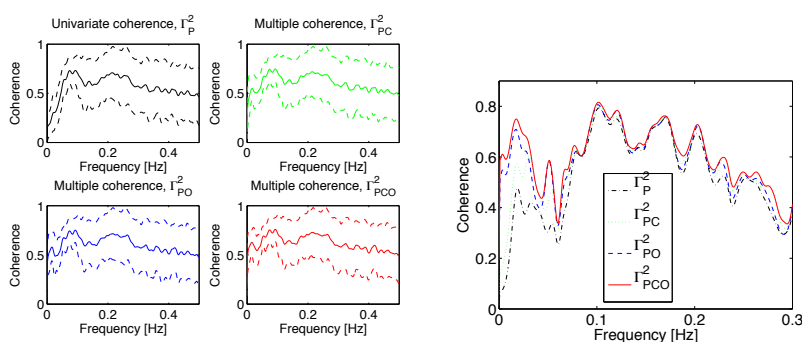


Figure 4.4(a) shows the univariate coherence between ABP and $CBFV$, the multiple coherences for the $ABP + P_{ETCO_2}$ inputs, $ABP + P_{ETO_2}$ inputs and $ABP + P_{ETCO_2} + P_{ETO_2}$ inputs (group mean value \pm standard deviation). The values of univariate coherence and multiple coherences for a typical subject and group mean values are also shown in Figure 4.4(b) and

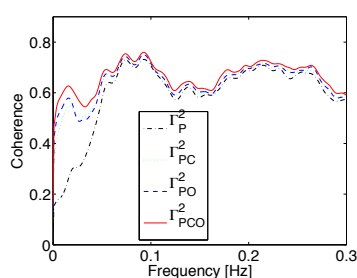
Figure 4.4(c) respectively. In the low frequency band, i.e. $< 0.05\text{Hz}$, the three multiple coherences ($ABP + P_{ETCO_2}$ inputs, $ABP + P_{ETO_2}$ inputs and $ABP + P_{ETCO_2} + P_{ETO_2}$ inputs) are all noticeably higher than the corresponding values for univariate coherence (ABP input), while no obvious difference between multiple coherence and univariate coherence is shown at higher frequencies, i.e. $> 0.05\text{Hz}$. This result illustrates that the contribution of P_{ETCO_2} and P_{ETO_2} terms and their interaction terms with ABP are found mainly at low frequencies, which is consistent with the results of Mitsis et al. (2004b).

Figure 4.4 Univariate coherence and multiple coherences for ABP input, $ABP + P_{ETCO_2}$ inputs, $ABP + P_{ETO_2}$ inputs and $ABP + P_{ETCO_2} + P_{ETO_2}$ inputs respectively. Solid line, averaged estimates; dotted line, \pm standard deviation. Black lines, univariate coherences with the single input ABP , Γ_P^2 ; green lines, multiple coherence with ABP and P_{ETCO_2} as inputs, Γ_{PC}^2 ; blue lines, multiple coherence with ABP and P_{ETO_2} as inputs, Γ_{PO}^2 ; red lines, multiple coherence with ABP , P_{ETCO_2} and P_{ETO_2} as inputs, Γ_{PCO}^2 .



(a) univariate coherence and multiple coherences (mean value \pm standard deviation)

(b) typical subject



(c) group averaged values

A paired t-test (see Goulden (1959)) was then used to analyze the statistical significance of the difference between the univariate coherence and multiple coherences. The p-value at each frequency is shown in Figure 4.5. Since five independent hypotheses are tested on one

data set, the Bonferroni method is used to correct the statistical significance level. In order to achieve simultaneous p-values of 0.05, a stricter individual p-value of 0.01 is used for each pair. Figure 4.5(a) illustrates that multiple coherences ($ABP + P_{ETCO_2}$, $ABP + P_{ETO_2}$ and $ABP + P_{ETCO_2} + P_{ETO_2}$) are significantly increased in the low frequency band ($0 - 0.04Hz$) compared with the univariate coherence with single input ABP . However, the multiple coherence of three inputs is not significantly different from the multiple coherence of two inputs (Figure 4.5(b)). This indicates that considering only P_{ETCO_2} or P_{ETO_2} is sufficient to obtain a representation of the low frequency system dynamics. An additional input does not add significantly more information. This is reflected in the fact that P_{ETCO_2} and P_{ETO_2} fluctuations are highly correlated.

Figure 4.5 P-value of paired t-test of the hypothesis that the mean value of univariate coherence and multiple coherence is the same. P-values less than 0.01 were accepted as statistically significant.

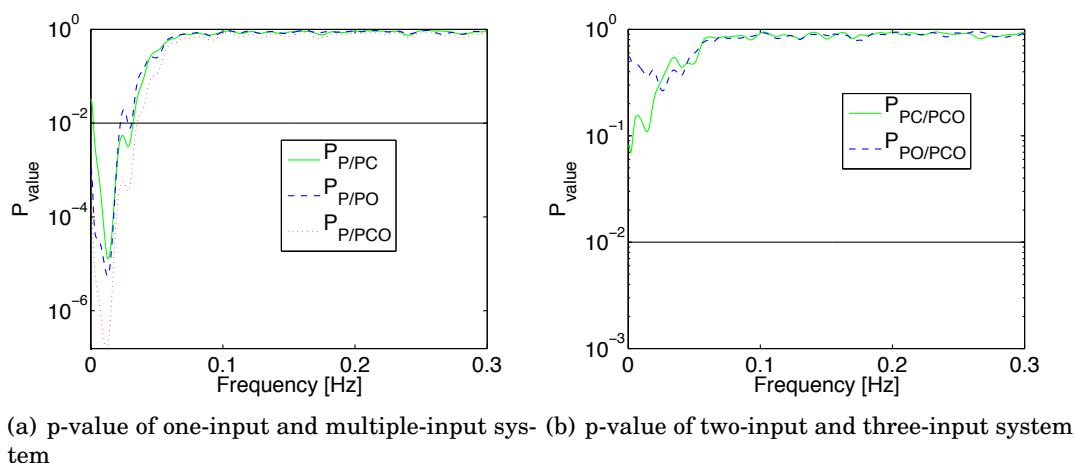


Figure 4.6 shows the spectrum of the measured $CBFV$ and spectrum of the residue (the difference between measurement and system prediction) of both the univariate system and the multivariate system. The high values of residue of the single input system over low frequencies indicates that most of the $CBFV$ power in the low frequency range is not linearly transformed from ABP alone. The reduced residue of the multivariate system in that frequency range reflects the fact that it can be explained better by the combination of ABP and other important physiological parameters such as P_{ETCO_2} and P_{ETO_2} . The

fact that there is still spectral power in the residue perhaps illustrates nonlinearities as explored in Mitsis et al. (2004b) or nonstationarities as explored in Latka et al. (2005) and Rowley et al. (2007), or may be due to the effects of other unmeasured physiological parameters.

Figure 4.6 Spectra of measured *CBFV* and model residue (univariate system and multivariate system).

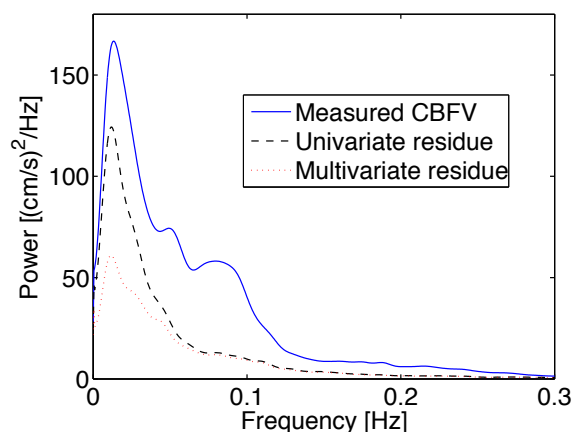


Figure 4.7(a) shows the group-averaged normalized cross spectra of $ABP - P_{ETCO_2}$ and $ABP - P_{ETO_2}$, having peak values of approximately $22Hz^{-1}$ and $66Hz^{-1}$ respectively. The high peak value of the cross spectra illustrates that it is unlikely that their effect on transfer function identification is negligible. Figure 4.7(c) shows the identified $ABP/CBFV$ transfer function, H , both for the single-input system and the multiple-input system. It is important to illustrate here the clinical significance of taking these multiple inputs into account. The dotted line in Figure 4.7(c) shows the frequency response of Tieck's model (Tiecks et al. (1995)), a widely used model to obtain autoregulation index by parametric fitting of time series from experimental data. The frequency responses of the two different transfer functions are thus fitted to the amplitude of frequency response (gain) of Tieck's model and the obtained autoregulation indexes (ARI) presented. This illustrates that, since the estimated gain in the low frequency band is lower with the contribution of cross-terms, the best fit values of ARI of the two transfer functions are also different. The ARI calculated without the cross-term is 3, whilst with the cross-term is 4. For some subjects

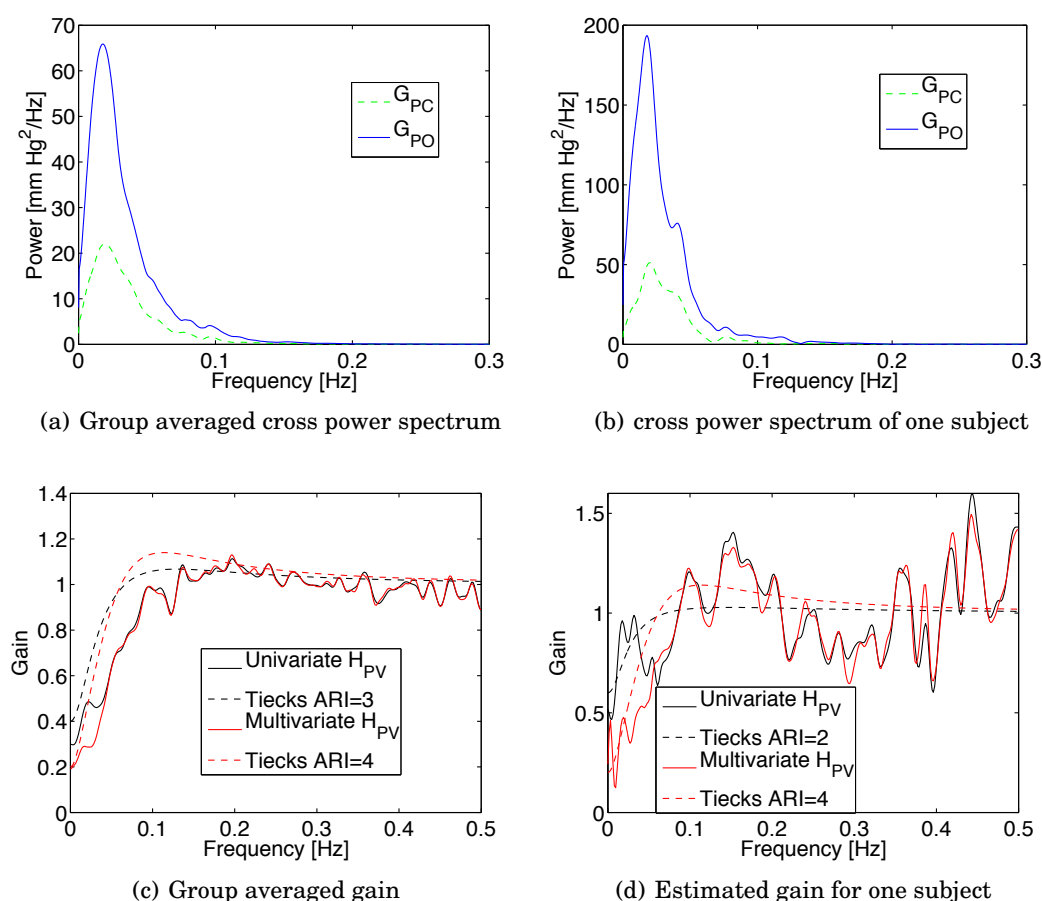
which have a relatively high correlation between ABP and P_{ETCO_2} or P_{ETO_2} , as shown in Figure 4.7(b), the difference in the estimated gain becomes larger, as shown in Figure 4.7(d). The univariate estimated transfer function of $ABP - CBFV$ behaves more like an all-pass filter whilst for the multivariate system it is still a high-pass filter. The fitted ARI of the former transfer function is only 2, which is supposed to represent impaired autoregulation status, whilst with the corrected multiple-input system, the fitted ARI is 4, which is within the healthy range. This clearly illustrates that the contribution of cross-terms is very important in the low frequency band and could lead to an incorrect classification of autoregulation status when they are not considered. Again, this is consistent with the results of Mitsis et al. (2004b).

4.3.2 Simulation Study

Figure 4.8(a) and Figure 4.8(b) show the coherence function between the model input, measured ABP , the model output, predicted $CBFV$, for the linear and nonlinear models respectively. For the case of a single input, ABP , the univariate coherence for the linear system is 1 at all frequencies², whilst the coherence for the nonlinear system is slightly reduced. For the case of an extra input, P_{ETCO_2} , the univariate coherence between ABP and $CBFV$ decreases in the low frequency band for both the linear and nonlinear systems, whilst multiple coherence remains the same as it accounts for the contribution of CO_2 . The effect of white noise is also reflected by a reduction in coherence, especially in the high frequency range. This might be due to the lack of high frequency power of the input signal. The simulation result illustrates that nonlinearity is not the only factor resulting in low coherence, as other factors such as an unmeasured input or noise can also play an important role in affecting the coherence. A number of existing models of cerebral autoregulation are in fact linear when considering spontaneous oscillations in blood pressure. The results of this simulation study appear to show that unmeasured variability rather than nonlinearity

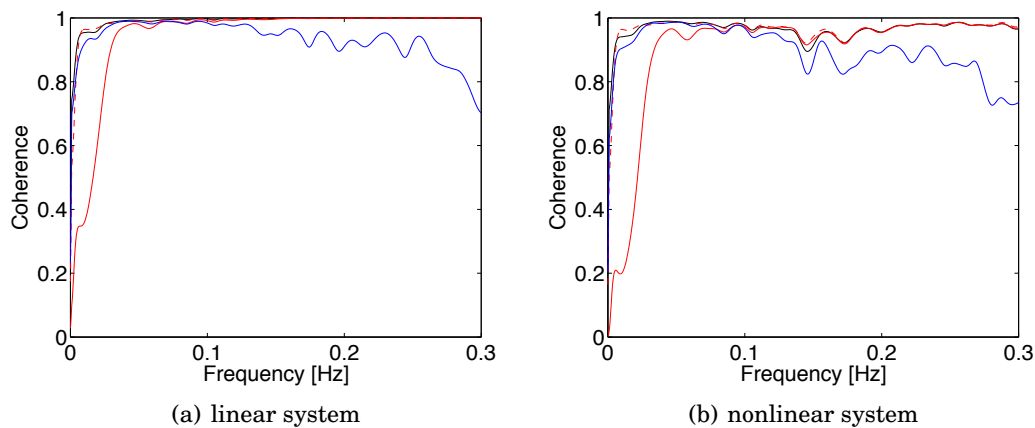
²Note that to remove baseline drift the signals were high-pass filtered as $0.005Hz$ (see Methods). This explains the sharp drop in coherence at very low frequencies.

Figure 4.7 a) The group averaged cross power spectrum between ABP and P_{ETCO_2} , G_{PC} (green line) and the group averaged cross power spectrum between ABP and P_{ETO_2} , G_{PO} (blue line). b) Cross power spectra G_{PC} (green line) and G_{PO} (blue line) for one subject. c) The group-averaged estimated transfer function gains for $ABP - CBFV$ for univariate system (black continuous line) and multivariate system (red continuous line). The corresponding fitted Tiecks autoregulation indexes are also shown in the figure: $ARI = 3$ for univariate system (black dotted line); $ARI = 4$ for multivariate system (red dotted line). d) The estimated transfer function gains for a particular subject with cross power spectrum shown in figure 4.7(b) for univariate system (black continuous line) and multivariate system (red continuous line). The fitted Tiecks autoregulation index: $ARI = 2$ for univariate system (black dotted line); $ARI = 4$ for multivariate system (red dotted line). A relatively large value of cross-term results in a noticeable difference between the estimated gains in the low frequency range.



is a more plausible explanation for low univariate coherence.

Figure 4.8 Model simulation. a) Coherences for linear model inputs and output. Univariate coherence with single model input, *ABP* (black line); univariate coherence between *ABP* and *CBFV* (red continuous line) and multiple coherence (red dotted line) with multiple inputs *ABP* and P_{ETCO_2} ; univariate coherence between surrogated *ABP* and surrogated *CBFV* for single input system, with 10% noise added to both model input and output. b) Coherence for nonlinear model input and output. Similar to linear model, univariate coherence for single-input system (black line); univariate coherence between *ABP* and *CBFV* (red continuous line) and multiple coherence (red dotted line) for multiple-input system; univariate coherence between surrogated *ABP* and surrogated *CBFV*, with 10% noise adding to both model input and output.



4.4 Discussion

Many investigators have attempted to characterize the *ABP/CBFV* relationship with various linear methods (Zhang et al. (1998a); Tiecks et al. (1995); Panerai et al. (1999); Liu et al. (2003)). The observed low univariate coherence found at low frequencies, which are those of most clinical interest, has always constrained the use of these linear methods. A number of researchers have thus questioned the validity of linear techniques and attempted to identify the system dynamics with more advanced and complex nonlinear analysis methods (Mitsis et al. (2002, 2004b); Giller and Mueller (2003)). We have shown here that by considering the contribution of CO_2 and O_2 to *CBFV*, the coherence is significantly increased at low frequencies, which improves the validity of linear techniques. In other words, some of the apparent nonlinearity can be attributed to unmeasured vari-

ability. Whether the system will appear to be less stationary due to these system inputs is another important issue, which will be presented in Chapter 5.

CO₂ and O₂ reactivity

It is well known that cerebral blood flow is modulated by changes in arterial CO_2 and O_2 (Renkin and Michel (1983); Paulson et al. (1990)). With the recent development of techniques used to measure cerebral blood flow and to control arterial gases continuously, a number of studies have focused on the assessment of dynamic changes in cerebral blood flow to changes in $PaCO_2$ and PaO_2 , for example, Mitsis et al. (2004b); Poulin et al. (1996, 1998); Panerai et al. (2000). Panerai et al. (Panerai et al. (2000)) found that spontaneous breath-to-breath changes in $PaCO_2$ can contribute significantly to the observed $CBFV$ variability as the correlation of model predicted $CBFV$ and measured $CBFV$ improved after adding CO_2 as an additive model input. Mitsis et al. (Mitsis et al. (2004b)) further pointed out that the contribution of P_{ETCO_2} terms and interaction terms are mainly found in the low frequency band, while ABP terms act mainly at high frequencies. The results presented here (Figure 4.4) are consistent with these previous findings. The increased multiple coherence in the low frequency band reflects the contribution of the linear P_{ETCO_2} and interaction terms. Mitsis et al. (Mitsis et al. (2004b)) use NMSE, defined as the normalized error between model output and measurement, to assess the contribution of both linear and nonlinear terms. Because of a different signal processing methodology, it is difficult to compare their result with ours quantitatively.

Using a physiologically-based model, we have shown that it is plausible that the univariate coherence of $ABP - CBFV$ is reduced by the presence of end tidal P_{ETCO_2} disturbances, which mimic how P_{ETCO_2} fluctuations influence flow autoregulation. The dynamic effects of P_{ETO_2} on $CBFV$ are less emphasized, partly because P_{ETO_2} fluctuations are highly correlated to P_{ETCO_2} . The linear information content in P_{ETCO_2} and P_{ETO_2} is not identical, illustrated by the small change in multiple coherence; however, this difference is not significant for our subject group.

Multiple-input system and multiple coherence

In the study of dynamic cerebral pressure autoregulation, the system comprising blood pressure as input and velocity as output is now a standard model (Giller and Mueller (2003)) and transfer function analysis has often been adopted to quantify this relationship. The fundamental assumption for the estimation of transfer function gain and phase is system linearity, quantified by using coherence. The observed low univariate coherence shows that the system is not adequately represented by a linear time invariant relationship and hence the system is either not univariate, or nonlinear, or nonstationary.

Multiple coherence theory developed previously (Bendat and Piersol (2000)) can be used to address the first problem and assess the extent of linear time invariance. Similar to univariate coherence, multiple coherence measures the ratio of output power that can be linearly related to input variables at each frequency. For a multiple-input single-output linear time-invariant system, multiple coherence should be close to 1 at all frequencies. Low univariate coherence between one input signal and one output signal at any frequency may be observed if most power at that particular frequency in the output signal is transformed from other input signals. Figure 4.8(a), using a simulation study, is a good example of this case: even for a pure linear system, the univariate coherence between ABP and model predicted $CBFV$ is reduced because most of the model output power in the low frequency band is transformed from P_{ETCO_2} rather than ABP . In the real system governing $CBFV$ variation, we have here illustrated that the low value of univariate coherence between ABP and $CBFV$ at low frequencies may be explained by the effects of other inputs of system such as P_{ETCO_2} and P_{ETO_2} because the corresponding values for multiple coherence are high after considering their contribution to $CBFV$ variability.

Panerai *et al.* (Panerai *et al.* (2006)) showed that by introducing a second derived variable, $CVRI$, multiple coherence could be increased using only univariate measures. We have argued that multiple measurements must be taken to set an accurate estimation of the transfer function. We now examine why the use of a derived variable is not sufficient in this case. Considering two inputs: ABP and resistance index $CVRI$, defined as $ABP/CBFV$;

and one output, $CBFV$, the system in Panerai et al. (2006) is written as:

$$V(f) = H_1(f)P(f) + H_2(f)R(f), \quad (4.12)$$

where $H_1(f)$ and $H_2(f)$ are the partial transfer functions for $ABP - CBFV$ and $CVRI - CBFV$.

For small changes around the basal condition, ΔR , can be expanded as a Taylor series:

$$\frac{\Delta CVRI}{CVRI} = \frac{\Delta ABP}{ABP} - \frac{\Delta CBFV}{CBFV}. \quad (4.13)$$

Equation 4.13 can be written in the frequency domain as:

$$R(f) = P(f) - V(f) \quad (4.14)$$

Thus Equation 4.12 becomes:

$$\begin{aligned} V(f) &= H_1(f)P(f) + H_2(f)(P(f) - V(f)) \\ &= (H_1(f) + H_2(f))P(f) - H_2(f)V(f). \end{aligned} \quad (4.15)$$

Equation 4.15 illustrates that the system with two inputs (ABP and R) is equivalent to the system with two inputs (ABP and $CBFV$). By definition, multiple coherence will be unity for a multivariate system in which one system input is linearly related to the output (Bendat and Piersol (2000)). After rearrangement, Equation 4.15 becomes:

$$\begin{aligned} V(f) &= \frac{H_1(f) + H_2(f)}{1 + H_2(f)}P(f) \\ &= H(f)P(f). \end{aligned} \quad (4.16)$$

Equation 4.16 shows that this multiple-input system is the same as the single-input system for small changes in ABP , illustrating that a derived parameter such as $CVRI$ does not contribute to a better understanding of the dynamic determinants of $CBFV$.

Cross-term and transfer function identification

Some researchers think the interactions between ABP and P_{ETCO_2} are small and negligible (Panerai et al. (2000)). Others have emphasized the significance of the cross-term,

which was found to account for a large part of the total model prediction power (Mitsis et al. (2004b)). Our result is consistent with the result of Mitsis et al. (2004b), and we have further showed that most of the cross spectrum power between ABP and P_{ETCO_2} is concentrated at low frequencies and that it will affect the results of the transfer function identification and autoregulation index estimation. In fact, the effects of uncorrelated and correlated noise on transfer function analysis are different: the former will reduce the coherence, but does not affect the identified transfer function, whilst the latter will affect both. In other words, any unmeasured variable will influence the coherence, but only those which are correlated to ABP will affect the transfer function identification if not accounted for. As shown in Figure 4.7, the result of ARI estimation is clearly affected by the presence of significant cross power between ABP and P_{ETCO_2} .

Nonlinear effects

Many previous studies focused on the question of whether the dynamic system of cerebral autoregulation is best considered to be linear or nonlinear. Giller *et al.* (Giller and Mueller (2003)) argued that the $ABP/CBFV$ system is nonlinear because of five main reasons:

1. *Low coherence at low frequencies.*
2. *Spontaneous oscillations observed in velocity are independent of the pressure.*
3. *Highly nonstationary velocity and blood pressure signals.*
4. *Presence of bifurcations and chirps.*
5. *Failure of ARX and OE models³.*

We have showed that the univariate coherence between ABP and $CBFV$ can be low because the contribution of other physiological variables such as P_{ETCO_2} and P_{ETO_2} that drive $CBFV$ variability has not been properly considered. Since ABP is not the only determinant of $CBFV$ fluctuations, it is natural that there exist spontaneous oscillations in $CBFV$ that are independent of pressure. We have illustrated that to some extent these oscillations may be due to CO_2 variability. It is also possible that these oscillations arise from vasomotion, a point we will refer to later. For the third reason, even with a time

³The model definitions can be found in Dutton et al. (1997).

invariant system from pressure to velocity, a highly non-stationary pressure signal will produce a highly non-stationary flow signal. The algorithm we have presented here tests the validity of a linear time-invariant relationship identified from the data. High values of coherence suggest that the data used in this study may be considered approximately stationary. The failure of ARX and OE models might well also be due to an unmeasured variability. Bifurcation and chirps were defined in Giller and Mueller (2003) as a splitting of the frequency content into two sub-bands at a point in time, and a linear increase in the frequency of most power in the signal with time. It should be noted that since a short time FFT is a moving average observation; any changes in frequency will appear smoothed; and therefore smoothness of frequency changes in this are infact an artifact of the process and should not be interpreted as significant results. Changes of the frequency content of *CBFV* are to be expected when the system is driven by multiple inputs.

Although Volterra kernels have been used to characterize the nonlinearities in *ABP/CBFV* system (Panerai et al. (1999); Mitsis et al. (2002, 2004b)), it is difficult to gain physical insights from this non-parametric approach (Panerai et al. (1999); Giller and Mueller (2003)). Another approach is the use of physiologically-based models which include nonlinearities from tissue elasticity and interactions with intracranial pressure, such as the models of Ursino and Lodi (1998), Ursino et al. (2000) and Payne (2006). The effect of the built-in nonlinearities is reflected by the reduced coherence over all frequencies comparing to the coherence for the linear model, as shown in Figure 4.8(b). However, this difference is not significant, illustrating that these nonlinear models behave more linearly when considering spontaneous oscillations. Comparing nonlinearities, the more significant coherence reduction is due to the effect of an extra system input, CO_2 . In fact, the active pressure autoregulation system can be considered as a high-pass filter and the transfer of low frequency *ABP* fluctuations to *CBFV* variability is successfully blocked. In contrast, CO_2 reactivity mechanisms behave like a low-pass filter which allows only the CO_2 power at low frequencies to transmit to *CBFV*. As a result, in the low frequency band of *CBFV*, *ABP* is no longer the dominant determinant, which is reflected by the reduced univariate

coherence between ABP and $CBFV$. However, multiple coherence remains high because it includes the contribution of CO_2 to $CBFV$ variability. The model simulations (Figure 7.7) support this explanation.

Other mechanisms of control of cerebral blood flow

Besides pressure autoregulation and CO_2 reactivity, vasomotion and neural activity are known to be other mechanisms which have an effect on cerebral blood flow. Vasomotion is defined as rhythmic oscillations in vascular tone caused by vascular smooth muscle constriction and dilation. The origin of vasomotion is still not clear, but it has been found to correlate with blood pressure and neural or humoral input. Its intensity and quantity, or even presence is highly variable according to the results of available experiments (Nilsson and Aalkjaer (2003)).

Neural activity is well known to control of local blood flow supply, which is the foundation of many neuroimaging techniques including Near Infra-Red Spectroscopy (NIRS) and functional magnetic resonance imaging (fMRI). For spontaneous fluctuations of blood flow, neural activity can be also an important controlling mechanism. Zhang *et al.* (Zhang *et al.* (2002)) showed the estimated transfer function gain and phase were altered by the removal of autonomic neural activity using ganglion blockade. It has been suspected that beat-to-beat fluctuations in sympathetic nerve activity may modulate cerebral autoregulation status and contribute to $CBFV$ variability. We notice there is still considerable residue in the multiple-input system, which might be due to vasomotion and neural activity. However, any firm conclusion will require more accurate measurement of these variables and will thus need to be investigated in the future.

Wavelet phase synchronization analysis of cerebral blood autoregulation

The dynamic relationship between beat-to-beat mean arterial blood pressure (ABP) fluctuations and cerebral blood flow velocity (CBFV) variations has been intensively studied. The experimentally observed low coherence in the low frequency band has previously indicated that the assumptions of linearity and/or stationarity, the preconditions of the linear transfer function analysis, are not valid in that frequency region. Latka et al. (2005) used a wavelet phase synchronization method to identify the instantaneous phase difference between ABP and CBFV and low values of synchronization index were found in the low frequency range, seeming to provide further evidence that the cerebral autoregulation system is nonstationary. Here we focus on another possible factor corresponding for this low synchronization index–unmeasured variability. We demonstrate analytically and with a physiologically-based cerebral hemodynamic model that, in the case of multiple inputs, the phase difference between one input, ABP, and the output, CBFV, will be distorted by an additional input, end-tidal CO_2 (P_{ETCO_2}), and no longer accurately represent the true ABP – CBFV system phase shift. We also prove that this phase distortion can be corrected if the transfer functions for ABP – CBFV and P_{ETCO_2} – CBFV are known or can be estimated. A significantly increased value of synchronization index in the low frequency band

is found using the CO_2 correction term with experimental data on thirteen subjects. This essentially indicates that the lack of synchronization between ABP and $CBFV$ previously identified by Latka et al. (2005) can be partly attributed to unmeasured variability¹.

5.1 Introduction

An important protective feature of the cerebral circulation is the ability to maintain cerebral blood flow, CBF , despite variations in a number of external factors such as arterial blood pressure, ABP , heart rate and respiration rate (Paulson et al. (1990)). If cerebral autoregulation is impaired, abnormally low or excessive CBF can lead to cerebral ischemia, intracranial hypertension or even capillary damage, thus contributing to the onset of cerebrovascular events. Thus, assessment of cerebral autoregulation becomes an important issue for diagnosis, monitoring or prognosis of cerebrovascular disease. Given the high temporal resolution of transcranial Doppler ultrasound (TCD) which measures cerebral blood flow velocity, $CBFV$, normally in the middle cerebral artery, a body of literature has attempted to assess the status of cerebral autoregulation by analysing the dynamic relationship between ABP and $CBFV$.

Linear transfer function analysis (Panerai et al. (1999, 2001); Zhang et al. (1998a)) is a standard model for cerebral hemodynamics. Within this framework, cerebral autoregulation is considered to be a high-pass filter that transmits rapid changes in blood pressure but dampens and delays low-frequency perturbations (Zhang et al. (1998a); Latka et al. (2005)). For ABP as the filter input and $CBFV$ as the output, transfer function identification techniques have been widely used to recover the filter parameters (gain and phase) from experimental data. However, the spectral estimation of gain and phase is only accurate when the corresponding coherence is high. The observed low coherence in the low frequency band thus indicates that a univariate linear time-invariant system model is not

¹This study has been accepted for publication as Peng et al. (2008b)

a valid representation of the dynamic of cerebral autoregulation in that range.

Numerous authors use this experimentally observed low coherence in the low frequency band to question entirely the validity of transfer function estimation techniques for cerebral autoregulation (Latka et al. (2005); Giller and Mueller (2003); Rowley et al. (2007)). The identified (or suspected) nonlinear and nonstationary relationship between *ABP* and *CBFV* has motivated many attempts to perform more sophisticated system identification procedures on the system including high order Volterra kernels (Mitsis et al. (2002, 2004b)) and phase synchronization methods (Latka et al. (2005)). The latter mathematical framework is based on wavelet decomposition, which allows for the identification and characterization of time varying phase difference. Strong phase difference variability between *ABP* and *CBFV* was found in the low frequency range, suggested by the low value of synchronization index.

However, the relationship between *ABP* and *CBFV* time series in the low frequency region is not entirely determined by pressure autoregulation. Alongside cerebral pressure autoregulation, the other main mechanism responsible for controlling blood flow is the reactivity of cerebral vessels to arterial CO_2 and O_2 levels, which are assessed by breath-to-breath end-tidal CO_2 (P_{ETCO_2}) and O_2 (P_{ETO_2}) measurements. Mitsis *et al.* (Mitsis et al. (2004b)) and Peng *et al.* (Chapter 4) have investigated the dynamic characteristics of the *CBFV* variability and a considerable proportion of low frequency *CBFV* fluctuations can be attributed to P_{ETCO_2} fluctuations and the interaction between *ABP* and P_{ETCO_2} . In particular, Peng *et al.* (Chapter 4) built a linear time-invariant system of multiple inputs: *ABP*, P_{ETCO_2} and P_{ETO_2} . Multiple coherence was used to assess the validity of this multivariate system and it was found that the multiple coherence for frequencies $< 0.05Hz$ is significantly higher than the corresponding values obtained for univariate coherence with a single input of *ABP*. This illustrates that, alongside nonlinearity and nonstationarity, unmeasured variability is also an important factor resulting in low univariate coherence. Similar to univariate coherence, a low value of univariate synchronization index might be also due to the effects of unmeasured parameters.

In this Chapter, we thus explore the validity of performing a univariate phase synchronization analysis on the cerebral system in the presence of another variable, P_{ETCO_2} (P_{ETO_2} is not included here because in this same data set, P_{ETO_2} fluctuations were found to be highly correlated to P_{ETCO_2} fluctuations and do not provide significantly more information to $CBFV$ variability (Chapter 4)). A mathematical formula of the error of the algorithm is deduced, showing that if the two transfer functions $ABP - CBFV$ and $P_{ETCO_2} - CBFV$ are known or can be estimated, the error of wavelet phase difference can be corrected. This is demonstrated by both synthetic and real data.

5.2 Method

5.2.1 System definition

As mentioned in Section 5.1, $CBFV$ is controlled by both ABP and P_{ETCO_2} fluctuations. Thus the cerebral system can be written as:

$$V(t) = P(t) \otimes h_{PV}(t) + C(t) \otimes h_{CV}(t) + n(t) \quad (5.1)$$

where $P(t)$ is the ABP time series, $C(t)$ is the P_{ETCO_2} time series, $V(t)$ is the $CBFV$ time series; h_{PV} and h_{CV} are the impulse responses of the system relating $ABP - CBFV$ and $P_{ETCO_2} - CBFV$ respectively; $n(t)$ is the noise term, including other unmeasured variability, such as vasomotion and mental activity, and instrument induced noise; the symbol \otimes represents the convolution operator.

5.2.2 Multivariate transfer function analysis

The relationship between system inputs, ABP and P_{ETCO_2} , and system output, $CBFV$, is evaluated using multivariate transfer function analysis. The component of the output that can be linearly related to the inputs is thus written as:

$$Y(f) = H_{PV}(f)P(f) + H_{CV}(f)C(f) \quad (5.2)$$

in which $P(f)$ and $C(f)$ are frequency-domain transforms of $P(t)$ and $C(t)$ respectively. H_{PV} and H_{CV} are partial transfer functions, which can be obtained by solving the following matrix equation (Chapter 4):

$$G_i * H = G_o, \quad (5.3)$$

in which $G_i = \begin{bmatrix} G_{PP} & G_{PC} \\ G_{CP} & G_{CC} \end{bmatrix}$, the matrix of autospectra and cross-spectra of the input signals, $G_o = \begin{bmatrix} G_{PV} \\ G_{CV} \end{bmatrix}$, the matrix of cross-spectra of the input and output signals, and $H = \begin{bmatrix} H_{PV} \\ H_{CV} \end{bmatrix}$, the vector of system partial transfer functions.

Multiple coherence is defined as the ratio between the linear system output spectrum and the measured velocity spectrum, which is:

$$\Gamma_M^2(f) = \frac{G_{YY}(f)}{G_{VV}(f)}, \quad (5.4)$$

in which $G_{YY}(f) = H^T G_i H$.

5.2.3 Wavelet phase synchronization method

Continuous complex Morlet wavelet transforms can be performed for $P(t)$, $C(t)$ and $V(t)$, giving the complex time series, $W_P(a, t)$, $W_C(a, t)$ and $W_V(a, t)$, as a function of wavelet scale a and time t (Le Van Quyen et al. (2001)). The complex argument of these time series gives a representation of the instantaneous phases, $\phi_P(a, t)$, $\phi_C(a, t)$ and $\phi_V(a, t)$. Taking the difference allows instantaneous phase difference to be calculated as:

$$\Delta\phi_P(a, t) = \phi_V(a, t) - \phi_P(a, t), \quad (5.5)$$

$$\Delta\phi_C(a, t) = \phi_V(a, t) - \phi_C(a, t). \quad (5.6)$$

To analyse synchronization between ABP and $CBFV$ time series, the circular mean, $\Delta\bar{\phi}_P(a)$ of the phase difference over the duration of a test segment can be calculated using (Rowley et al. (2007)):

$$\Delta\bar{\phi}_P(a) = \tan^{-1} \left\{ \frac{\sum_t \sin(\Delta\phi_P(a, t))}{\sum_t \cos(\Delta\phi_P(a, t))} \right\}. \quad (5.7)$$

The synchronization index, $\gamma_P(a)$ (Latka et al. (2005)), which is an inverse circular statistical analogue of variance is calculated using:

$$\gamma_P(a) = \frac{1}{N}([\sum_t \cos(\Delta\phi_P(a,t))]^2 + [\sum_t \sin(\Delta\phi_P(a,t))]^2), \quad (5.8)$$

in which N is the number of time points in the series. $\Delta\phi_C(a)$ and $\gamma_C(a)$ can be calculated in the same way and be used to analyse the synchronization between P_{ETCO_2} and $CBFV$. The value of synchronization index lies in the interval $0 \leq \gamma \leq 1$ and varies with the scaling parameter, a . In the case of perfect phase synchronization, i.e. $\phi_V(a,t) - \phi_P(a,t) = constant$, $\gamma_P(a) = 1$. In contrast, when the distribution of the phase differences is uniform, the time average of both trigonometric functions are zero, which leads to a zero synchronization index. A high value of synchronization index thus indicates that the phase difference between the two signals at any given frequency has a low variation over time.

5.2.4 Phase distortion by another variable

However, for the multivariate system in the presence of another input $C(t)$, the phase difference $\Delta\phi_P$ does not necessarily represent the instantaneous phase of $h_{PV}(t)$, denoted by ψ_{PV} . Suppose that the inputs to the system (Equation 5.1) are sinusoidal with an angle frequency of ω :

$$P(t) = A_P \cos(\omega t + \phi_P), \quad (5.9)$$

$$C(t) = A_C \cos(\omega t + \phi_C), \quad (5.10)$$

with the instantaneous phase of the primary input, $P(t)$, taken as the reference, i.e. $\phi_P = 0$, thus the output will be:

$$\begin{aligned} V(t) = & A_P |H_{PV}(e^{i\omega})| \cos(\omega t + \psi_{PV}) + \\ & A_C |H_{CV}(e^{i\omega})| \cos(\omega t + \phi_C + \psi_{CV}) + A_n \cos(\omega t + \phi_n), \end{aligned} \quad (5.11)$$

where:

$$\psi_{PV} = \angle H_{PV}(e^{i\omega}), \quad (5.12)$$

$$\psi_{CV} = \angle H_{CV}(e^{i\omega}). \quad (5.13)$$

H_{PV} and H_{CV} are the transfer functions for $ABP - CBFV$ and $P_{ETCO_2} - CBFV$ respectively.

The instantaneous phase difference that would be recovered using a wavelet phase estimator between ABP and $CBFV$ is:

$$\begin{aligned} \Delta\phi_P(t) &= \phi_V(t) \\ &= \tan^{-1} \left\{ \frac{A_P |H_{PV}| \sin\psi_{PV} +}{A_P |H_{PV}| \cos\psi_{PV} +} \right. \\ &\quad \left. \frac{A_C |H_{CV}| \sin(\phi_C + \psi_{CV}) + A_n \sin\phi_n}{A_C |H_{CV}| \cos(\phi_C + \psi_{CV}) + A_n \cos\phi_n} \right\}, \end{aligned} \quad (5.14)$$

at each angle frequency ω . The error between the identified phase difference and system phase shift is:

$$\begin{aligned} \Delta\phi_e(t) &= \Delta\phi_P(t) - \psi_{PV}(t) \\ &= \tan^{-1} \left\{ \frac{A_C |H_{CV}| \sin(\phi_C + \psi_{CV} - \psi_{PV}) +}{A_C |H_{CV}| \cos(\phi_C + \psi_{CV} - \psi_{PV}) +} \right. \\ &\quad \left. \frac{A_n \sin(\phi_n - \psi_{PV})}{A_P |H_{PV}| + A_n \cos(\phi_n - \psi_{PV})} \right\} \end{aligned} \quad (5.15)$$

The above equation illustrates that, as well as the P_{ETCO_2} term, any noise term will also distort the result of phase difference identification. However, if H_{PV} and H_{CV} are known or can be estimated, the error caused by P_{ETCO_2} fluctuations can be corrected. The corrected phase difference is:

$$\begin{aligned} \Delta\phi_P^c &= \Delta\phi_P - \\ &\tan^{-1} \left\{ \frac{A_C |H_{CV}| \sin(\phi_C + \psi_{CV} - \psi_{PV})}{A_P |H_{PV}| + A_P |H_{CV}| \cos(\phi_C + \psi_{CV} - \psi_{PV})} \right\} \end{aligned} \quad (5.16)$$

where $\Delta\phi_P^c$ is the estimate for ψ_{PV} at each angle frequency ω . Continuous complex Morlet wavelet transforms are also used to estimate instantaneous amplitude and phase of each

signal, i.e. $|W_P|(a, t)$ and $|W_C|(a, t)$ replace $A_P(\omega, t)$ and $A_C(\omega, t)$ respectively; $\psi_{PV}(a, t)$ and $\psi_{CV}(a, t)$ replace $\psi_{PV}(\omega, t)$ and $\psi_{CV}(\omega, t)$, thus the correction term can be written as:

$$\Delta\phi_P^c(a, t) = \Delta\phi_P - \tan^{-1} \left\{ \frac{|W_C H_{CV}| \sin(\phi_C + \psi_{CV} - \psi_{PV})}{|W_P H_{PV}| + |W_C H_{CV}| \cos(\phi_C + \psi_{CV} - \psi_{PV})} \right\}, \quad (5.17)$$

as a function of wavelet scale a and time t . Its circular mean, $\Delta\bar{\phi}_P^c$, and the corresponding synchronization index, γ_P^c , are also calculated as:

$$\Delta\bar{\phi}_P^c(a) = \tan^{-1} \left\{ \frac{\sum_t \sin(\Delta\phi_P^c(a, t))}{\sum_t \cos(\Delta\phi_P^c(a, t))} \right\}, \quad (5.18)$$

$$\gamma_P^c(a) = \frac{1}{N} ([\sum_t \cos(\Delta\phi_P^c(a, t))]^2 + [\sum_t \sin(\Delta\phi_P^c(a, t))]^2). \quad (5.19)$$

The corrected phase difference is a better estimation of the $ABP - CBFV$ system phase shift. This will now be demonstrated using a physiologically-based linear model and an example physiological data set.

5.2.5 Data collection and processing

Synthetic Data

Synthetic data is generated by a linear time-invariant model. The system comprises two transfer functions for $ABP - CBFV$ and $P_{ETCO_2} - CBFV$, which are linear approximations of the physiologically-based model described in Payne (2006). The linearisation procedure can be found in Chapter 4 and Payne and Tarassenko (2006). Measured ABP and P_{ETCO_2} of a single subject were used as model inputs. The wavelet phase synchronization method is used to identify the phase difference between one model input, ABP , and model output, $CBFV$, with or without another model input, P_{ETCO_2} . The circular mean phase differences in both cases are then compared to the true phase shift of the $ABP - CBFV$ system and their difference calculated. Moreover, with the known $ABP - CBFV$ and $P_{ETCO_2} - CBFV$ transfer functions, Equation 5.17 is used to obtain the corrected phase difference, with the effect of CO_2 removed. The time-averaged value of corrected phase difference is then compared to the true $ABP - CBFV$ system phase shift, and its corresponding synchronization

index is also compared with the theoretical value, unity. This test on synthetic data is used to validate the modified phase synchronization method for multivariate system outlined above.

Physiological Data

Thirteen healthy subjects participated in the study. All subjects received verbal and written instructions outlining the experiment procedure; written informed content was obtained, studies conformed to the standards set by Declaration of Helsinki, and research study was approved by the Conjoint Health Research Ethics Board at the University of Calgary (Grant ID 15671). Participants were not taking any medication, all were non-smokers, and none had any history of cardiovascular, cerebrovascular, or respiratory disease. The experimental data were collected under supine, free-breathing conditions (Mitsis et al. (2004a), Chapter 4). The experimental variables P_{ETCO_2} were monitored using a mass spectrometer (AMIS2000, Innovision, Odense, Denmark) and were sampled every 20ms. ABP was monitored continuously in the finger by photoplethysmography (Portapress, TPD Biomedical Instrumentation, the Netherlands). $CBFV$ was measured with a 2-MHz Doppler ultrasound system (TC22, SciMed, Bristol, U.K.) in the right middle cerebral artery. Both the pressure and velocity signals were sampled every 10 ms.

The time series of all experimental variables were further resampled to 1Hz using cubic spline interpolation. This frequency was chosen to be consistent with existing value widely used in the literature (Zhang et al. (1998a); Mitsis et al. (2004b,a)). The resampled data were then high pass filtered using a fifth-order Butterworth filter with a cut-off frequency of 0.005Hz to remove the very slow variation and baseline shift (Rowley et al. (2007); Mitsis et al. (2004b,a)). Sections of the time series having a duration of 2000 seconds were selected for spectral and transfer function analysis. Power spectral densities were calculated for each of the preprocessed time series with the Welch technique (Welch (1967)) with a 128-point (128 seconds) Hanning window with 50% overlap. Transfer functions for $ABP - CBFV$, H_{PV} , and for $P_{ETCO_2} - CBFV$, H_{CV} , were estimated through multivariate transfer function analysis (Chapter 4). Wavelet phase differences between ABP and $CBFV$ are

then identified using the wavelet phase synchronization method and estimated transfer functions were used to eliminate the effect of the other variable, P_{ETCO_2} . The identified phase difference, with and without correction terms, is compared to the estimated phase shift of H_{PV} using the multivariate system identification technique.

5.2.6 Statistics

The variability of the ABP , P_{ETCO_2} and $CBFV$ time series was assessed by calculating the coefficients of variation given by standard deviation divided by the mean for all values in each recording, as in Panerai et al. (2006). The differences between two synchronization indices of $ABP - CBFV$ relationship with and without CO_2 correction were tested for significance with the two-tailed Wilcoxon signed rank test (see Goulden (1959)). The percentage of positive instantaneous phase between ABP and $CBFV$ over all subjects was also obtained in both cases. Again, the two-tailed Wilcoxon signed rank test was used to test their difference.

5.3 Results

5.3.1 Synthetic data

Figure 5.1 shows the frequency responses of the $ABP - CBFV$ transfer function, H_{PV} , and the $P_{ETCO_2} - CBFV$ transfer function, H_{CV} , for the model (normalized response). The pressure autoregulation mechanisms were modelled as a high-pass filter transmitting rapid changes in ABP but blocking low-frequency variation. As shown in Figure 5.1(a), small gain was found at high scales (low frequencies) and large gain at low scales (high frequencies) with slight resonance around a scale of 3.5 ($0.3Hz$). The positive value of phase in the low frequency range indicates changes in velocity lead changes in pressure, which is due to the active resistance mechanism, as suggested in Panerai et al. (2006). However, in the high-frequency range, changes in velocity are almost in phase with changes in pressure. In contrast to pressure autoregulation, CO_2 reactivity was modelled as a low-

pass filter with high gains at high scales (low frequencies) and low gains at low scales (high frequencies). The negative value of phase at all scales indicates that P_{ETCO_2} leads $CBFV$ in all frequency range, which is in good agreement with experimental data (Poulin et al. (1996, 1998)).

Figure 5.1 Frequency response of the model. a) Gain and phase of $ABP - CBFV$ transfer function. b) Gain and phase of $P_{ETCO_2} - CBFV$ transfer function.

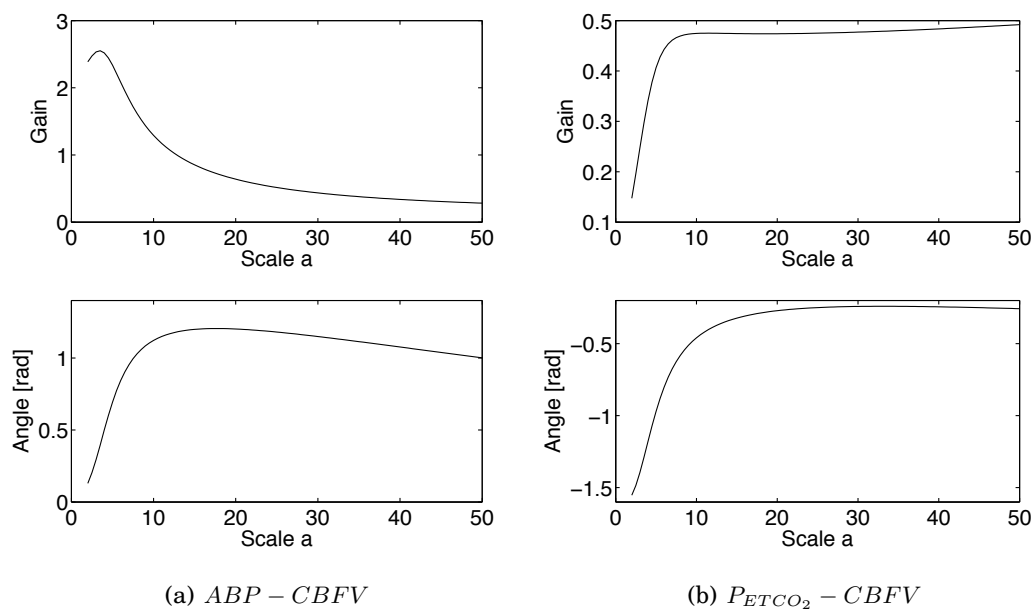
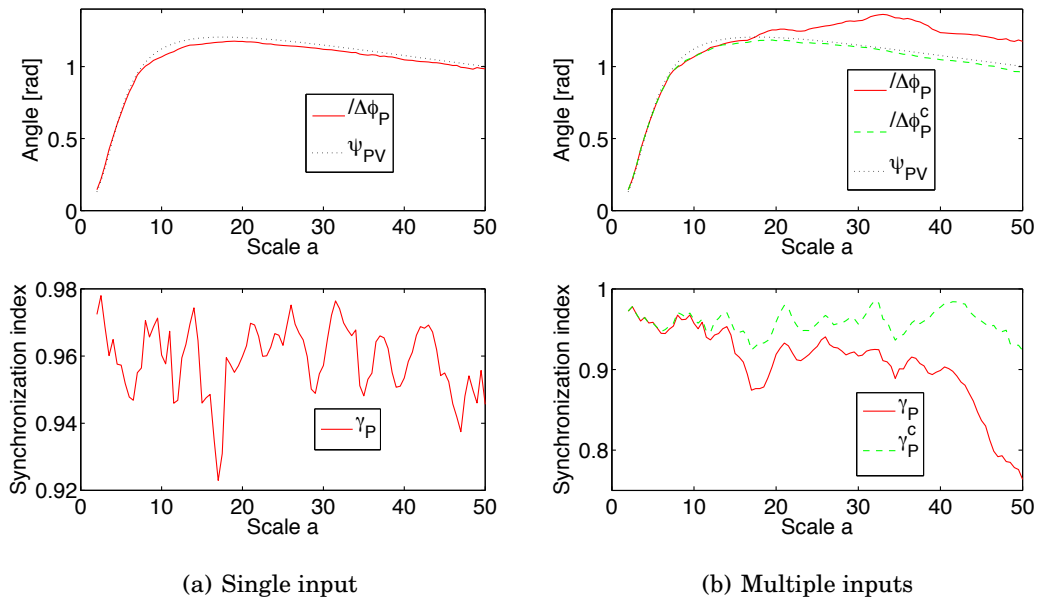


Figure 5.2 shows the phase synchronization result between the model input (measured ABP) and the model output (predicted $CBFV$). For the case of a single input, ABP , the circular mean phase difference, $\Delta\bar{\phi}_P$ is consistent with the actual system phase shift, ψ_{PV} , at all scales. The corresponding synchronization index is also close to unity. However, for the case of an extra input, CO_2 (measured P_{ETCO_2}), $\Delta\bar{\phi}_P$ no longer represents ϕ_{PV} in the low frequency region, where the corresponding synchronization index, γ_P , is low. The identification error can be corrected using Equation 5.17, the corrected value, $\Delta\bar{\phi}_P^c$, being very close to ψ_{PV} , the corresponding synchronization index, γ_P^c , returning to higher values close to unity.

The above result illustrates that, in the case of multiple inputs, the phase difference be-

Figure 5.2 Wavelet phase synchronization for linear time-invariant model input and output. a) Single input, *ABP*. Top: phase shift of *ABP* – *CBFV* transfer function, ψ_{PV} , over different scales (black dotted line); time-averaged phase difference between *ABP* and *CBFV*, $\Delta\bar{\phi}_P$ (red solid line). Bottom: synchronization index between *ABP* and *CBFV*, γ_P . b) Multiple inputs: *ABP* and P_{ETCO_2} . Top: phase shift of *ABP* – *CBFV* transfer function, ψ_{PV} , over different scales (black dotted line); time-averaged phase difference between *ABP* and *CBFV* without correction, $\Delta\bar{\phi}_P$ (red line); time-averaged phase difference with correction, $\Delta\bar{\phi}_P^c$ (green dashed line). Bottom: synchronization index between *ABP* and *CBFV* without correction, γ_P (red solid line); synchronization index with correction, γ_P^c (green dashed line).



tween one input, ABP , and the output, $CBFV$, will be distorted by an additional input, P_{ETCO_2} , and no longer accurately represent the true $ABP - CBFV$ system phase shift. However, with the correction term which eliminates the effect of other disturbing variables, the modified phase synchronization method can successfully estimate the real system phase shift. This method, which has been shown here to be valid in identifying the multivariate system, will now be applied to real physiological data to analyse the cerebral autoregulation system.

5.3.2 Physiological data

A total of 13 data files were available for analysis. Their baseline values and coefficients of variation for ABP , P_{ETCO_2} and $CBFV$ variables are given in Table 5.1.

Table 5.1 Baseline values and coefficients of variation for ABP , P_{ETCO_2} , P_{ETO_2} , and $CBFV$ for 13 subjects (values are Means \pm SD)

Variable	Baseline	variation
ABP	76.6 ± 7.0 [mmHg]	4.9 ± 1.2 [%]
P_{ETCO_2}	37.4 ± 1.8 [mmHg]	2.4 ± 0.7 [%]
$CBFV$	53.5 ± 5.2 [cm/s]	5.9 ± 1.3 [%]

$ABP - CBFV$ and $P_{ETCO_2} - CBFV$ transfer functions were identified from the experimental data by multivariate transfer function analysis (Section 5.2.2). Their frequency responses are shown in Figure 5.3. The estimated $ABP - CBFV$ transfer function behaves like a high-pass filter, with high gain at low scales: 2 – 10 (frequencies: $0.5 - 0.1Hz$) and low gain at high scales: 10 – 50 (frequencies: $0.1 - 0.02Hz$). Positive phase indicates that $CBFV$ leads ABP in the low frequency band, which is consistent with other studies (Panerai et al. (1999, 2001); Zhang et al. (1998a)). In contrast, the estimated $P_{ETCO_2} - CBFV$ transfer function behaves like a low-pass filter, with lower gains at low scales: 8 – 15 (frequencies: $0.07 - 1.25Hz$) and higher gains at high scales. Although the estimated gain seems to be quite large at scales 2 – 10, actually there is very little P_{ETCO_2} power at those frequencies, so the estimation is not robust in that frequency region. The corresponding multiple coherence is also shown in Figure 5.3(c), similarly to that shown in Chapter 4.

Figure 5.3 Frequency response of the identified system. a) Estimated transfer function gain and phase for $ABP - CBFV$ relationship. b) Estimated transfer function gain and phase of $P_{ETCO_2} - CBFV$ relationship. c) Multiple coherence of multivariate system. Solid line: mean value; dotted line: \pm standard deviation.

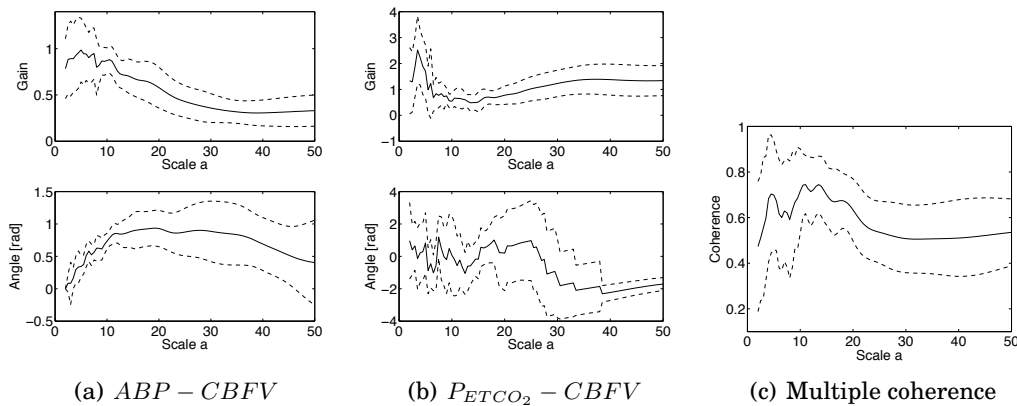
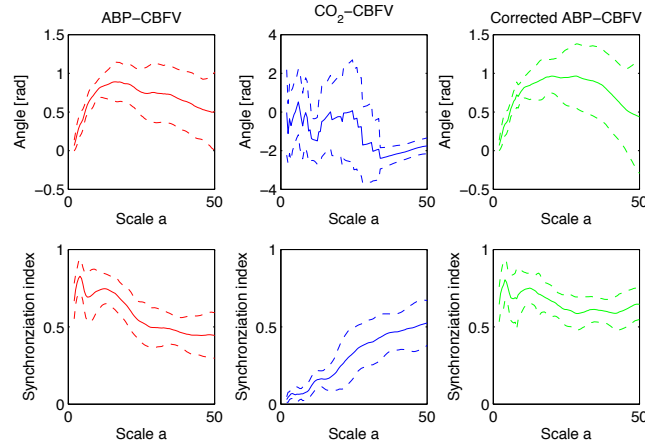


Figure 5.4 shows the identified mean phase difference of $ABP - CBFV$ and $P_{ETCO_2} - CBFV$ system, together with their corresponding synchronization indexes (group mean value \pm standard deviation). For the $ABP - CBFV$ system, high values of synchronization index were found at high frequencies, with two distinct peaks, a narrow one at $0.25Hz$ ($a = 4, \gamma = 0.83$) and another broad one at $0.08Hz$ ($a = 12, \gamma = 0.75$). In contrast, much lower index values were found at lower frequencies (higher scales: $a > 30, \gamma < 0.5$). This result is generally consistent with the findings of Latka et al. (2005), with slight differently peak frequencies. For the $P_{ETCO_2} - CBFV$ system, the inverse trend was found with an enhanced value of synchronization index at increased scales, which illustrates that P_{ETCO_2} fluctuations have a more significant contribution to low frequency $CBFV$ variability.

The estimated $ABP - CBFV$ and $P_{ETCO_2} - CBFV$ transfer functions using multivariate transfer function analysis are used to correct the effect of the additional variable, P_{ETCO_2} , and to estimate the real phase shift of $ABP - CBFV$ system. The corrected mean phase difference and synchronization index are also shown in Figure 5.4. The density map (Figure 5.5(a)) represents the time evolution of the normalized phase difference without CO_2 correction, $\Delta\phi_P/2\pi$ (top), and with CO_2 correction, $\Delta\phi_P^c/2\pi$ (bottom) for 50 integer values of the wavelet scale a for a typical subject. In particular, Figure 5.5(b) displays the variation

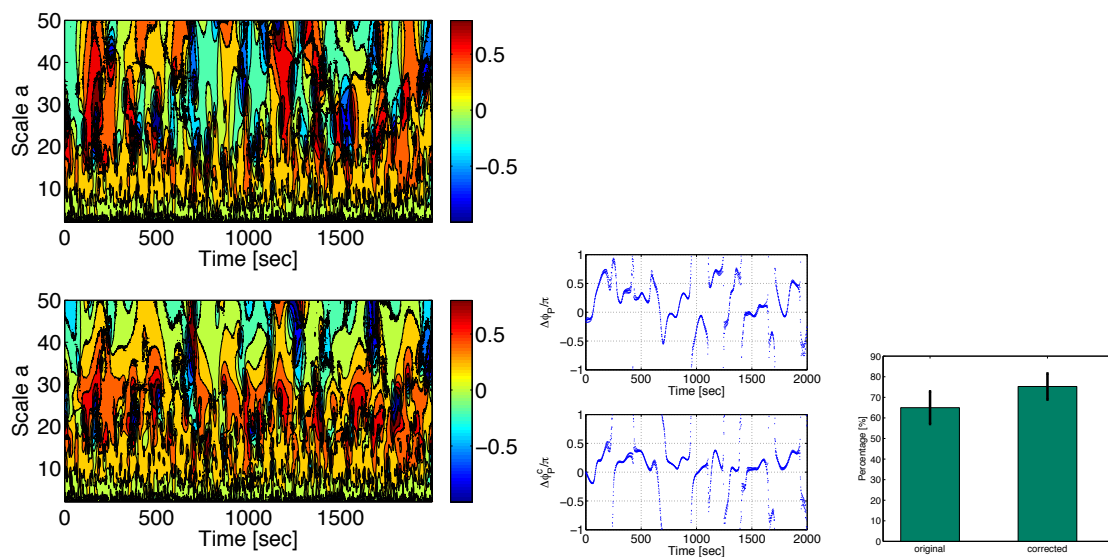
of the phase difference for the scale $a = 40$ ($f_a = 0.025Hz$). In the low frequency part of the spectrum, the phase difference slowly evolves over time with broad distribution, with both phase leading ($0 - \pi$) and phase lagging ($-\pi - 0$) between *CBFV* and *ABP*. However, with the correction term, which removes the effects of CO_2 , the instantaneous phase difference becomes more positive, as shown in Figure 5.5(c) ($P < 0.002$).

Figure 5.4 Phase difference and synchronization index for real system (mean value \pm standard deviation). Top: time-averaged phase difference between *ABP* and *CBFV* time series, $\Delta\bar{\phi}_P$, P_{ETCO_2} and *CBFV*, $\Delta\phi_C$, and corrected time-averaged phase difference between *ABP* and *CBFV*, $\Delta\bar{\phi}_P^c$. Bottom: the corresponding synchronization indices, γ_P , γ_C and γ_P^c respectively.



The last figure (Figure 5.6) shows the group-averaged circular mean phase and synchronization index. In the low frequency band, i.e. $< 0.05Hz$ ($a > 20$), the value of the corrected synchronization index is significantly higher than the original index ($P < 0.005$) while no obvious difference exists between them at higher frequencies. The slightly lower value of corrected synchronization index in the high frequency range is because the estimated transfer functions are not accurate in the frequency band where there is inadequate input power. This issue will be revisited in Section 5.4. The result indicates that the lack of synchronization between *ABP* and *CBFV* at low frequencies is partly due to the effect of CO_2 , and with the correction term which eliminates its influence, the entrainment of *ABP* and *CBFV* is found to be stronger. This also illustrates that the effects of CO_2 are found mainly at low frequencies, which is consistent with the results of Mitsis et al. (2004b) and

Figure 5.5 Instantaneous phase difference. a) Density map of the normalised instantaneous phase difference over time, $\Delta\phi_P/2\pi$ (top), and with CO_2 correction, $\Delta\phi_P^c/2\pi$ (bottom) for a typical subject. b) Plot of normalized phase difference for scale $a = 40$. c) Histogram showing percentage of positive instantaneous phase over time with and without CO_2 correction (group mean value \pm standard deviation).

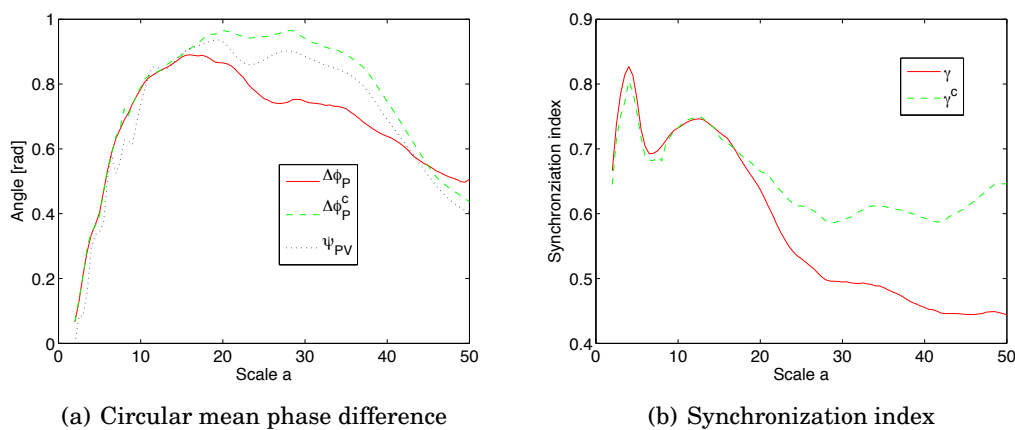


(a) Density map of normalised phase difference (b) Instantaneous phase difference at scale $a = 40$ (c) Percentage of positive phase at scale $a = 40$

Chapter 4.

In the low frequency region where the synchronization index is low, the identified phase difference is also different from the estimated system shift ($\Delta\bar{\phi}_P$ and ψ_{PV}), although not significantly so. With the correction term, the two are in better qualitative agreement ($\Delta\bar{\phi}_P^c$ and ψ_{PV}), as would be expected. The increased value of the corresponding synchronization index indicates that there is a phase difference with less variation over time. Thus, with a smaller standard deviation, the circular mean phase difference provides a better estimate of the real system phase shift.

Figure 5.6 a) Comparison of mean phase difference between *ABP* and *CBFV* without CO_2 correction, $\Delta\bar{\phi}_P$, with CO_2 correction, $\Delta\bar{\phi}_P^c$, and phase shift of estimated *ABP* – *CBFV* transfer function using multivariate transfer function analysis, ψ_{PV} , is also provided for comparison. b) Synchronization index without CO_2 correction, γ_P , with CO_2 correction, γ_P^c .



5.4 Discussion

In the high frequency band, the synchronization curve exhibits high values with two distinct peaks, the first at a scale corresponding to $0.25Hz$, the second at a frequency of around $0.08Hz$, being slightly different from the result of Latka et al. (2005), which are $0.33Hz$ and $0.1Hz$ respectively. Latka et al. (Latka et al. (2005)) suggested that the higher frequency peak originated to respiration. Normal respiratory rates reported from healthy adults varies from source to source: between 12 to 20 breaths per minute (Schimelpfenig

and Lindsey (2000)). Since both $0.25Hz$ and $0.33Hz$ (15 and 20 breaths per minute) are in the normal range, their difference may be just due to different subject groups. The low frequency peak could correspond to the Mayer Wave peak and it has been suggested that the peak frequency will shift to lower frequencies during head-up tilt compared to supine (Rowley et al. (2007)).

In the low frequency region, the instantaneous phase difference between *ABP* and *CBFV* has an almost uniform distribution, reflected by a low value of synchronization index, which is consistent with the result of Latka et al. (2005). However, the lack of synchronization between *ABP* and *CBFV* at those frequencies does not necessarily lead to the conclusion that cerebral autoregulation system is nonstationary. Instead, our current study illustrates that the observed low synchronization index between *ABP* and *CBFV* can be attributed to unmeasured variability.

As is well known, *ABP* is not the only determinant of *CBFV* variability, other parameters such as CO_2 having a vasodilatory effect on cerebral vessels and thus influencing blood flow, known as CO_2 reactivity. A number of studies have investigated the dynamic characteristics of the $CO_2 - CBFV$ relationship through measuring both the *CBFV* response to a step change in end-tidal CO_2 (Poulin et al. (1996, 1998)) and the continuous recordings of breath-by-breath spontaneous fluctuations in CO_2 (Mitsis et al. (2004b); Panerai et al. (2000), Chapter 4). Mitsis et al. (Mitsis et al. (2004b)) found that the CO_2 term and the interaction term between *ABP* and CO_2 can contribute significantly to the observed *CBFV* variability in the low frequency band. Peng et al. (Chapter 4) further point out that the observed low values of univariate coherence at low frequencies is partly due to CO_2 variability not being considered, and the transfer function between *ABP* and *CBFV* at those frequencies can be modified by the fluctuation of other variables such as CO_2 , no longer representing pressure autoregulation. In a similar way, the phase relationship between *ABP* and *CBFV* in the low frequency band is also modified by CO_2 reactivity. An observed low value of synchronization index does not mean that the *ABP* and *CBFV* are not physiologically related, but that their phase relationship in that frequency region has

been distorted by another parameter, CO_2 . In fact, we have proposed a modified phase synchronization method to correct this phase distortion and thus to estimate the true phase shift of $ABP - CBFV$ system. With the correction term which eliminates the effect of CO_2 , the synchronization index is significantly increased in the low frequency band, suggesting a underlying relationship between ABP and $CBFV$ even at low frequencies.

The phase shift between ABP and $CBFV$ is an important parameter in the assessment of cerebral autoregulation status. Previous studies (Diehl et al. (1995); Birch et al. (1995)) have studied the $CBFV$ response to slow oscillations in ABP by adopting slow breathing and periodic squatting/standing up cycles respectively. Both of these studies showed a phase lead of $CBFV$ to ABP in individuals at low frequencies and the phase difference were found to be highly correlated to $PaCO_2$ level: a phase difference increase was found with hypocapnia while a decrease with hypercapnia (Birch et al. (1995)), suggesting differing autoregulation status. Moreover, a recent paper (Liu et al. (2003)) used an ARX model to analyse the phase difference between $CBFV$ and ABP spontaneous fluctuations during thigh cuff test and lower body negative pressure test. A consistent positive phase shift was found for all data sets and again, the phase lead was also found to decrease in the hypercapnia condition. Besides time-averaged phase relationship assessed by Fourier analysis, instantaneous phase difference can now be extracted by a phase dynamics method, based on wavelet analysis, which sheds new light on the nature of cerebral hemodynamics (Latka et al. (2005)). Though the circular mean phase difference is shown to be positive here, which is consistent with former studies, the instantaneous phase difference slowly evolves over time and tends to have a uniform distribution, with both positive and negative values (*Figure 5.5(b)*). Latka et al. (2005) suggested that the zero or negative phase difference for a short time can be due to intermittent autoregulatory failure even in normal subjects. However, with the CO_2 correction term, the instantaneous phase shift (*Figure 5.5(c)*) shows a more positive value over time, which illustrates the previous periodical zero and negative phase can be partly attributed to the effect of CO_2 .

Multivariate transfer function analysis was used in the present study to estimate the CO_2

correction term. Compared to univariate transfer function analysis, it has been shown to be more valid in analysing the dynamics of cerebral autoregulation in the low frequency band, as suggested by the significantly increased value for multiple coherence at those frequencies (Chapter 4). The same data-set used here and in Chapter 4 is from normal subjects, the stationary assumption is acceptable. However, under certain physiological conditions, such as exercise or tilting, the measurements are expected to be highly nonstationary which will invalidate the necessary assumption for time-invariant transfer function analysis. Moreover, for very high frequencies where there is little ABP and CO_2 power, the transfer function analysis is not very robust. Thus more robust techniques such as time-varying transfer function analysis (Zhao et al. (2005)) and wavelet cross-correlation analysis (Rowley et al. (2007); Mizuno-Matsumoto et al. (2005)) will need to replace current techniques to get a better estimation of the dynamics of the cerebral autoregulation system. This will be the subject of future work.

5.5 Conclusion

In this paper, we demonstrate that the fluctuations in CO_2 distort the phase relationship between ABP and $CBFV$ in the low frequency region, corresponding to a low value of synchronization index between the two variables. A modified phase synchronization method has been proposed to eliminate the effect of CO_2 and to estimate the true phase shift of $ABP - CBFV$ system. This new method has been applied to both synthetic data and physiological data and has been proved successful, resulting in a significantly increased value of synchronization index between ABP and $CBFV$ at low frequencies.

The effects of age on the spontaneous low-frequency oscillations in cerebral and systemic cardiovascular dynamics

Although the effects of ageing on cardiovascular control and particularly the response to orthostatic stress have been the subject of many studies, the interaction between the cardiovascular and cerebral regulation mechanisms is still not fully understood. Wavelet cross-correlation is used here to assess the coupling and synchronization between low-frequency oscillations (LFOs) observed in cerebral hemodynamics, as measured using cerebral blood flow velocity (CBFV) and cerebral oxygenation (O_2Hb), and systemic cardiovascular dynamics, as measured using heart rate (HR) and arterial blood pressure (ABP), in both old and young healthy subjects undergoing head-up tilt table testing. Statistically significant increases in correlation values are found in the interaction of cerebral and cardiovascular LFOs for young subjects ($P < 0.01$ for HRABP, $P < 0.001$ for HRO_2Hb and $ABPO_2Hb$), but not in old subjects under orthostatic stress. The coupling between the cerebrovascular and wider cardiovascular systems in response to orthostatic stress thus appears to be impaired with ageing¹.

¹This study has been published as Peng et al. (2008a)

6.1 Introduction

Any postural change induces a transient change in mean arterial blood pressure (ABP) which is detected by the baroreceptors and then minimised by the cardiovascular autonomic regulation mechanisms (Priebe (1999)). Changes in ABP are further compensated by the protective mechanism of the brain, cerebral autoregulation, which maintains a relatively constant cerebral blood flow (CBF) despite variations in pressure (Panerai (1998)). These two mechanisms collectively ensure adequate CBF in the brain during postural changes. However, both the cardiovascular response and the cerebral autoregulation can become impaired with ageing, possibly resulting in orthostatic hypotension and related cerebral symptoms, such as light-headedness, dizziness, falls, or even syncope in old people (Jansen et al. (1989); Lipsitz (1989); Raiha et al. (1995)). These symptoms can occur when cerebral perfusion and hence oxygen supply become compromised as a result of reduced cerebral blood flow in response to postural change, which indicates either impaired cerebral autoregulation or impaired cardiovascular regulation with ageing (Laitinen et al. (2004); Mehagnoul-Schipper et al. (2000, 2001)), or possibly both.

Numerous previous studies have attempted to quantify the effects of posture changes on both cerebral and cardiovascular hemodynamics by measuring absolute changes in heart rate (HR), ABP, CBF and frontal cerebral oxygen hemoglobin concentration (O_2Hb , measured by near-infrared spectroscopy) (Smith et al. (1987); Laitinen et al. (2004); Levine et al. (1994); Lagi et al. (1994)). However, the noise that is inherent in the data means that many repetitions are required for a single patient, which is problematic in the case of patients with an impaired autonomic nervous system (Panerai (1998)). Other studies have thus investigated the posture dependence of spontaneous oscillations in cardiovascular and cerebrovascular variables and found that the oscillatory changes in ABP and O_2Hb increased significantly from the supine to the upright position (Tachtsidis et al. (2004)).

Spontaneous low-frequency oscillations (LFOs) at frequencies around 0.1 Hz in cerebral hemodynamics have been observed under a wide range of experimental conditions. They

can be distinguished by spectral analysis from other fluctuation components, such as very low-frequency oscillation (VLFs) centered at 0.02 Hz and high-frequency oscillations (including the cardiac cycle at approximately 1 Hz and the respiratory cycle at approximately 0.2-0.3 Hz). Although the origin of LFOs is still unclear, these oscillations have been found to be modulated by pharmacological and pathological conditions, or by neural activation (Obrig et al. (2000)). Within the same frequency band, high variability in ABP and HR is also found. These oscillations, called "Mayer waves" (Mayer (1876)), originate from the action of the baroreflex in the systemic regulation of the cardiovascular system, and can be ascribed to sympathetic nervous activity (Nilsson and Aalkjaer (2003)). Since the cerebrovascular system is a part of the systemic circulation, it is mediated by both central sympathetic activation and local myogenic or metabolic mechanisms (Priebe, 2000). It is thus very unlikely that LFOs found in cerebral hemodynamic variables are completely independent of their cardiovascular counterparts. Indeed, it has been shown that one third of cerebrovascular oscillations in the range of 0.04-0.15 Hz can be tracked back to the systemic cardiovascular fluctuations (HR and ABP) in the same frequency band (Katura et al., 2006). Fluctuations in HR (<0.1 Hz) have also recently been identified as an important source of variance in the resting-state fMRI BOLD signal (Shmueli et al. (2007)).

The bivariate relationship between LFOs in ABP and cerebral blood flow velocity (CBFV), measured using transcranial Doppler ultrasound (TCD), can be used as an assessment of cerebral autoregulation status (Zhang et al. (1998a,b); Panerai et al. (2001, 1999)). Within this framework, cerebral autoregulation is considered to be a high-pass filter, with ABP as the input and CBFV as the output, whose parameters (gain and phase) can be identified from experimental data using a system identification technique which essentially involves division of the power spectra of the two time series. However, this Fourier spectral analysis makes the assumption of stationarity, which might not be valid for clinical measurements of older individuals or patients with an impaired sympathetic regulation system. It also requires a relatively long recording time as its accuracy is dependent on the amount of spontaneous power in the low frequency range (Panerai et al., 1998; Zhang et al., 1998b).

Wavelet analysis thus provides an alternative framework, which allows for the identification of time-varying frequency and phase and for the characterization of the nonstationary effects of cerebral dynamics, thus overcoming the restriction of earlier methods (Latka et al. (2005); Rowley et al. (2007)). Wavelet cross-correlation, in particular, has been shown to be more effective than transfer function estimation techniques when used with time series that are obtained from a short duration head-up tilt table test (Rowley et al. (2007)), as it is a measure of the level of similarity of two signals and does not depend on the power of those signals.

The aim of the present study was thus to investigate the effects of ageing on both the cerebrovascular hemodynamic and systemic cardiovascular responses to posture changes using wavelet cross-correlation. O_2Hb was chosen in addition to CBFV to represent cerebrovascular hemodynamics as it provides a direct measurement of changes in cerebral oxygenation at the cerebral cortical tissue level (Schroeter et al., 2004) and its LFOs have been found to be more pronounced than other variables measured by near-infrared spectroscopy (NIRS) (Obrig et al. (2000)).

6.2 Methods

6.2.1 Subjects

A total of 33 healthy subjects were studied: 18 young and 15 old. Participants were included if they were normotensive ($< 140/90mmHg$), non-smokers, and free of overt chronic diseases, as assessed by detailed medical history, physical examination and 12-lead ECG. None of the participants were taking any medication or had any history of syncope. The study was approved by the Local Ethical Committee, and written informed consent was obtained.

6.2.2 Experimental design

Subjects were instructed to abstain from exercise, alcohol and caffeine 12h prior, and not to eat a heavy meal within 4 hours prior to experimental testing. Subjects attended the laboratory on two occasions. The first occasion was used to familiarize the subjects with the tilt table and related experimental apparatus. During the second visit, the main experimental testing was conducted.

6.2.3 Measurements of CBF velocity, cerebral oxygenation, arterial blood pressure and end-tidal gases

During each session CBF velocity, cerebral oxygenation, ABP, end-tidal carbon dioxide (PETCO₂) and oxygen (PETO₂) partial pressures and electrocardiography (ECG) were recorded continuously. Blood flow velocity in the right middle cerebral artery (MCA_v) was measured using a 2 MHz pulsed Doppler ultrasound system (DWL Doppler, Sterling VA, USA). Cerebral oxygenation was measured using a commercially available near infrared spectroscopy (NIRS) system (NIRO-200; Hamamatsu Photonics KK; Hamamatsu, Japan). A probe holder containing an emission probe and detection probe was attached at the right side of the forehead with a distance of 5 cm between the probes as previously described (Nollert et al. (1995)). Beat-to-beat BP was measured by finger photoplethysmography that uses a height correction system (Finometer, TPD Biomedical Instruments, Netherlands). Any changes in vertical displacement of the finger cuff relative to the heart are corrected for by a reference probe placed on the chest at heart level. Participants breathed through a respiratory mask (Hans-Rudolph 8980, Kansas City, MO) attached to a one-way non-rebreathing valve (Hans-Rudolph 2700). PETCO₂ and PETO₂ were sampled continuously and measured using a gas analyser (model CD-3A, AEI Technologies, Pittsburgh, PA). HR was also recorded using 3-lead electrocardiogram via a Bio Amp (Model ML132, ADInstruments, Colorado Springs, CO, USA). All data were sampled continuously at 200 Hz using an analog-digital converter (Powerlab/16SP ML795; ADInstruments) interfaced with a computer and displayed in real time during testing. Following supine rest for at

least 15 minutes, subjects were then tilted to 60° for fifteen minutes.

6.2.4 Maximal overlap discrete wavelet packet decomposition

The recently developed maximal overlap discrete wavelet packet transform using Hilbert wavelet pair filters (MODHWPT) (Selesnick, 2002; Selesnick et al., 2005; Whitcher et al., 2005; Whitcher and Craigmille, 2004) was used to decompose all the time series into sets of wavelet coefficients at different levels, associated with different frequency bands, as shown in Figure 6.1. For a time series $X = (X_0, X_1, \dots, X_{N-1})$, the j th level MODHWPT coefficients, $W_{j,n,t}^X$, can be calculated by a recursive scheme for which we assume that we already have the level $j - 1$ coefficients (Percival and Walden (2000)):

$$W_{j-1,n,t}^X = \sum_{l=0}^{L-1} \tilde{u}_{n,l} W_{j-1, [\frac{n}{2}], t-2^{j-1}l \bmod N}^X, \quad \begin{matrix} t = 0, 1, \dots, N-1 \\ n = 0, 1, \dots, 2^j - 1 \end{matrix} \quad (6.1)$$

The recursion starts with $W_{0,0,t}^X = X_t$. The wavelet packet filter $\tilde{u}_{n,l}$ is then defined as:

$$\tilde{u}_{n,l} = \begin{cases} \tilde{g}_l, & \text{if } n \bmod 4 \text{ is } 0 \text{ or } 3; \\ \tilde{h}_l, & \text{if } n \bmod 4 \text{ is } 1 \text{ or } 2; \end{cases} \quad (6.2)$$

where \tilde{h}_l and \tilde{g}_l are the unit scale analytic wavelet (high-pass) filter and scaling (low-pass) filter with discrete transfer function $\tilde{G}(k/N)$ and $\tilde{H}(k/N)$ respectively (Percival and Walden, 2006). They are designed to be approximate Hilbert transforms of each other, like sine and cosine waves, but with compact support (Whitcher et al., 2005; Whitcher and Craigmille, 2004). The coefficients from one filter of the pair form the real part of the transform and the coefficients from the other filter form the imaginary part (Whitcher and Craigmille, 2004). Due to the approximate Hilbert relationship at each node between the real and imaginary components of the MODHWPT coefficients, $W_{j,n,t}^X$ is a complex number approximately encoding the magnitude and phase of the signal at that frequency.

It is not possible to design a pair of wavelet filters that are exact Hilbert transforms; however approximate Hilbert wavelet pairs can be designed via spectral factorization. The detailed procedure of designing filter coefficients was outlined elsewhere (Selesnick (2002)). In practice, Equation 6.1 be replaced by filtering the level $(j - 1)$ coefficients with the circular filter having discrete transfer function $\tilde{G}(2^{j-1}k/N)$ and $\tilde{H}(2^{j-1}k/N)$. These filters

can be obtained by inserting $2^{j-1} - 1$ zeros between the elements of \tilde{g}_l and \tilde{h}_l (Olhede and Walden (2004)).

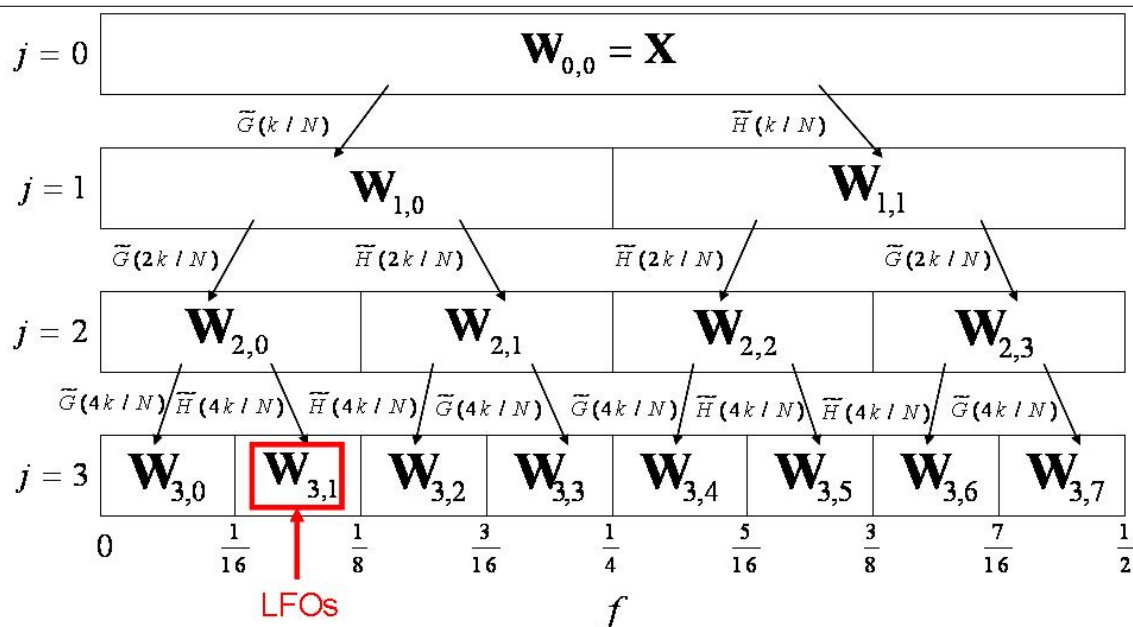
Since all the signals are sampled at 1 Hz in the preprocessing step, the frequency content of the MODHWPT coefficient time series $W_{j,n}^X$ are localized in a frequency band:

$$\lambda_{j,n} = [(-\frac{n+1}{2^{j+1}}, -\frac{n}{2^{j+1}}) \cup (\frac{n}{2^{j+1}}, \frac{n+1}{2^{j+1}})], \quad (6.3)$$

in which $W_{3,1}^X$, in particular, is associated with frequency interval [0.0625-0.125]Hz, the specific frequency intervals of our interest, LFOs. $W_{3,1}^X$ is a complex number encoding the magnitude and phase of the signal in that frequency band.

The raw MODHWPT coefficients can not be related to the original time series directly, as a circular time shift needs to be applied on the coefficients. By using a ‘center of energy’ strategy (Whitcher and Craigmille (2004); Percival and Walden (2000)), the time shifts of Hilbert wavelet filters can be obtained and the shifted MODHWPT coefficients can now be associated with the same times as the original time series.

Figure 6.1 MODHWPT tree



6.2.5 Discrete wavelet cross-correlation

Similar to the definition of continuous wavelet cross-correlation (Grinsted et al. (2004); Rowley et al. (2007)), the normalized discrete wavelet cross-correlation is defined as:

$$WCC_{j,n} = \frac{|R_{X,Y}(W_{j,n}^X, W_{j,n}^Y, \tau)|}{\sqrt{|R_{X,X}(W_{j,n}^X, 0) \bullet R_{Y,Y}(W_{j,n}^Y, 0)|}}, \quad (6.4)$$

in which $R_{X,Y}(W_{j,n}^X, W_{j,n}^Y, \tau)$ denotes the cross-correlation of the MODHWPT coefficients of two time series X and Y ($W_{j,n}^X$ and $W_{j,n}^Y$ respectively) for a relative time shift τ ; $R_{X,X}(W_{j,n}^X, 0)$ thus denotes the auto-correlation of the time series X for zero time shift.

$WCC_{j,n}$ represents the cross-spectral power in the two time series (shifted relative to each other by τ) as a fraction of the total power in the two time series. $WCC_{j,n} = 1$ would indicate that the coefficients of the two wavelet transforms were related to each other by a simple scaling factor, suggesting very strong synchronization in that frequency band.

In contrast to the continuous wavelet transform used by Grinsted et al. (2004) and Rowley et al. (2007), the maximal overlap discrete wavelet packet transform (MODWPT) is adopted here to decompose the original signals into wavelet coefficients of a series of frequency bands rather than a single frequency. Thus, the discrete wavelet correlation is not only much faster than the continuous equivalent, thus allowing for instantaneous analysis, but it is also ideal for assessing the coupling and synchronization between oscillations found in different variables in different frequency bands.

6.2.6 Statistical analysis

The characteristics of the different subject groups were compared by the student t-test (Rice (1995)). The baseline values were defined as the 3 minute averaged values in the supine position. The paired t-test was applied to examine the mean changes in HR, ABP, CBFV and O_2Hb for all subjects after tilt, which were calculated for a 10 minute average in the prolonged head-up position compared to the baseline value. The measurements in the

first two minutes after posture change were excluded in the averaging process to allow all the variables to reach a stable level. The age dependence of average postural changes was examined by the two-way repeated measures ANOVA test. Similarly, the maximum value of wavelet cross-correlation of LFOs and low frequency power spectra were also tested for posture effects using paired t-test and their age dependence was further examined by two-way repeated measures ANOVA.

6.3 Results

6.3.1 Subject characteristics

The characteristics of the 15 healthy elderly subjects and the 18 healthy young subjects are shown in Table 6.1, represented by grouped-averaged baseline values and inter-subject standard deviation. Older subjects had lower HR (12%) and CBFV (32%) in the resting state than young subjects.

Table 6.1 Subject characteristics (expressed as mean \pm SD)

	Elderly subjects	Young subjects	P between Groups
Age, y	65 \pm 5	27 \pm 4	P<0.001
HR, b min-1	58 \pm 7	66 \pm 9	P<0.01
ABP, mm Hg	89 \pm 10	83 \pm 7	0.0542
CBFV, cm s-1	48 \pm 10	70 \pm 7	P<0.001

6.3.2 Postural changes in cerebral and systemic cardiovascular dynamics

Table 6.2 shows the postural changes in HR, ABP, CBFV and O_2Hb in both the healthy old and young subject groups. In response to orthostatic stress induced by head-up tilt, all subjects showed an increase in HR ($P<0.001$) and a decrease in both CBFV ($P<0.001$) and O_2Hb ($P<0.001$ for older and $P<0.01$ for young subjects). However, the change of HR for older subjects was considerably smaller than in young subjects ($P<0.001$), which is consistent with previous findings (Kawaguchi et al. (2001); Laitinen et al. (2004)). No marked difference was found in other variables between groups.

Table 6.2 Postural changes in cerebral and systemic cardiovascular dynamics in the head-up positions versus supine positions (expressed as mean \pm SD); *P<0.01, **P<0.001, indicates the variables in which statistically significant postural changes were found.)

	Elderly subjects	Young subjects	P between Groups
HR, b min-1	8.1 \pm 4.1**	18.4 \pm 8.2**	P<0.001
ABP, mm Hg	-4.0 \pm 8.28	-2.9 \pm 4.4	0.6208
CBFV, cm s-1	-9.5 \pm 5.7**	-12.2 \pm 5.7**	0.1825
O_2Hb , μ molar	-3.4 \pm 2.9**	-3.1 \pm 3.5*	0.8086

6.3.3 Wavelet cross-correlation

Figure 6.2 shows an example of the MODHWPT decomposition (levels $j \leq 3$), applied to the heart rate time series for a typical subject. The zero level MODHWPT coefficients $W_{0,0}$ shown at the top are simply the original time series X . Other MODHWPT coefficient vectors $W_{3,0}$, $W_{3,1}$, $W_{2,1}$, $W_{1,1}$ are also displayed, corresponding to time-varying decompositions in the frequency intervals [0-0.0625] Hz, [0.0625-0.125] Hz, [0.125-0.25] Hz and [0.25-0.5] Hz, respectively. Since the frequency interval [0.0625-0.125] Hz is associated with low frequency oscillations, the dynamic relationship between the values of $W_{3,1}$ for different time series was the major target of this study. The vertical lines shown in the figure indicate sharp changes in the original signal which can easily be traced across several frequency bands (since sharp changes contain information across a wide range of frequencies). This shows that the MODHWPT coefficients can be very well associated with the original time series after the circularly shifting correction applied here.

The group-averaged wavelet cross-correlation of low frequency oscillations, $WCC_{3,1}$, for each pair of HR, ABP, CBFV and O_2Hb time series over all subjects over a range of delay time is shown in Figure 3, with the maximum correlation marked. As the coefficient signals are restricted to the frequency band [0.065-0.125] Hz, a maximum time delay of ± 8 seconds was chosen for correlation, referred to the 16-second period of the lowest frequency oscillation components. The multiple peaks shown in the correlation function are a result of the signals being periodic in nature. Occasionally maximum correlation is found at different peaks for the two groups (Figure 6.3(a), HR- O_2Hb ; Figure 6.3(b), CBFV- O_2Hb). This is likely to be due to the effects of measurement noise.

Figure 6.2 MODHWPT decomposition of the heart rate time series. $W_{3,1}$ corresponds to LFOs.

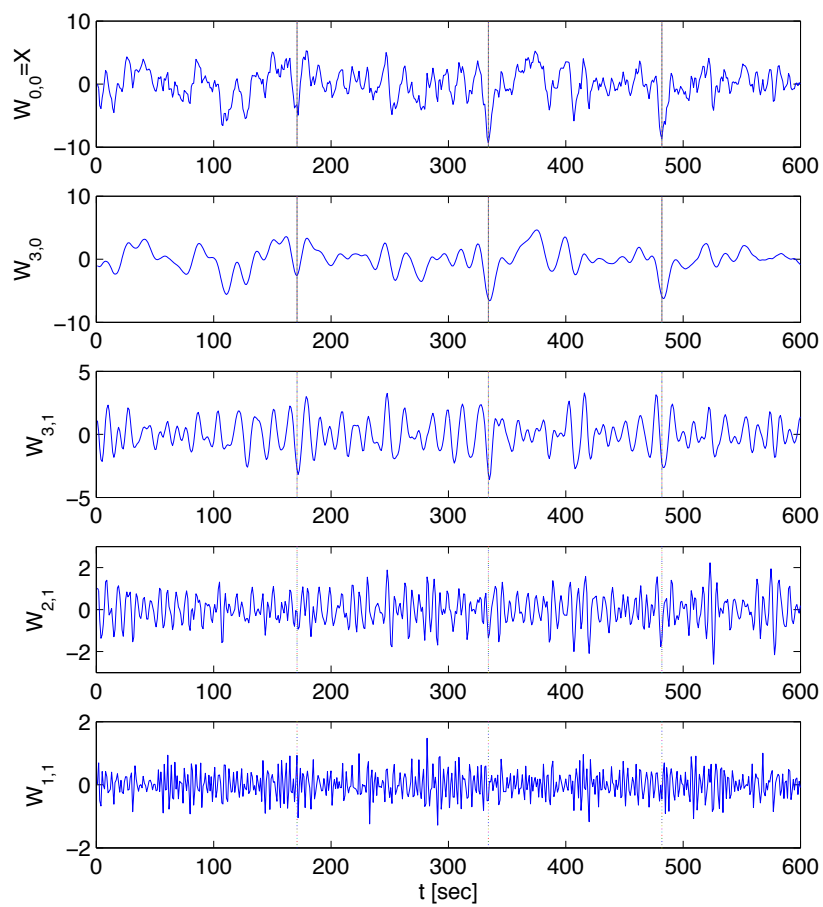
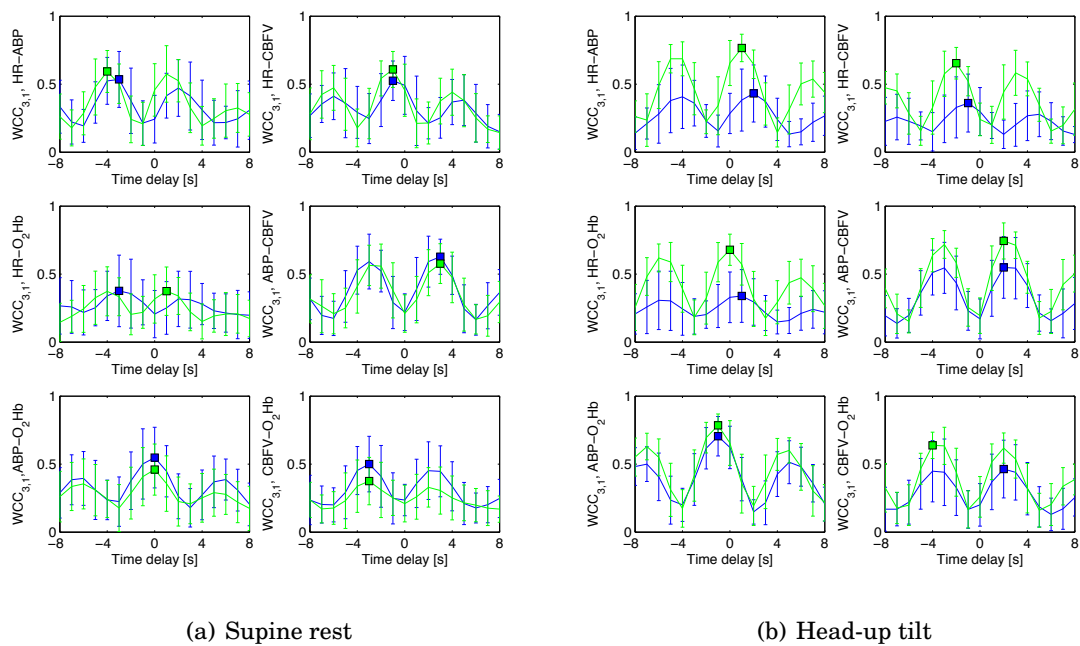
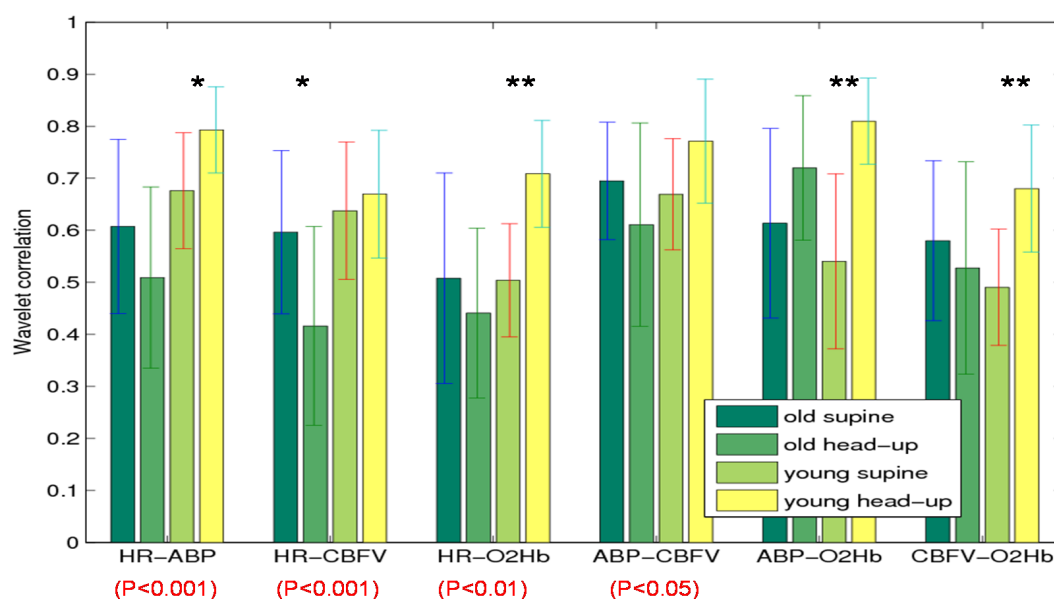


Figure 6.3 Group averaged wavelet cross-correlation of LFOs of each pair of HR, ABP, CBFV and O_2Hb for old (blue solid line) and young subjects (green dashed line) during supine rest and head-up tilt. Error bars represent standard deviation and spots indicate the maximum wavelet cross-correlations of each group.



In the supine position, there is no clear difference between old and young subjects, illustrated by the similar shapes of blue and green curves and their overlapping error bars (Figure 6.3(a)). In contrast, in the head-up position, mean wavelet correlation curves for the young subjects consistently have higher peak values than the corresponding values for elderly subjects, particularly for the paired time series of HR-ABP, HR-CBFV and HR- O_2Hb (Figure 6.3(b)). This difference is illustrated more clearly in Figure 6.4, which shows the value of the maximum wavelet cross-correlation for each paired time series in both the supine and head-up positions.

Figure 6.4 Maximum wavelet cross-correlation of LFOs for each pair of HR, ABP, CBFV and O_2Hb time series for both old and young subjects during supine rest and head-up tilt. * $P < 0.01$, ** $P < 0.001$, indicates the variables in which statistically significant postural changes were found. The age effect was also tested and statistically significant values are shown in red brackets. P-value refers to age*posture interaction effect tested by the two-way repeated measures ANOVA test.



The wavelet cross-correlation values in the head-up tilt position for all young subjects are greater than 0.5, which indicates strong linear interactions in the low frequency oscillations in all cardiovascular and cerebrovascular variables. The cardiovascular and cerebral hemodynamic regulation systems thus seem to be working to compensate for the effect of orthostatic stress. However, this is not the same for elderly subjects, in which the cor-

relations between cerebral (CBFV and O_2Hb) and systemic cardiovascular (HR and ABP) dynamics are found to be significantly lower ($P < 0.01$ for HR-CBFV and HR- O_2Hb , $P < 0.05$ for ABP-CBFV). This difference is only found in the head-up tilt period but not at supine rest, where the results for two groups are not significantly different.

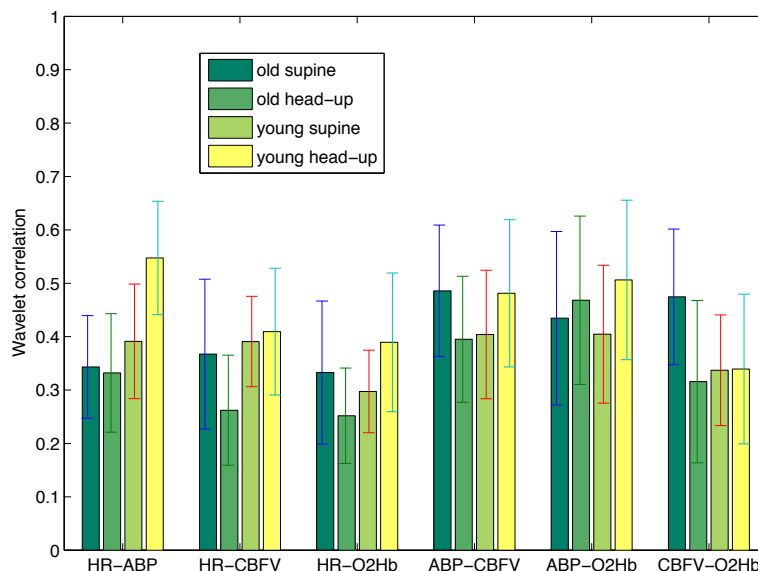
The two-way repeated measures ANOVA shows the effects of posture illustrates that the response to orthostatic stress is different for old and young subjects: young subjects showed an increased correlation between cardiac rate and cerebrovascular variables ($P < 0.001$ for HR- O_2Hb) while elderly subjects showed an inverse trend with decreased correlation values ($P < 0.01$ for HR-CBFV), with posture*age interaction effect found to be significant for all pairs except ABP- O_2Hb . The coupling between HR and ABP, which represents the behaviour of the cardiac baroreflex system, is also different for the two groups, with a decreased mean correlation value for elderly subjects but an increase for young subjects. However, the relationship between ABP and O_2Hb was found to be quite similar, with an increased correlation value in the upright position (though a statistical significance was only found in young subjects).

Figure 6.5 shows the maximum value of $WCC_{0,0}$, which is simply the common temporal cross-correlation. The correlation values are mostly lower than 0.5. The much lower value of correlation compared to Figure 6.4 is due to the fact that those variables are less correlated in other frequency bands such as the very low frequency band [0-0.0625] Hz (results not shown here). This clearly shows the advantage of the wavelet cross-correlation technique detecting an underlying relationship between two variables in a specific frequency interval, even though the overall correlation shows that the two variables are not strongly correlated over all frequencies.

6.3.4 Power spectral analysis

Figure 6.6 shows the group statistics for low frequency (LF) spectral power ([0.0625-0.125]Hz). HR LF power is found to increase on head-up tilt in young subjects, but to decrease in el-

Figure 6.5 Maximum correlation for each pair of HR, ABP, CBFV and O_2Hb original time series for both old and young subjects during supine rest and head-up tilt.

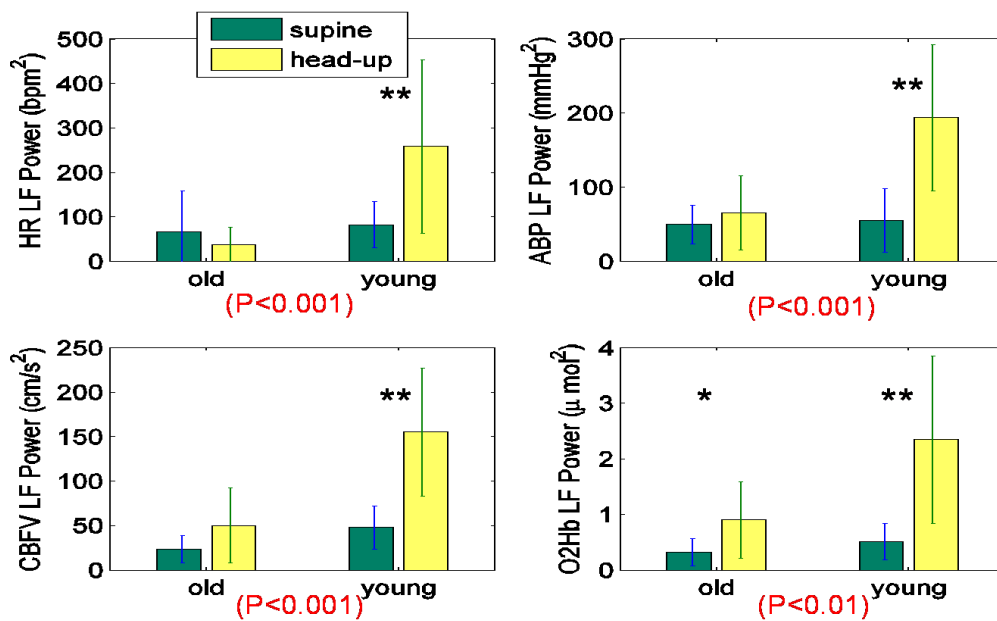


derly subjects (though a statistically significant result was not found, which might be due to large inter-subject variability), consistent with previous findings (Lipsitz et al., 1990). LF power spectra in other variables show similar posture dependence in that they increase upon head-up tilt for all subjects. In particular, O_2Hb LF power shows a statistically significant change for both old and young subject groups, in agreement with the results of Tachtsidis et al. (2004). As for other variables, however, statistically significant changes were only found in the young subjects.

6.4 Discussion

Wavelet cross-correlation between LFOs in each pair of HR, ABP, CBFV and O_2Hb has shown that for young healthy subjects passive head-up increases the wavelet cross-correlation for all pairs of parameters (statistically significant for HR-ABP, HR- O_2Hb , ABP- O_2Hb and CBFV- O_2Hb). This stronger linear interaction between these variables indicates a functioning cardiovascular and cerebral autonomic regulation system in response to orthostatic stress. However, elderly subjects show an inverse trend, with declining correlation values

Figure 6.6 Group statistical analysis of low frequency ([0.0625-0.125] Hz) spectral power in HR, ABP, CBFV and O_2Hb . Error bars represent standard deviation. * $P < 0.01$, ** $P < 0.001$, indicates the variables in which statistically significant postural changes were found. The age effect was also tested and statistically significant values are shown in red brackets. P-value refers to age*posture interaction effect tested by the two-way repeated measures ANOVA test.



in the upright position compared to the supine position for most pairs of parameters except ABP- O_2Hb (a non-significant increase was found). As a result, though the correlation values are comparable for the two groups in the supine rest position, lower correlation values of LFOs in cerebral hemodynamics and systemic cardiovascular dynamics are found in elderly subjects in the head-up position, especially for the coupling between heart rate and cerebrovascular variability ($P < 0.001$ for both HR-CBFV and HR- O_2Hb). This wavelet cross-correlation analysis of LFOs has clearly shown that different cardiovascular and cerebrovascular responses occur for young and elderly subjects, using just one postural manoeuvre for each participant.

Power spectral analysis showed that increases in low frequency power O_2Hb could be observed in both old and young subjects on assuming the upright posture, in agreement with Tachtsidis et al. (2004). Statistically significant changes were also observed in LF HR/ABP/CBFV power in young subjects but not in elderly subjects. Since LF oscillations could be a marker of sympathetic activity (Preiss and Polosa (1974)), these posture-related changes may be related to the degree of sympathetic stimulation (Tachtsidis et al. (2004)). Such posture dependence was not found in most variables for elderly subjects, which might suggest an impaired ability to transmit a pre-existing elevation in sympathetic activation into vascular resistance when facing the challenge of orthostatic stress. This could also explain why the effects of age were found to be more prominent in the tilt period.

The baroreceptor reflex is very sensitive to the decrease in mean arterial blood pressure that occurs immediately after passive tilt and is thus able to restore blood pressure within several seconds (Guyton (1980)). Baroreflex sensitivity is known to be impaired with ageing (Byrne et al. (1996); Colosimo et al. (1997); Laitinen et al. (2004)). Previous studies have attempted to evaluate baroreflex sensitivity on the basis of the interrelations between low frequency oscillations (Mayer wave) in blood pressure and heart rate (Watkins et al. (1995); Linden and Diehl (1996); Oka et al. (2003)). In particular, Linden and Diehl (1996) estimated baroreflex sensitivity using transfer function analysis and found a reduced coherence between HR and ABP for elderly subjects compared to young subjects, in-

dicating an impaired arterial baroreflex function associated with ageing. The same result was found here, showing a reduced correlation between HR and ABP for healthy elderly subjects. Moreover, this age dependency was only found for the tilted position. Again, this is consistent with previous findings of Linden and Diehl (1996).

Spontaneous low-frequency oscillations have also been observed in cerebral hemodynamics and metabolism in a number of experimental modalities, including functional near-infrared spectroscopy (Obrig et al. (2000); Mehagnoul-Schipper et al. (2000, 2001)), transcranial Doppler-sonography (Zhang et al. (1998a,b); Panerai et al. (2001, 1999)) and functional magnetic resonance imaging (Biswal et al. (1997, 1995); Shmueli et al. (2007)). There are a wide range of mechanisms which are thought to lead to these oscillations. Nilsson and Aalkjaer (2003) and Haddock and Hill (2005) both suggested that they can be attributed to spontaneous vasomotion of cerebral vessels which may become spatially entrained throughout the vasculature, possibly reflecting some underlying stimulus. Moreover, Schroeter et al. (2004) suggested that a reduction of LFOs observed in the ageing brain indicated a declining spontaneous activity in microvascular smooth muscle cells, in conjunction with increased vessel stiffness with ageing. Although the mean value of LF O_2Hb power was found to decline with age, no statistically significant difference was found in our study, which could be due to the short duration of measurements taken in the supine position.

Other literature has related cerebrovascular LFOs to the ‘Mayer Wave’ cardiovascular oscillations from their spectral features. Katura et al. (2006) investigated the causal relationship between them using information transfer analysis and found that about one third of the low frequency oscillations in O_2Hb originated from oscillations in HR and ABP. This is confirmed here since considerable wavelet cross-correlation values between HR/ABP and O_2Hb (young subject group-averaged values of about 0.5) are found in the supine position. In addition, our study has found that the correlation significantly increased in the head-up tilt period for young subjects. Though the correlation cannot reveal the direction of causality, it does indicate a stronger coupling between cerebral hemodynamics and sys-

temic regulation of the cardiovascular system when the body faces orthostatic challenge. Thus, it is possible that the increased LFOs in a posture-activated brain, identified both here and by Tachtsidis et al. (2004), can be attributed to increased systemic drive. Applying the information transfer method used in Katura et al. (2006) to the measurements of both postures might demonstrate whether this causal relation becomes more significant. This will be the subject of further investigation.

The effects of sympathetic activation on the cerebral circulation have always been a controversial topic. It is generally agreed that cerebral autoregulation is due to cooperative action of both sympathetically mediated and local myogenic or metabolic mechanisms (Priebe, 2000). Under normal conditions, the sympathetic tone of cerebral arteries is probably minimal, but under conditions of cerebrovascular stress induced by large pressure changes, cerebral sympathetic activation is thought to become more dominant (Harper et al., 1972; Branston, 1995). In particular Panerai *et al.*, (2001) investigated the CBFV response to ABP fluctuations occurring spontaneously and using thigh cuff, Valsalva, cold pressor, lower body negative pressure and hand grip tests. They found that the instantaneous ABP-CBFV relationship was dependent on the type of maneuver, which could reflect different degrees of sympathetic activation. Our study showed that a weaker ABP-CBFV coupling relationship in elderly subjects compared to young subjects was found in upright positions, which might indicate an altered cerebral autoregulation status with ageing (Paulson et al. (1990)). In previous studies, high correlation was observed in patients with head injury (Giller (1990); Czosnyka et al. (1996)), thus being interpreted as impaired autoregulation with a pressure-dependent flow (Czosnyka et al. (2008)). However, this traditional interpretation clearly cannot be applied to current study which has identified an increased correlation in young healthy subject. It is also worth to point out that this age effect could only be found when certain sympathetic mechanisms were activated by orthostatic challenge, which makes it hard to predict orthostatic hypotension for elderly subjects based on the cerebral autoregulation status identified from measurements of spontaneous fluctuations at rest.

In contrast to the age-correlated difference found in ABP-CBFV relationship, a stronger ABP- O_2Hb coupling relationship was found after posture change in both old and young subject groups. This could be due to the different cerebral region in which O_2Hb is measured by NIRS compared to that perfused by the middle cerebral artery (Harms et al. (2000)), since NIRS is sensitive to the microvascular territory (Schroeter et al. (2006)), whereas CBFV (as measured in the middle cerebral artery) represents larger vessels. Another possible reason is that the diameter of the middle cerebral artery may change due to sympathetic stimulation, thus the changes in CBFV may not necessarily reflect the changes in CBF.

Wavelet cross-correlation has previously been used in Rowley et al. (2007) to investigate the low frequency synchronization between ABP and O_2Hb for both healthy control subjects and autonomic failure patients. It has been shown that the frequency at which most synchronization occurs has a statistically significant difference between patients and controls. In this study, instead of using the continuous wavelet transform, as before, the maximal overlap discrete wavelet packet transform was adopted to decompose the original signals into wavelet coefficients of a series of frequency bands rather than a single frequency, in which the frequency interval around 0.1Hz, representing LFOs, has been our focus. The wavelet cross-correlation values have been used to assess the degree of synchronization of cerebral hemodynamics (CBFV and O_2Hb) and systemic cardiovascular changes (HR and ABP), which is easier to interpret as the coupling of cerebral circulation and cardiovascular systemic regulation systems may become weak even in healthy elderly subjects.

Quantification of the effects of CO₂ on the resting BOLD signal

7.1 Introduction

Physiological fluctuations in the blood oxygen level-dependent (BOLD) signal are significant components of noise in functional magnetic resonance imaging (fMRI) studies. In contrast to system and thermal noise, the noise arising from physiological sources depends on the total BOLD signal strength and therefore becomes a larger fraction of the total noise as the signal increases (Krüger et al. (2001); Krüger and Glover (2001); Triantafyllou et al. (2005)), for example with increased magnetic field strength. They become particularly problematic when their spectral characteristics overlap with those of task-related signals, as conventional noise reduction strategies, such as fixed bandwidth band-rejection filtering, are unable to distinguish them from the signal of interest (Biswal et al. (1996)).

Several physiological noise sources have been identified, including cardiac (Dagli et al. (1999); Bhattacharyya and Lowe (2004)) and respiratory cycles (Birn et al. (2006)) as well as uncharacterized low-frequency fluctuations (Biswal et al. (1996)). Though their precise physiological origin is unclear, these low-frequency fluctuations observed in cerebral BOLD signals are likely to arise from haemodynamic and metabolic oscillations (Wise et al.

(2004); Triantafyllou et al. (2005)). Besides BOLD-fMRI, these spontaneous low-frequency variations in cerebral blood flow and oxygenation can also be observed by Transcranial Doppler Ultrasound (TCD) and near infrared spectroscopy (NIRS). A comprehensive review can be found in Obrig et al. (2000). They are of great interest as they may reveal autoregulatory mechanisms of the brain vasculature and are altered by pathological conditions (Diehl et al. (1995); Hu et al. (1999)). This physiological noise not only negatively affects conventional task-based fMRI experiments, but also leads to low-frequency variations in the resting BOLD signal in the absence of external stimuli, given the correlations found between BOLD and flow signals (Biswal et al. (1997); Lowe et al. (1998)). Fluctuations of neuronal origin are also demonstrated by the evidence that the underlying fluctuations are correlated with modulations of cortical electrical activity detected by EEG (Goldman et al. (2002); Moosmann et al. (2003)). It is still uncertain whether the fluctuations in resting fMRI signal are a direct consequence of neuronal activity or dominated by physiological variations (De Luca et al. (2006)). In this study, we thus investigate one source of widespread low frequency BOLD signal variations related to carbon dioxide.

Carbon dioxide (CO_2) in arterial blood is a potent vasodilator which can modulate global cerebral blood flow (CBF) (Grubb et al. (1974); Hoge et al. (1999a,b)). The CBF increase induced by hypercapnia will lead to dilution of venous deoxyhemoglobin and increase the global BOLD signal, whereas the CBF decrease due to hypocapnia reduces the BOLD signal (Cohen et al. (2002); Bandettini and Wong (1997); Corfield et al. (2001); Posse et al. (2001); Kemna and Posse (2001); Vesely et al. (2001)). Significant regional variability has been found for both the magnitude and the time course of the BOLD signal response to changes in P_{aCO_2} (Kastrup et al. (1999); Rostrup et al. (2000)).

At rest, changes in P_{aCO_2} can be represented by changes in the end-tidal partial pressure of carbon dioxide (P_{ETCO_2}) (Robbins et al. (1990); Young et al. (1991)). Fluctuations in resting P_{ETCO_2} have been observed principally in the range 0-0.05Hz (Modarreszadeh and Bruce (1994)). The source of such fluctuations may be the feedback control of breathing via chemoreflexes seeking to maintain optimal blood gas levels (Wise et al. (2004)). These

low-frequency fluctuations in P_{ETCO_2} have been associated with fluctuations in CBF velocity measured in the middle cerebral artery (MCA) (Mitsis et al. (2002, 2004b); Panerai et al. (2000)) and have been used to explain CBFV variability in the same frequency range (Chapter 4). The effects of P_{aCO_2} fluctuations on cerebral oxygenation and metabolism were investigated in Wise et al. (2004) by calculating the regression coefficients between breath-to-breath P_{ETCO_2} and resting BOLD time series on a voxel-to-voxel basis. Again, these P_{ETCO_2} -related BOLD signal fluctuations showed regional differences, suggesting variability of the responsiveness to carbon dioxide at rest (Wise et al. (2004)). However, the linear regression analysis (equivalent to correlation coefficient) used in Wise et al. (2004) makes an additional assumption of the data, stationarity, which might not hold for P_{ETCO_2} and resting *BOLD* time series.

It is also well known that the relationship between CO_2 and CBF is strongly frequency dependent, in which CO_2 effects are concentrated in the low frequency range 0-0.05Hz (Mitsis et al. (2004b), Chapter 4). We therefore hypothesize that the effects of CO_2 on the resting state BOLD signal are also restricted within low frequencies. Wavelet cross-correlation analysis (both continuous and discrete wavelet methods) will be used to assess the coupling of the two time series at different frequencies, in contrast to ordinary correlation which is the average value over the whole frequency spectrum. In addition, a physiological based model relating the BOLD signal to CO_2 changes will be used to help to interpret the clinical results.

7.2 Methods

The procedures performed in this study were approved by the Cardiff Clinical Research Ethics Committee. All volunteers gave informed consent before taking part.

7.2.1 Measurements

Eleven healthy volunteers underwent functional MRI testing. Imaging was performed at 3T with an Oxford Magnet Technology, 1m bore magnet driven by a Varian Unity Inova console. Gradient-echo echo-planar imaging (EPI) was performed giving T_2^* weighting for BOLD contrast (image matrix: 64×64 ; 3×4 mm pixels; echo time (TE=30ms)).

Each volunteer underwent two fMRI scans of 20-min duration, instructed to keep their eyes closed during one scan and open during the other. Each scan was performed with 24 contiguous axial slices of 6 mm thickness covering the whole brain with a flip angle of 90° and repetition time TR=3s. For each subject, a T_1 -weighted structural scan (64 contiguous 3-mm axial slices; in-plane field of view 256 mm, 1×1 mm pixels) was acquired and used to assist in placing individual subjects's data into a common stereotactic space.

While lying supine in the MRI scanner, subjects wore a nasal cannula through which respired gases were sampled by an MR compatible patient monitor, incorporating a capnograph (Multigas 9500, MR Equipment Corp., Bay Shore, NY) situated outside the magnet room. The capnograph measured the P_{CO_2} in the expirate by exploiting the infrared absorption spectrum of CO_2 . The partial pressure of CO_2 was logged at 10ms intervals using in-house software (CCARM, FMRIB Centre, Oxford University, UK) and P_{ETCO_2} was calculated for each breath. The combined gas transport delay and dispersion along the sample tube was factored into the analysis of the CO_2 recordings. Subjects wore an MR compatible respiratory monitor (MR Equipment Corp.) consisting of bellows around the chest, the internal pressure of which encoded the chest position and hence the phase of the breathing cycle. Triggers for each scanner volume acquired were logged in synchrony with physiological quantities to allow accurate synchronization with fMRI data.

7.2.2 Image analysis

Image analysis to reveal significant P_{ETCO_2} -related changes in the BOLD signal was performed on each subject's data using the FEAT software (FMRIB Expert Analysis Tool,

v5, <http://www.fmrib.ox.ac.uk/fsl>, Oxford University, UK) (Smith et al. (2001)). Preprocessing steps were applied to each subject's time series of fMRI volumes: motion correction (Bannister and Jenkinson (2001); Jenkinson and Smith (2001)); spatial smoothing using a Gaussian kernel of full-width-half-maximum 5 mm; high-pass temporal filtering (Gaussian-weighted least squares straight line fitting, with a high-pass filter cut-off of 100 s) and subtraction of the mean of each voxel time-course from that time course.

Linear models were constructed to describe the fMRI data on a voxel by voxel basis, with local autocorrection correction (Woolrich et al. (2001)). The main covariate of interest was the P_{ETCO_2} time series high-passed by the same temporal filter applied previously to the BOLD signal. First-level regression analysis was used to determine the effect of CO_2 on the fMRI signal at each image voxel; regression coefficients (equivalent to correlation coefficients) of which were subsequently transformed to z statistics¹ indicating the statistical significance of the P_{ETCO_2} -related BOLD signal change. Regions of grey and white matter were segmented from the high-quality T1-weighted structure image for each subject. Regional differences in the P_{ETCO_2} -related BOLD signal change were decided by coregistration of the low spatial-resolution image with the high spatial-resolution segmented image.

7.2.3 Data analysis

Power spectral analysis

Power spectral densities were calculated for each of the post-processed time series (after high-pass filtering removing low frequency variation with a period longer than 90s) with the Welch technique (Welch (1967)) with a 128-point (384 s) Hanning window with an overlap of 56 points.

Wavelet cross-correlation analysis

¹The z statistic has a normal distribution with a mean of zero and a standard deviation of one. Therefore, if we know the mean and standard deviation for a population, we can identify a z-score given the raw score.

Wavelet cross-correlation was defined as the cross-correlation between the wavelet coefficients of two time series X and Y for a relative time shift τ :

$$WCC(\tau) = \frac{|R_{X,Y}(W^X, W^Y, \tau)|}{\sqrt{|R_{X,X}(W^X, 0) \bullet R_{Y,Y}(W^Y, 0)|}}, \quad (7.1)$$

where the wavelet coefficients, W^X and W^Y , were computed by the continuous complex Morlet wavelet transform using the MATLAB (Mathworks Natick, MA) wavelet toolbox function `cwt`. This gave two complex time series, $W^X(a, t)$ and $W^Y(a, t)$, thus wavelet cross-correlation $WCC(a, \tau)$ represents the cross-spectral power in the two time series (shifted relative to each other by τ) as a fraction of the total power in the two time series. At a given wavelet scale $WCC(a, \tau) = 1$ would indicate that the coefficients of the two wavelet transforms were related to each other by a simple scaling factor, suggesting strong synchronization at this frequency. For a more detailed explanation of wavelet cross-correlation see Grinsted et al. (2004) and Rowley et al. (2007).

The maximal overlap discrete wavelet packet transform (MODWPT) described in Chapter 6 was also used here to decompose the original signals into wavelet coefficients of a series of frequency bands rather than a single frequency. Thus, the discrete wavelet cross-correlation can be calculated through cross-correlation of these discrete wavelet coefficients. This is not only much faster than the continuous equivalent, thus allowing for instantaneous analysis, but it is also ideal for assessing the coupling and synchronization between oscillations found in different variables in different frequency bands.

7.2.4 Model simulation

Synthetic data was also generated using a linear time-invariant model. The system comprises two transfer functions for $u - BOLD$ and $P_{ETCO_2} - BOLD$, which are linear approximations of the physiologically-based model described in Section 3.2. The linearisation procedure can be found in Section 3.4.3. Measured P_{ETCO_2} data of a single subject were used as a sample of one model input. In the eyeopen condition, random data are also generated to mimic the baseline neural activity, u , which will be added as the second model input. No

such simulated neural activity is used in the eyeshut case. Essentially, the model hypothesizes that the eyesopen and eyeshut cases are associated with different levels of neural activity, but the system behaviour is identical.

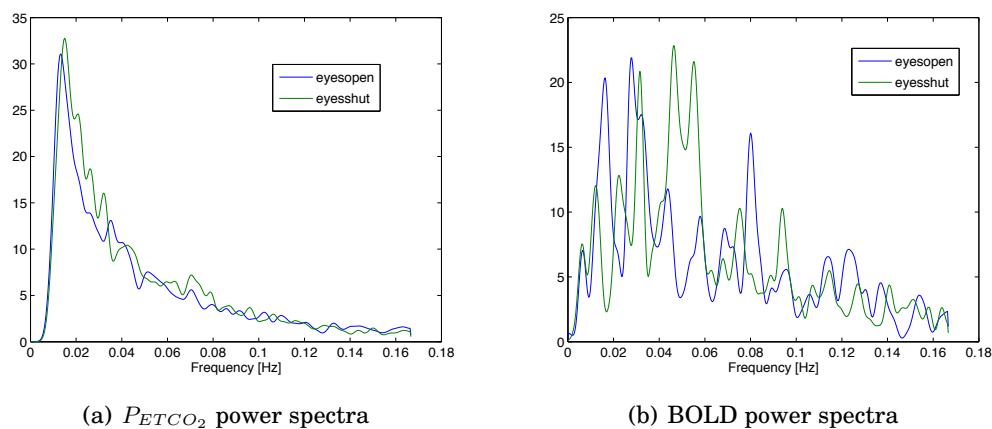
Discrete wavelet cross-correlation method was used to analyse the coupling and synchronization between one model input, P_{ETCO_2} , and the model output, $BOLD$, with or without another model input, u . The simulation results then help to interpret the different experimental results obtained in the eyes open and shut cases.

7.3 Results

7.3.1 Power spectra of P_{ETCO_2} and $BOLD$ fluctuations

Figure 7.1(a) shows the power spectra of the P_{ETCO_2} time course, averaged over all subjects in each condition. The figure shows that most of P_{ETCO_2} variations occur at very low frequencies ($< 0.1Hz$) and that there are no distinct frequency peaks in the averaged spectra. Compared to the P_{ETCO_2} power spectra which are concentrated at low frequencies, the $BOLD$ signals are broadband, with power spread over all frequencies (0 to sampling frequency/2), as shown in Figure 7.1(b).

Figure 7.1 (a) Group-averaged power spectra of P_{ETCO_2} variations in both eyes open and shut cases. (b) Power spectra of $BOLD$ fluctuations of a typical voxel.



7.3.2 Linear regression analysis

Figure 7.2 illustrates the regional distribution of P_{ETCO_2} -related BOLD signal fluctuations in both the eyes open and shut cases for a single subject, identified from the first-level linear regression analysis. In the eyeshut condition, the significant regions of BOLD fluctuations are widespread whereas fewer regions are found to be correlated with P_{ETCO_2} in the eyeopen case. The BOLD time series in voxel (46,28,22) in both conditions are plotted on the right, together with the predicted BOLD response, scaled from P_{ETCO_2} . For this particular voxel, the correlation coefficients between the P_{ETCO_2} and BOLD timeseries are found to be quite different in the two conditions: $R = 0.1243$ in the eyeopen and $R = 0.3768$ in the eyeshut cases, with a statistically significant correlation found in the eyeshut but not in the eyeopen case.

The first-level linear regression analysis was then applied to all subjects. The fraction of voxels whose BOLD signals showed a statistically significant regression with P_{ETCO_2} for each subject is shown in Table 7.1. The percentage of voxels showing significantly P_{ETCO_2} -related BOLD are found to be quite similar for grey and white matters for each subject. The group-averaged results suggest that the effect of CO_2 on the baseline BOLD fluctuations with eyes closed are slightly larger than that with eyeopen. However, due to the large cross-subject variability, statistical significance was not achieved.

7.3.3 Cross-correlation analysis

Cross-correlation analysis was then performed to look for correlations between the P_{ETCO_2} and BOLD signals for each voxel for all possible temporal shifts (both positive and negative) within 7TR (21 sec). The maximum correlation and time shift corresponding to the maximum correlation value were calculated for each voxel, thus generating a correlation map (Figure 7.3) and a time shift map (Figure 7.4). Both the correlation map and the time shift map for each subject are then registered to the segmented grey and white matter from the structure image. Mean correlation averaged over grey and white matter are

Figure 7.2 Left: Z-maps of regression between BOLD and P_{ETCO_2} (P_{ETCO_2} -related signal changes) in both eyeopen (a) and eyeshut (c) conditions for a single subject (a cluster in the black square being picked for wavelet cross-correlation presented below). Significant regions are displayed with a threshold of $Z > 2.3$ and with a cluster probability threshold applied of $P < 0.05$ superimposed upon the volume-averaged EPI image. Right: BOLD time series in voxel (46,28,22) in (b) eyeopen and (d) eyeshut case. Predicted BOLD responses using P_{ETCO_2} time series are also plotted for comparison.

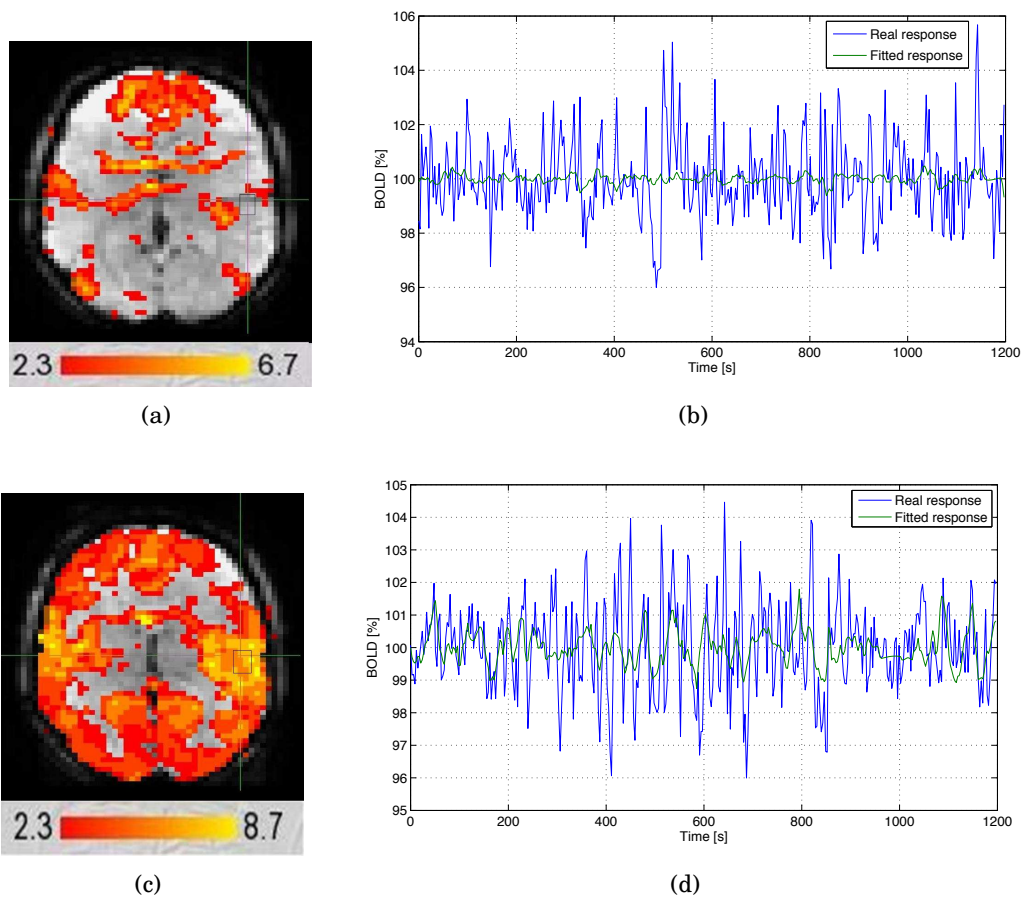


Table 7.1 Mean percentage of voxels showing significant P_{ETCO_2} regression

Subject	Eyeopen (%)		Eyeshut (%)	
	Grey matter	White matter	Grey matter	White Matter
1	15.1	16.5	54.7	59.7
2	3.2	2.9	1.7	1.9
3	0	0	37.3	30.1
4	19.6	22.6	16.1	17.5
5	0	0	0.4	0.4
6	16.5	19.6	43.2	40.4
7	1.3	1.2	26.7	26.2
8	2.7	2.8	1.9	2.2
9	51.9	50.8	2.3	1.9
10	12.6	12.7	7.1	6.9
11	0	0	3.3	2.6
Mean	11.2±15.4	11.7±15.5	17.7±19.6	17.3±19.7

summarised in Table 7.2, suggesting a slightly stronger coupling between these two fluctuations in grey matter compared to white matter for both the eyes open and shut cases². A quicker BOLD response is also found in grey matter than in white matter, with statistical significance achieved in the eyeshut condition. These findings concerning regional difference agree well with the literature (Rostrup et al. (2000); Wise et al. (2004)). Besides the regional difference, time lags in eyeopen case are consistently larger than eyeshut case, which partly contributes to the different regression result (correlation at zero time shift) between the two cases.

Table 7.2 Group statistics of maximum cross-correlation and corresponding time shifts between P_{ETCO_2} and BOLD fluctuations. Significantly stronger correlation and shorter time delay were found in the grey matter than white matter, indicated by a two-tailed paired Student's t test at $*P < 0.05$. Significantly longer time delay were found in eyeopen than eyeshut condition, indicated by a two-tailed Student t test at $^+P < 0.05$.

Condition	Maximum cross-correlation		Time delay [sec]	
	Eyesopen	Eyesshut	Eyesopen	Eyesshut
Grey matter	0.17 ± 0.08*	0.18 ± 0.07*	8.9 ± 2.3 ⁺	6.7 ± 3.0*
White matter	0.16 ± 0.07	0.17 ± 0.06	9.1 ± 2.1 ⁺	7.3 ± 3.2

²During to the large cross-subject variability, this regional trend may not be very obvious, but paired t-test does show a statistical significant increases in correlation in grey matter than in white matter.

Figure 7.3 Maximum correlation map between BOLD and P_{ETCO_2} (P_{ETCO_2} -related signal changes) across all possible time delay (0-21 sec) in both (a) eyeopen and (b) eyeshut conditions for a single subject.

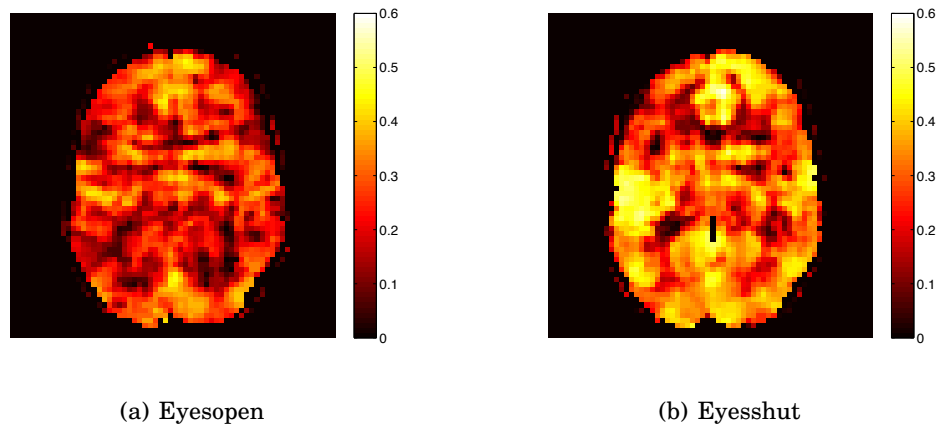
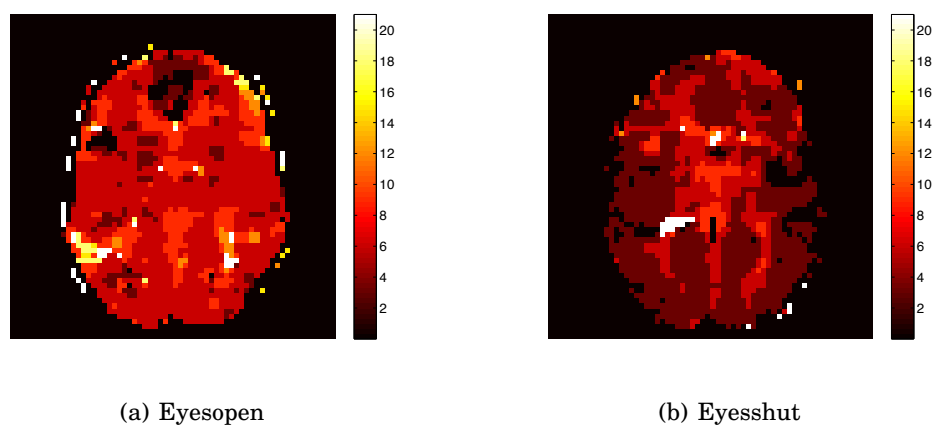


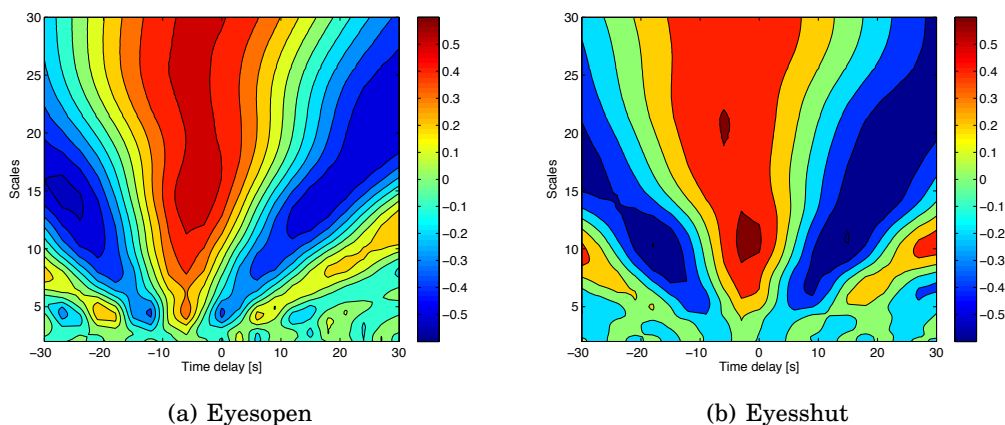
Figure 7.4 Time shift map between BOLD and P_{ETCO_2} in both (a) eyeopen and (b) eyeshut conditions for a single subject.



7.3.4 Wavelet cross-correlation analysis

A cluster with 90 voxels in the parietal lobe was chosen, illustrated by the black square in Figure 7.2, where BOLD fluctuations were found to be correlated with P_{ETCO_2} changes by the previous regression analysis in the eyeshut but not in the eyeopen case. Cluster-averaged continuous wavelet cross-correlation between the two time series, Figure 7.5, illustrates that relatively high values of correlation were found at low frequencies (scales 7-30, equivalent to 0.01-0.05Hz, sampling time, 3s), suggesting a stronger coupling in that frequency range. Given the previous findings that the effects of CO_2 on CBF variations are concentrated in the low frequency range (Chapter 4), it is not surprising that the contribution of CO_2 to the BOLD signal is also restricted within the low frequency region. Differences between the eyeopen and shut cases are reflected in: 1) Peak value at scale 10 (0.033Hz) in the eyes shut but not open case; 2) Slightly larger time delay in the eyeopen compared to the eyeshut case.

Figure 7.5 Cluster-averaged continuous wavelet cross-correlation between BOLD and P_{ETCO_2} (P_{ETCO_2} -related signal changes) in both eyeopen (a) and eyeshut (b) conditions for a single subject.



Discrete wavelet cross-correlation was also used to investigate the frequency-dependent coupling between the P_{ETCO_2} and BOLD time series. Figure 7.6 (top left) shows the cluster-averaged zero-level wavelet cross-correlation, which is equivalent to ordinary cross-correlation, over a range of time delay, with the correlation coefficients at zero time delay

marked. Although the maximum values of cross-correlation are similar for the eyes open and shut cases, the correlation coefficients are significantly different, which is primarily due to a change in the time delay between the two conditions. Wavelet cross-correlation values for the low frequency oscillations (0-0.04Hz, where most P_{ETCO_2} power is concentrated for this subject) between the two time series (top right) are significantly higher than for ordinary correlation ($P < 0.01$ with eyes both open and shut). The overlapped error-bar illustrates similar trends were now found for both eye conditions ($P = 0.17$ for maximum wavelet correlation values), in contrast to the significantly different P_{ETCO_2} -related BOLD signal change between the two cases previously identified by regression analysis. The correlation curve for the other frequency band, i.e. 0.04-0.08Hz, clearly illustrates the different temporal dynamics of P_{ETCO_2} related BOLD response between the two conditions. Correlation for high frequencies, 0.08-0.16Hz, collapses since there is no P_{ETCO_2} power in that high frequency range.

Figure 7.6 Cluster-averaged wavelet cross-correlation between P_{ETCO_2} and BOLD fluctuations across different frequency bands. Error bars represent standard deviation.

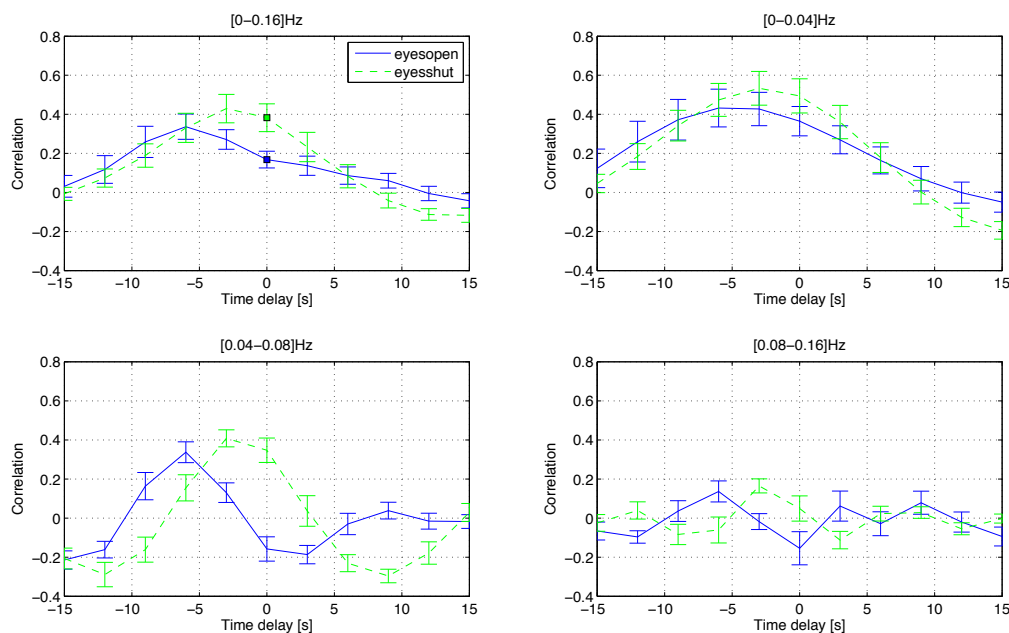
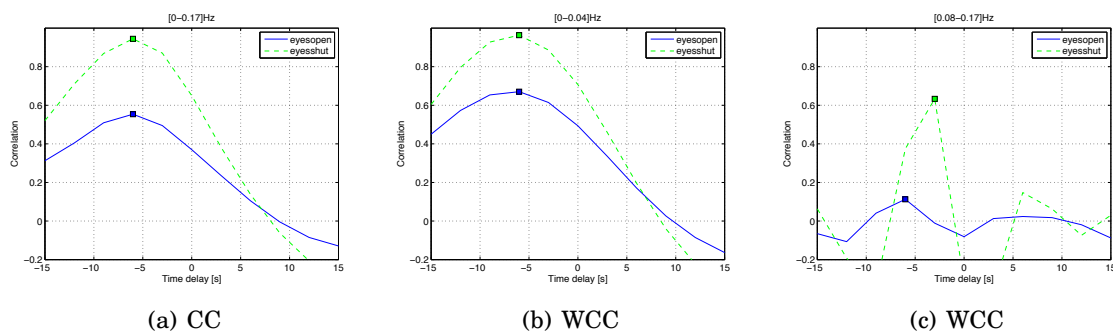


Figure 7.7(a) plots the cross-correlation between model input, measured P_{ETCO_2} , and model

output, simulated *BOLD* response, with and without another model input, simulated neural activity. In the simulated eyeshut case, the maximum cross-correlation (marked with the blue colour box) is close to the theoretical value, 1, with a time delay of 6 s. This 6 s time delay predicted by the model is consistent with findings in Wise et al. (2004). In the simulated eyeopen case, the correlation values reduce, due to the effects of the additional disturbing input that resembles neural activity. However, the 6 s time delay remains. The discrete wavelet transform was used to decompose the signals into different frequency bands and wavelet cross-correlation provides an assessment of the coupling associated with a particular frequency band, 0-0.04Hz being chosen here as it contains most of the P_{ETCO_2} power. As shown in Figure 7.7(b), maximum wavelet cross-correlation value is higher than the corresponding ordinary cross-correlation in eyeopen case, suggesting that it is less influenced by unmeasured variability. In contrast, the coupling between P_{ETCO_2} and *BOLD* of other frequency band, for example, [0.08-0.17]Hz, is completely destroyed by the disturbing neural activity input, (Figure 7.7(c)), the power of which now become dominant at those frequencies.

Figure 7.7 a) Cross-correlation between P_{ETCO_2} and model simulated *BOLD* response in both eyeopen and shut conditions. b) Wavelet cross-correlation between their low frequency oscillations in the range of 0-0.04Hz. c) Wavelet cross-correlation between higher frequency oscillations in the range of 0.08-0.17Hz. Spots indicate the maximum wavelet cross-correlations.



7.4 Discussion

The data presented here suggest that spontaneous fluctuations in arterial CO_2 level cause BOLD signal fluctuations at a level that is detectable and significant, consistent with previous findings of Wise et al. (2004). It is well known that carbon dioxide has a potent vasodilatory effect which produces increases in CBF and CBV (Grubb et al. (1974)). With the recent development of techniques used to measure cerebral blood flow and oxygenation and to delicately control blood gas level, numerous studies have investigated the time course of the vascular response to CO_2 , including both forced CO_2 challenges such as hypercapnia or hypocapnia (Poulin et al. (1996, 1998); Posse et al. (1997); Cohen et al. (2002)), and spontaneous P_{ETCO_2} fluctuations (Panerai et al. (2000); Mitsis et al. (2004b); Wise et al. (2004)). The delay time between P_{ETCO_2} and changes in cerebrovascular dynamics would consist of both the transport delay of blood from the lungs to the brain and the time for the vasculature to respond. This is estimated to be approximately 6s measured using TCD ultrasound (Poulin et al. (1996)) and 5-10s during BOLD contrast fMRI (Posse et al. (1997)), depending on the different methodology. The estimated time delay in the present study, 7s in eyeshut and 9s in the eyeopen, are both in broad agreement with the previous literature.

The coupling of spontaneous P_{ETCO_2} fluctuations and the resting BOLD signal was significantly larger in the grey matter than in the white matter. This is likely to reflect differences in metabolic activity, vascular regulation and capillary density (Wise et al. (2004)). The white matter has a lower blood volume and metabolic activity than the cortical grey matter. Regional differences are also found in the time course of the vascular response: BOLD signal changes take place slower in the white matter than in the grey matter to hypercapnia challenge (Rostrup et al. (2000)), again supported by the present study which shows the same trend. The differences in temporal dynamics may suggest tissue specific differences in the biochemical mechanisms responsible for metabolic activity and vascular regulation. A major influence is likely to be the resting values of cerebral blood volume and regional microvascular anatomy (Bandettini and Wong (1997)). For example, the transit

time for red blood cells are found to be different between grey and white matter (Bereczki et al. (1993)), which must be a factor in determining the time required for changing the local capillary or venular oxygenation.

It is also worth noticing that the time delay of the BOLD signal change is found to be consistently larger in the eyeopen than in the eyeshut case, for both grey and white matter. A possible reason is that the relation between BOLD and P_{ETCO_2} may be blurred by the presence of a concomitant change in neuronal activity and that the eyes open and shut cases are associated with different degree of this disturbance. In this study, the effect of neuronal activity has been investigated using a physiological-based model which includes both P_{ETCO_2} and simulated neuronal activity as inputs. A reduced correlation between P_{ETCO_2} and BOLD due to neural activity was observed, but not an altered time delay. This could be due to the fact that the simulated neuronal activity used here, random noise, may not be a good representation of real neural activity. Nevertheless, the model simulations demonstrates that wavelet cross-correlation is a powerful tool to assess the frequency-dependent coupling between two variables in the presence of additional variability.

Besides P_{ETCO_2} fluctuations, other sources have also been suggested to account for low-frequency BOLD oscillations, including fluctuations of neuronal, metabolic and vascular origin (Elwell et al. (1999); Hudetz et al. (1998); Obrig et al. (2000)). Vascular fluctuations were observed in TCD measured CBF velocity with a frequency of 0.008-0.05Hz, known as B waves (Lundberg (1960)), which are thought to be caused by changes in blood vessel diameter (Diehl et al. (1991)). Cardiovascular oscillations, Mayer waves in heart rate and systemic arterial blood pressure around 0.1Hz also create fluctuations at the same frequency in cerebral dynamics. A recent study, Shmueli et al. (2007), quantify the low-frequency fluctuations in the cardiac rate as a source of variance in the resting-state fMRI BOLD.

7.5 Conclusion

The results demonstrate that P_{ETCO_2} fluctuations are an important source of low-frequency variations in resting-state BOLD fMRI data. The time delay between the P_{ETCO_2} and BOLD signals was found to be significantly shorter in the eyeshut than in the eyeopen case. This difference in temporal dynamics would contribute to the observed large variability of the percentage of voxels which show significant P_{ETCO_2} -related BOLD signal changes between the two cases, based on linear regression analysis which is equivalent to correlation at zero time shift. A varied time shift should be carefully compensated for in such analysis.

Wavelet cross-correlation was also used to assess the frequency-dependence of the P_{ETCO_2} -BOLD coupling, which illustrates that the effects of P_{ETCO_2} are concentrated in the low frequency band 0-0.08Hz. Simulation results of a physiologically-based model demonstrate that wavelet cross-correlation is robust in identifying the coupling of two variables in the presence of additional disturbing variability.

Conclusion

8.1 Summary

This thesis has presented a combined analysis which involves both physiological modelling and signal processing as well as the analysis of clinical data concerning the regulation of cerebral blood flow. A physiologically-based model, described in Chapter 3, is able to predict the response of the cerebral vasculature to arterial blood pressure, arterial CO_2 concentration and neural activation. This combined haemodynamic circuit makes it possible to investigate the interaction between pressure autoregulation, CO_2 reactivity and functional activation, which are often assumed to be separate pathways. The derived linear version of the model has reduced freedom in the model parameters, which can thus be related to the impulse or step response directly estimated from experimental data, providing an effective way to validate the model. The model approach used here is not only able to test the hypotheses made about the regulation mechanisms, but also to provide a simulation tool to test the signal processing techniques and to help explain experimental observations. A series of these studies are presented in Chapters 4 5 and 7.

Chapter 4 uses a standard statistical technique to demonstrate that including experimentally measured blood gas concentrations as additional inputs of the system can give in-

creased confidence (as measured by the coherence function) in the results obtained from system identification of cerebral autoregulation at low frequencies (0-0.05Hz). This demonstrates the important role that CO_2 plays in the control of cerebral blood flow, and the need to include its measurement to assess correctly the coherence of transfer function analysis in clinical autoregulation studies. High values of multiple coherence suggests that multivariate system identification on fluctuations in TCD-measured CBFV, ABP, P_{ETCO_2} and P_{ETO_2} recorded from healthy human subjects allows approximate recovery of the dynamics of cerebral autoregulation. A significant limitation of transfer function estimation is, however, its averaging of the system dynamics over time.

The second study, described in Chapter 5, thus showed how the continuous wavelet transform could be used to study the time-varying phase dynamics of the relationship between ABP and CBFV, without making the assumption of stationarity. It was found, in the same data-set as in Chapter 4, that the wavelet recovered instantaneous phase relationship was modulated by P_{ETCO_2} fluctuations. The multivariate system identification techniques described in Chapter 4 were used to derive a correction term that can remove the effects of P_{ETCO_2} variations. The corrected phase relationship between ABP and CBFV is found to vary less with time, as suggested by the increased synchronization index. This illustrates that some of the apparent nonstationarity can be attributed to the unmeasured variability.

Chapter 6 showed how wavelet cross-correlation could be used to assess the degree of coupling between two time series associated with different frequency bands. Compared to the continuous wavelet transform used in Chapter 5, the maximal overlap wavelet packet transform used here provides a more efficient way for time-frequency decomposition of signals. The correlation between the low frequency oscillations in cerebral haemodynamics and systemic cardiovascular changes in young subjects are found to be significantly higher than that of old subjects in head-up tilt, but not in the supine position. The coupling between the cerebrovascular and wider cardiovascular systems in response to orthostatic stress thus appears to be impaired with ageing.

In Chapter 7 it was demonstrated how the wavelet phase synchronization algorithm used in Chapter 5 and the wavelet cross-correlation described in Chapter 6 can provide an alternative method to link resting BOLD fluctuations to spontaneous fluctuations in P_{ETCO_2} , besides the classic correlation coefficient and regression analysis methods. Though regression analysis found significantly different P_{ETCO_2} correlated changes in baseline BOLD signal between the eyeopen and eyeshut cases by regression analysis, wavelet cross-correlation analysis shows that there appears to be no major difference apart from the time shift (i.e. there appears to be no amplitude variation). This suggests that the time shift between P_{ETCO_2} and BOLD is a critical variable which should be carefully compensated for in regression analysis.

The conclusions of this thesis based upon the results of both simulation studies and detailed analysis of experimental data are thus:

- 1. Model simulations show that pressure autoregulation and CO_2 reactivity have a large effect on the response of the cerebral vasculature to functional activation, suggesting that it is extremely important to consider systemic changes when performing functional imaging studies, in particular for patient groups who have impaired cerebral behaviour.*
- 2. Functional activation and CO_2 reactivity will have a large influence on the results of existing analysis techniques which attempt to assess autoregulation status by considering only pressure and flow changes.*
- 3. Wavelet-based techniques (i.e cross-correlation and phase synchronization) provide a robust assessment of cerebral and systemic coupling in the presence of a multivariate and time-varying system.*

8.2 Limitations and Future work

In Chapter 5, the phase synchronization method only make use of the phase information of ABP and $CBFV$ measurements. In contrast, wavelet cross-correlation used in Rowley et al. (2007) and Chapter 6 incorporated the phase as well as amplitude information. For

a narrowband signal, instantaneous phase would be an ideal representation, thus circular mean phase and synchronization index over time are better indices of coupling than correlation for this particular problem. Unfortunately, most signals are not narrowband sinusoids. The real relationship between correlation and synchronization need further investigation.

The phase synchronization method was used to analyse the phase dynamics of cerebral autoregulation in the presence of additional variability in Chapter 5. The correction term accounting for CO_2 effects is derived by multivariate transfer function analysis, which makes an assumption of stationarity on the $CO_2 - CBFV$ relationship. However, this stationarity assumption may not be valid under certain physiological or pathological conditions, such as physical exercise or tilting. In order accurately to estimate the correlation term, a time-varying transfer function is required to replace the time-invariant algorithm used currently. A very promising time-varying system identification algorithm was proposed in Rowley et al. (2007), which uses the maximal overlap discrete wavelet packet transform based on Hilbert wavelet pairs to estimate both auto and cross power spectra. This could have the potential to resolve current conflicts and to lead to a better estimator of the dynamics of cerebral autoregulation.

Both Chapters 6 and 7 adopted the Maximal Overlap Wavelet Packet Transform based on Hilbert wavelet pair filters, which are designed via spectral factorization to form an approximate Hilbert relationship (Selesnick (2002)). Since the wavelet filters do not form a perfect Hilbert relationship ¹, the approximation of Hilbert relationship of the real and imaginary component of wavelet coefficients becomes worse with increasing level of decomposition. In order to control the effects of this approximation, it is important to avoid splitting a frequency band when not required. A very promising optimization algorithm for decomposition was proposed in Olhede and Walden (2004), which uses an FFT based estimate of bandwidth for each node of the wavelet packet transform and seeks optimized band

¹It is not possible to design a pair of wavelet filters that are exact Hilbert transforms because of the finite length of real filters.

splitting with monocomponent signals in each band. This would minimize total bandwidth over the wavelet packet tree yet result in better representation of the system dynamics.

In Chapter 6, MODHWPT was used to provide a series band-pass filters which decompose original signal to a series of signal associated with different frequency bands. Compared to conventional overlapped FFT method, MODHWPT served as an adaptive way automatically determining the time window for frequency decomposition, which is a big advantage. However, the potential of wavelet has not been fully explored here as the signal we applied in this chapter has already reached a stable level, while wavelet is known to be most capable dealing with time-varying signal, e.g. the signal representing transient changes from supine to tilt-up position. As a result, our next step will be investigating the age-dependence of transient cardiovascular response and autoregulation to orthostatic challenge by exploring this transient signal measured right after tilt-up position using MODHWPT.

As a complex wavelet transform, MODHWPT incorporates magnitude as well as instantaneous phase of a signal. Its application for investigating phase dynamics was first proposed in Whitcher et al. (2005) for the analysis of electromyographic (EMG) data, which was later introduced into the cerebral autoregulation field by Rowley et al. (2007). In particular, Rowley et al. (2007) extended its application from dealing with univariate systems to the estimation of bivariate phase relationship of two signals in a multivariate coupled system, i.e. in the presence of additional disturbing signals, which is very common in real physiological systems of biomedical engineering. This new approach would be ideal to examine various physiological sources potentially corresponding to variations in the resting BOLD signal, including EEG which represents neural activity, P_{ETCO_2} variations and cardiac rate and will be a target of future work.

Bibliography

() *Wavelet Toolbox*.

- Aaslid, R., Lindegaard, K. F., Sorteberg, W. and Nornes, H. (1989) Cerebral autoregulation dynamics in humans. *Stroke*, **20**, 45–52.
- Aaslid, R., Markwalder, T. M. and Nornes, H. (1982) Noninvasive transcranial doppler ultrasound recording of flow velocity in basal cerebral arteries. *J Neurosurg*, **57**, 769–774.
- Aaslid, R., Newell, D. W., Stooss, R., Sorteberg, W. and Lindegaard, K. F. (1991) Assessment of cerebral autoregulation dynamics from simultaneous arterial and venous transcranial doppler recordings in humans. *Stroke*, **22**, 1148–1154.
- Al-Rawi, P. G., Smielewski, P. and Kirkpatrick, P. J. (2001) Evaluation of a near-infrared spectrometer (niro 300) for the detection of intracranial oxygenation changes in the adult head. *Stroke*, **32**, 2492–2500.
- Balfors, E. M. and Franklin, K. A. (1996) Impairment of cerebral perfusion during obstructive sleep apneas. *American Journal of Respiratory and Critical Care Medicine*, **150**, 1587–1591.
- Banaji, M., Tachtsidis, I., Delpy, D. and Baigent, S. (2005) A physiological model of cerebral blood flow control. *Math Biosci*, **194**, 125–173.
- Bandettini, P. A. and Wong, E. C. (1997) A hypercapnia-based normalization method for improved spatial localization of human brain activation with fmri. *NMR Biomed*, **10**, 197–203.
- Bannister, P. R. and Jenkinson, M. (2001) Robust affine motion correction in fmri time series. *NeuroImage*, **13**, 570.
- Bayliss, W. M. (1902) On the local reactions of the arterial wall to changes of internal pressure. *J Physiol*, **28**, 220–231.
- Bendat, J. S. and Piersol, A. G. (2000) *Random Data: Analysis and Measurement Procedures*. New York, NY, USA: John Wiley & Sons, Inc.
- Benders, M. J., Dorrepaal, C. A., van de Bor, M. and van Bel, F. (1995) Acute effects of indomethacin on cerebral hemodynamics and oxygenation. *Biol Neonate*, **68**, 91–99.
- Bereczki, D., Wei, L., Otsuka, T., Hans, F. J., Acuff, V., Patlak, C. and Fenstermacher, J. (1993) Hypercapnia slightly raises blood volume and sizably elevates flow velocity in brain microvessels. *Am J Physiol Heart Circ Physiol*, **264**, H1360–1369.
- Bhattacharyya, P. K. and Lowe, M. J. (2004) Cardiac-induced physiologic noise in tissue is a direct observation of cardiac-induced fluctuations. *Magn Reson Imaging*, **22**, 9–13.
- Bill, A. and Linder, J. (1976) Sympathetic control of cerebral blood flow in acute arterial hypertension. *Acta physiologica Scandinavica*, **96**, 114–121.
- Birch, A. A., Dirnhuber, M. J., Hartley-Davies, R., Iannotti, F. and Neil-Dwyer, G. (1995) Assessment of autoregulation by means of periodic changes in blood pressure. *Stroke*, **26**, 834–837.
- Birch, A. A. and Morris, S. L. (2003) Do the finapres and colin radial artery tonometer measure the same blood pressure changes following deflation of thigh cuffs? *Physiological measurement*, **24**, 653–660.
- Birch, A. A., Neil-Dwyer, G. and Murrills, A. J. (2002) The repeatability of cerebral autoregulation assessment using sinusoidal lower body negative pressure. *Physiol Meas*, **23**, 73–83.
- Birn, R. M., Diamond, J. B., Smith, M. A. and Bandettini, P. A. (2006) Separating respiratory-variation-related fluctuations from neuronal-activity-related fluctuations in fmri. *NeuroImage*, **31**, 1536–1548.
- Biswal, B., DeYoe, A. E. and Hyde, J. S. (1996) Reduction of physiological fluctuations in fmri using digital filters. *Magn Reson Med*, **35**, 107–113.
- Biswal, B., Yetkin, Z. F., Haughton, V. M. and Hyde, J. S. (1995) Functional connectivity in the motor cortex of resting human brain using echo-planar mri. *Magnetic Resonance in Medicine*, **34**, 537–541.
- Biswal, B. B., Van Kylen, J. and Hyde, J. S. (1997) Simultaneous assessment of flow and bold signals in resting-state functional connectivity maps. *NMR in Biomedicine*, **10**, 165–170.
- Bondar, R. L., Kassam, M. S., Stein, F., Dunphy, P. T. and Riedesel, M. L. (1994) Simultaneous transcranial doppler and arterial blood pressure response to lower body negative pressure. *J Clin Pharmacol*, **34**, 584–589.
- Bortfeld, H., Wruck, E. and Boas, D. A. (2007) Assessing infants' cortical response to speech using near-infrared spectroscopy. *NeuroImage*, **34**, 407–415.
- Bouma, G. J. and Muizelaar, J. P. (1990) Relationship between cardiac output and cerebral blood flow in patients with intact and with impaired autoregulation. *J Neurosurg*, **73**, 368–374.
- (1992) Cerebral blood flow, cerebral blood volume, and cerebrovascular reactivity after severe head injury. *J Neurotrauma*, **9 Suppl 1**.
- Bouma, G. J., Muizelaar, J. P., Bandoh, K. and Marmarou, A. (1992) Blood pressure and intracranial pressure-volume dynamics in severe head injury: relationship with cerebral blood flow. *J Neurosurg*, **77**, 15–19.
- Brooks, D. J., Redmond, S., Mathias, C. J., Bannister, R. and Symon, L. (1989) The effect of orthostatic hypotension on cerebral blood flow and middle cerebral artery velocity in autonomic failure, with observations on the action of ephedrine. *J Neurol Neurosurg Psychiatry*, **52**, 962–966.
- Buijs, J., Van Bel, F., Nandorff, A., Hardjowijono, R., Stijnen, T. and Ottenkamp, J. (1992) Cerebral blood flow pattern and autoregulation during open-heart surgery in infants and young children: a transcranial, doppler ultrasound study. *Crit Care Med*, **20**, 771–777.
- Busija, D. and Heistad, D. (1984) Factors involved in the physiological regulation of the cerebral circulation. *Reviews of Physiology, Biochemistry and Pharmacology*, **101**, 161–211.
- Buxton, R. B., Wong, E. C. and Frank, L. R. (1998) Dynamics of blood flow and oxygenation changes during brain activation: the balloon model. *Magn Reson Med*, **39**, 855–864.
- Byrne, E. A., Fleg, J. L., Vaitkevicius, P. V., Wright, J. and Porges, S. W. (1996) Role of aerobic capacity and body mass index in the age-associated decline in heart rate variability. *J Appl Physiol*, **81**, 743–750.
- Cencetti, S., Bandinelli, G. and Lagi, A. (1997) Effect of pco2 changes induced by head-upright tilt on transcranial doppler recordings. *Stroke*, **28**, 1195–1197.
- Cohen, E. R., Ugurbil, K. and Kim, S. G. (2002) Effect of basal conditions on the magnitude and dynamics of the blood oxygenation level-dependent fmri response. *J Cereb Blood Flow Metab*, **22**, 1042–1053.
- Cohen, M. A. and Taylor, A. J. (2002) Short-term cardiovascular oscillations in man: measuring and modelling the physiologies. *The Journal of Physiology*, **542**, 669–683.
- Colosimo, A., Giuliani, A., Mancini, A. M., Piccirillo, G. and Marigliano, V. (1997) Estimating a cardiac age by means of heart rate variability. *Am J Physiol Heart Circ Physiol*, **273**, H1841–1847.
- Cope, M. (1991) *The development of a near infrared spectroscopy system and its application for non invasive monitoring of cerebral blood and tissue oxygenation in the newborn infant*. Ph.D. thesis, University of London.
- Corfield, D. R., Murphy, K., Josephs, O., Adams, L. and Turner, R. (2001) Does hypercapnia-induced cerebral vasodilation modulate the hemodynamic response to neural activation? *Neuroimage*, **13**, 1207–1211.
- Czosnyka, M., Piechnik, S., Richards, H. K., Kirkpatrick, P., Smielewski, P. and Pickard, J. D. (1997) Contribution of mathematical modelling to the interpretation of bedside tests of cerebrovascular autoregulation. *J Neurol Neurosurg Psychiatry*, **63**, 721–31.

- Czosnyka, M., Smielewski, P., Kirkpatrick, P., Menon, D. K. and Pickard, J. D. (1996) Monitoring of cerebral autoregulation in head-injured patients. *Stroke*, **27**, 1829–1834.
- Czosnyka, M., Smielewski, P., Lavinio, A., Pickard, J. D. and Panerai, R. (2008) An assessment of dynamic autoregulation from spontaneous fluctuations of cerebral blood flow velocity: a comparison of two models, index of autoregulation and mean flow index. *Anesth Analg*, **106**.
- Czosnyka, M., Smielewski, P., Piechnik, S., Steiner, L. A. and Pickard, J. D. (2001) Cerebral autoregulation following head injury. *J Neurosurg*, **95**, 756–763.
- Daffertshofer, M., Diehl, R. R., Ziems, G. U. and Hennerici, M. (1991) Orthostatic changes of cerebral blood flow velocity in patients with autonomic dysfunction. *Journal of the neurological sciences*, **104**, 32–38.
- Dagli, M. S., Ingeholm, J. E. and Haxby, J. V. (1999) Localization of cardiac-induced signal change in fmri. *Neuroimage*, **9**, 407–415.
- De Luca, M., Beckmann, C. F., De Stefano, N., Matthews, P. M. and Smith, S. M. (2006) fmri resting state networks define distinct modes of long-distance interactions in the human brain. *NeuroImage*, **29**, 1359–1367.
- deBoer, R. W., Karemaker, J. M. and Strackee, J. (1987) Hemodynamic fluctuations and baroreflex sensitivity in humans: a beat-to-beat model. *Am J Physiol*, **253**.
- Delpy, D. T. and Cope, M. (1997) Quantification in tissue near-infrared spectroscopy. *Philosophical Transactions of the Royal Society of London*, **B**, **352**, 649–659.
- Diehl, R. R., Diehl, B., Sitzer, M. and Hennerici, M. (1991) Spontaneous oscillations in cerebral blood flow velocity in normal humans and in patients with carotid artery disease. *Neurosci Lett*, **127**, 5–8.
- Diehl, R. R., Linden, D., Lcke, D. and Berlit, P. (1995) Phase relationship between cerebral blood flow velocity and blood pressure. a clinical test of autoregulation. *Stroke*, **26**, 1801–1804.
- Duncan, A., Meek, J. H., Clemence, M., Elwell, C. E., Tyszczuk, L., Cope, M. and Delpy, D. T. (1995) Optical pathlength measurements on adult head, calf and forearm and the head of the newborn infant using phase resolved optical spectroscopy. *Phys Med Biol*, **40**, 295–304.
- Dutton, K., Thompson, S. and Barraclough, B. (1997) *The Art of Control Engineering*. Boston, MA, USA: Addison-Wesley Longman Publishing Co., Inc.
- Edvinsson, L., Mackenzie, E. T. and McCulloch, J. (1992) *Cerebral Blood Flow and Metabolism*. Raven Pr.
- Edvinsson, L., Owman, C. and Siesjö, B. (1976) Physiological role of cerebrovascular sympathetic nerves in the autoregulation of cerebral blood flow. *Brain research*, **117**, 519–523.
- Edwards, M. R., Topor, Z. L. and Hughson, R. L. (2003) A new two-breath technique for extracting the cerebrovascular response to arterial carbon dioxide. *Am J Physiol Regul Integr Comp Physiol*, **284**, R853–859.
- Ellingsen, I., Hauge, A., Nicolaysen, G., Thoresen, M. and Walle, L. (1987) Changes in human cerebral blood flow due to step changes in pao₂ and paco₂. *Acta Physiol Scand*, **129**, 157–163.
- Elwell, C. E. (1995) *A practical users guide to near infrared spectroscopy*. London, UK: Hamamatsu Photonics KK UCL Reprographics.
- Elwell, C. E., Cope, M., Edwards, A. D., Wyatt, J. S., Delpy, D. T. and Reynolds, E. O. (1994) Quantification of adult cerebral hemodynamics by near-infrared spectroscopy. *J Appl Physiol*, **77**, 2753–2760.
- Elwell, C. E., Springett, R., Hillman, E. and Delpy, D. T. (1999) Oscillations in cerebral haemodynamics. implications for functional activation studies. *Adv Exp Med Biol*, **471**, 57–65.
- Finger, S. (1999) *Minds behind the Brain: A History of the Pioneers and Their Discoveries*. Oxford University Press, USA.
- Fisher, N. I. (1995) *Statistical Analysis of Circular Data*. Cambridge University Press.
- Friston, K. J., Mechelli, A., Turner, R. and Price, C. J. (2000) Nonlinear responses in fmri: the balloon model, volterra kernels, and other hemodynamics. *Neuroimage*, **12**, 466–477.
- Furchgott, R. F. (1984) The role of endothelium in the responses of vascular smooth muscle to drugs. *Annual Review of Pharmacology and Toxicology*, **24**, 175–197.
- Gabor, D. (1946) Theory of communication. *Journal of the IEE (London)*, **93**, 429–457.
- Garnham, J., Panerai, R. B., Naylor, A. R. and Evans, D. H. (1999) Cerebrovascular response to dynamic changes in pco₂. *Cerebrovasc Dis*, **9**, 146–151.
- Giller, C. A. (1990) The frequency-dependent behavior of cerebral autoregulation. *Neurosurgery*, **27**, 362–368.
- Giller, C. A., Bowman, G., Dyer, H., Mootz, L. and Krippner, W. (1993) Cerebral arterial diameters during changes in blood pressure and carbon dioxide during craniotomy. *Neurosurgery*, **32**.
- Giller, C. A. and Mueller, M. (2003) Linearity and non-linearity in cerebral hemodynamics. *Med Eng Phys*, **25**, 633–646.
- Goldman, R. I., Stern, J. M., Engel, J. and Cohen, M. S. (2002) Simultaneous eeg and fmri of the alpha rhythm. *Neuroreport*, **13**, 2487–2492.
- Goulden, C. H. (1959) *Methods of statistical analysis (Wiley publications in statistics)*. Wiley.
- Goupillaud, P., Grossmann, A. and Morlet, J. (1984) Cycle-octave and related transforms in seismic signal analysis. *Geoexploration*, **23**, 85–102.
- Greisen, G., Johansen, K., Ellison, P. H., Fredriksen, P. S., Mali, J. and Friis-Hansen, B. (1984) Cerebral blood flow in the newborn infant: comparison of doppler ultrasound and 133xenon clearance. *J Pediatr*, **104**, 411–418.
- Grinsted, A., Moore, J. C. and Jevrejeva, S. (2004) Application of the cross wavelet transform and wavelet coherence to geophysical time series. *Nonlinear Processes in Geophysics*, **11**, 561–566.
- Grubb, R. L., Raichle, M. E., Eichling, J. O. and Ter-Pogossian, M. M. (1974) The effects of changes in paco₂ on cerebral blood volume, blood flow, and vascular mean transit time. *Stroke*, **5**, 630–639.
- Guyton, A. C. (1980) *Arterial pressure and hypertension*. Philadelphia: Saunders.
- Haddock, R. E. and Hill, C. E. (2005) Rhythmicity in arterial smooth muscle. *The Journal of Physiology*, **566**, 645–656.
- Hansen, N. B., Stonestreet, B. S., Rosenkrantz, T. S. and Oh, W. (1983) Validity of doppler measurements of anterior cerebral artery blood flow velocity: Correlation with brain blood flow in piglets. *Pediatrics*, **72**, 526–531.
- Harms, M. P., Colier, W. N., Wieling, W., Lenders, J. W., Secher, N. H. and van Lieshout, J. J. (2000) Orthostatic tolerance, cerebral oxygenation, and blood velocity in humans with sympathetic failure. *Stroke*, **31**, 1608–1614.
- Harper, M. A. and Jennett, S. (1990) *Cerebral Blood Flow and Metabolism (Physiological Society Study Guide)*. Manchester Univ Pr.
- Hoge, R. D., Atkinson, J., Gill, B., Crelier, G. R., Marrett, S. and Pike, B. G. (1999a) Investigation of bold signal dependence on cerebral blood flow and oxygen consumption: The deoxyhemoglobin dilution model. *Magnetic Resonance in Medicine*, **42**, 849–863.
- (1999b) Linear coupling between cerebral blood flow and oxygen consumption in activated human cortex. *PNAS*, **96**, 9403–9408.
- Hu, H. H., Kuo, T. B., Wong, W. J., Luk, Y. O., Chern, C. M., Hsu, L. C. and Sheng, W. Y. (1999) Transfer function analysis of cerebral hemodynamics in patients with carotid stenosis. *Journal of cerebral blood flow and metabolism : official journal of the International Society of Cerebral Blood Flow and Metabolism*, **19**, 460–465.
- Hudetz, A. G., Biswal, B. B., Shen, H., Lauer, K. K. and Kampine, J. P. (1998) Spontaneous fluctuations in cerebral oxygen supply. an introduction. *Adv Exp Med Biol*, **454**, 551–559.
- Hudetz, A. G., Roman, R. J. and Harder, D. R. (1992) Spontaneous flow oscillations in the cerebral cortex during acute changes in mean arterial pressure. *J Cereb Blood Flow Metab*, **12**, 491–499.
- Huppert, T. J., Hoge, R. D., Diamond, S. G., Franceschini, M. A. and Boas, D. A. (2005) A temporal comparison of bold, asl, and nirs hemodynamic responses to motor stimuli in adult humans. *Neuroimage*, **29**, 368–382.
- Ingvar, D. H. and Lassen, N. A. (1965) Methods for cerebral blood flow measurements in man. *Br J Anaesth*, **37**, 216–224.
- Innes, J. A., De Cort, S. C., Kox, W. and Guz, A. (1993) Within-breath modulation of left ventricular function during normal breathing and positive-pressure ventilation in man. *J Physiol*, **460**, 487–502.
- Jansen, R. W., Lenders, J. W., Thien, T. and Hoefnagels, W. H. (1989) The influence of age and blood pressure on the hemodynamic and humoral response to head-up tilt. *J Am Geriatr Soc*, **37**, 528–532.
- Jenkinson, M. and Smith, S. (2001) A global optimisation method for robust affine registration of brain images. *Med Image Anal*, **5**, 143–156.

- Jennings, R. J. (2003) Autoregulation of blood pressure and thought: Preliminary results of an application of brain imaging to psychosomatic medicine. *Psychosom Med*, **65**, 384–395.
- Jöbsis, F. F. (1977) Noninvasive, infrared monitoring of cerebral and myocardial oxygen sufficiency and circulatory parameters. *Science*, **198**, 1264–1267.
- Jorch, G. and Jorch, N. (1987) Failure of autoregulation of cerebral blood flow in neonates studied by pulsed doppler ultrasound of the internal carotid artery. *European Journal of Pediatrics*, **146**, 468–472.
- Jünger, E. C., Newell, D. W., Grant, G. A., Avellino, A. M., Ghatan, S., Douville, C. M., Lam, A. M., Aaslid, R. and Winn, H. R. (1997) Cerebral autoregulation following minor head injury. *Journal of neurosurgery*, **86**, 425–432.
- Jrgensen, L. G., Perko, M., Perko, G. and Secher, N. H. (1993) Middle cerebral artery velocity during head-up tilt induced hypovolaemic shock in humans. *Clin Physiol*, **13**, 323–336.
- Kastrup, A., Krüger, G., Glover, G. H., Neumann-Haefelin, T. and Moseley, M. E. (1999) Regional variability of cerebral blood oxygenation response to hypercapnia. *Neuroimage*, **10**, 675–681.
- Katura, T., Tanaka, N., Obata, A., Sato, H. and Maki, A. (2006) Quantitative evaluation of interrelations between spontaneous low-frequency oscillations in cerebral hemodynamics and systemic cardiovascular dynamics. *NeuroImage*, **31**.
- Kawaguchi, T., Uyama, O., Konishi, M., Nishiyama, T. and Iida, T. (2001) Orthostatic hypotension in elderly persons during passive standing: a comparison with young persons. *J Gerontol A Biol Sci Med Sci*, **56**.
- Kemna, L. J. and Posse, S. (2001) Effect of respiratory co2 changes on the temporal dynamics of the hemodynamic response in functional mr imaging. *Neuroimage*, **14**, 642–649.
- Kety, S. S. and Schmidt, C. F. (1948) The effects of altered arterial tensions of carbon dioxide and oxygen on cerebral blood flow and cerebral oxygen consumption of normal young men. *The Journal of clinical investigation*, **27**, 484–492.
- Kirkpatrick, P. J., Smielewski, P., Al-Rawi, P. and Czosnyka, M. (1998) Resolving extra- and intracranial signal changes during adult near infrared spectroscopy. *Neuro Res*, **20 Suppl 1**.
- Krüger, G. and Glover, G. H. (2001) Physiological noise in oxygenation-sensitive magnetic resonance imaging. *Magnetic Resonance in Medicine*, **46**, 631–637.
- Krüger, G., Kastrup, A. and Glover, G. H. (2001) Neuroimaging at 1.5 t and 3.0 t: Comparison of oxygenation-sensitive magnetic resonance imaging. *Magnetic Resonance in Medicine*, **45**, 595–604.
- Kuschinsky, W. and Wahl, M. (1978) Local chemical and neurogenic regulation of cerebral vascular resistance. *Physiol Rev*, **58**, 656–689.
- Kwong, K. K., Belliveau, J. W., Chesler, D. A., Goldberg, I. E., Weisskoff, R. M., Poncelet, B. P., Kennedy, D. N., Hoppel, B. E., Cohen, M. S. and Turner, R. (1992) Dynamic magnetic resonance imaging of human brain activity during primary sensory stimulation. *Proc Natl Acad Sci U S A*, **89**, 5675–5679.
- Lagi, A., Bacalli, S., Cencetti, S., Paggetti, C. and Colzi, L. (1994) Cerebral autoregulation in orthostatic hypotension. a transcranial doppler study. *Stroke*, **25**, 1771–1775.
- Laitinen, T., Niskanen, L., Geelen, G., Lansimies, E. and Hartikainen, J. (2004) Age dependency of cardiovascular autonomic responses to head-up tilt in healthy subjects. *J Appl Physiol*, **96**, 2333–2340.
- Larsen, F. S., Olsen, K. S., Hansen, B. A., Paulson, O. B. and Knudsen, G. M. (1994) Transcranial doppler is valid for determination of the lower limit of cerebral blood flow autoregulation. *Stroke*, **25**, 1985–1988.
- Lassen, N. A. (1959) Cerebral blood flow and oxygen consumption in man. *Physiol Rev*, **39**, 183–238.
- (1974) Control of cerebral circulation in health and disease. *Circulation Research*, **34**, 749–760.
- (1980) Citation classic - cerebral blood-flow and oxygen-consumption in man. *Current Contents in Clinical Practice*, **1012**.
- Latka, M., Turalska, M., Glaubic-Latka, M., Kolodziej, W., Latka, D. and West, B. J. J. (2005) Phase dynamics in cerebral autoregulation. *Am J Physiol Heart Circ Physiol*.
- Le Van Quyen, M., Foucher, J., Lachaux, J., Rodriguez, E., Lutz, A., Martinerie, J. and Varela, F. J. (2001) Comparison of hilbert transform and wavelet methods for the analysis of neuronal synchrony. *J Neurosci Methods*, **111**, 83–98.
- Levine, B. D., Giller, C. A., Lane, L. D., Buckley, J. C. and Blomqvist, C. G. (1994) Cerebral versus systemic hemodynamics during graded orthostatic stress in humans. *Circulation*, **90**, 298–306.
- van Lieshout, J. J. and Secher, N. H. (2008) Point:counterpoint: Sympathetic activity does/does not influence cerebral blood flow. *J Appl Physiol*, **105**, 1364–1366.
- Linden, D. and Diehl, R. (1996) Estimation of baroreflex sensitivity using transfer function analysis: normal values and theoretical considerations. *Clinical Autonomic Research*, **6**, 157–161.
- Lipsitz, L. A. (1989) Orthostatic hypotension in the elderly. *N Engl J Med*, **321**, 952–957.
- Liu, H., Rainey, C., Lauer, K. K., Piacentine, L., Bloom, A., Risinger, R., Ward, B. D., Stein, E. and Li, S. J. (2006) Peripheral blood pressure changes induced by dobutamine do not alter bold signals in the human brain. *Neuroimage*, **30**, 745–752.
- Liu, Y., Birch, A. A. and Allen, R. (2003) Dynamic cerebral autoregulation assessment using an arx model: comparative study using step response and phase shift analysis. *Med Eng Phys*, **25**, 647–653.
- Ljung, L. (1998) *System Identification: Theory for the User (2nd Edition)*. Prentice Hall PTR.
- Lodi, C. A., Ter Minassian, A., Beydon, L. and Ursino, M. (1998) Modeling cerebral autoregulation and co2 reactivity in patients with severe head injury. *Am J Physiol*, **274**.
- Lowe, M. J., Mock, B. J. and Sorenson, J. A. (1998) Functional connectivity in single and multislice echoplanar imaging using resting-state fluctuations. *NeuroImage*, **7**, 119–132.
- Lu, K., Clark, J. W., Ghorbel, F. H., Robertson, C. S., Ware, D. L., Zwischenberger, J. B. and Bidani, A. (2004) Cerebral autoregulation and gas exchange studied using a human cardiopulmonary model. *Am J Physiol Heart Circ Physiol*, **286**, H584–H601.
- Lundar, T., Lindegaard, K. F., Frysaker, T., Aaslid, R., Grip, A. and Nornes, H. (1985) Dissociation between cerebral autoregulation and carbon dioxide reactivity during nonpulsatile cardiopulmonary bypass. *Ann Thorac Surg*, **40**, 582–587.
- Lundberg, N. (1960) Continuous recording and control of ventricular fluid pressure in neurosurgical practice. *Acta Psychiatr Scand Suppl*, **36**, 1–193.
- MacIntosh, B. J., Klassen, L. M. and Menon, R. S. (2003) Transient hemodynamics during a breath hold challenge in a two part functional imaging study with simultaneous near-infrared spectroscopy in adult humans. *Neuroimage*, **20**, 1246–1252.
- Mallat, S. (1999) *A Wavelet Tour of Signal Processing, Second Edition (Wavelet Analysis & Its Applications)*. Academic Press.
- Mayer, S. (1876) Studien zur physiologie des herzens und der blutgefäße 6. abhandlung: Über spontane blutdruckschwankungen. *Sitzungsberichte Akademie der Wissenschaften in Wien. Mathematisch-naturwissenschaftliche Classe, Anatomie*, **74**, 281–307.
- Mayhew, J. E., Askew, S., Zheng, Y., Porritt, J., Westby, G. W., Redgrave, P., Rector, D. M. and Harper, R. M. (1996) Cerebral vasomotion: a 0.1-hz oscillation in reflected light imaging of neural activity. *Neuroimage*, **4**, 183–193.
- McCulloch, J. and Edvinsson, L. (1984) Cerebrovascular smooth muscle reactivity: a critical appraisal of in vitro and in situ techniques. *Journal of cerebral blood flow and metabolism : official journal of the International Society of Cerebral Blood Flow and Metabolism*, **4**, 129–139.
- Mepherson, R. W., Koehler, R. C. and Traystman, R. J. (1988) Effect of jugular venous pressure on cerebral autoregulation in dogs. *Am J Physiol Heart Circ Physiol*, **255**, H1516–1524.
- Mehagnoul-Schipper, D. J., Colier, W. N. and Jansen, R. W. (2001) Reproducibility of orthostatic changes in cerebral oxygenation in healthy subjects aged 70 years or older. *Clin Physiol*, **21**, 77–84.
- Mehagnoul-Schipper, J. D., Vloet, L. C., Colier, W. N., Hoefnagels, W. H. and Jansen, R. W. (2000) Cerebral oxygenation declines in healthy elderly subjects in response to assuming the upright position. *Stroke*, **31**, 1615–1620.
- Menke, J., Michel, E., Rabe, H., Bresser, B. W., Grohs, B., Schmitt, R. M. and Jorch, G. (1993) Simultaneous influence of blood pressure, pco2, and po2 on cerebral blood flow velocity in preterm infants of less than 33 weeks' gestation. *Pediatr Res*, **34**, 173–177.
- Mitsis, G. D., Ainslie, P. N., Poulin, M. J., Robbins, P. A. and Marmarelis, V. Z. (2004a) Nonlinear modeling of the dynamic effects of arterial pressure and blood gas variations on cerebral blood flow in healthy humans. *Adv Exp Med Biol*, **551**, 259–265.

- Mitsis, G. D., Poulin, M. J., Robbins, P. A. and Marmarelis, V. Z. (2004b) Nonlinear modeling of the dynamic effects of arterial pressure and CO_2 variations on cerebral blood flow in healthy humans. *IEEE Trans Biomed Eng*, **51**, 1932–1943.
- Mitsis, G. D., Zhang, R., Levine, B. D. and Marmarelis, V. Z. (2002) Modeling of nonlinear physiological systems with fast and slow dynamics. ii. application to cerebral autoregulation. *Ann Biomed Eng*, **30**, 555–565.
- Mizuno-Matsumoto, Y., Ukai, S., Ishii, R., Date, S., Kaishima, T., Shinosaki, K., Shimajo, S., Takeda, M., Tamura, S. and Inouye, T. (2005) Wavelet-crosscorrelation analysis: Non-stationary analysis of neurophysiological signals. *Brain Topogr*, **17**, 237–252.
- Modarreszadeh, M. and Bruce, E. N. (1994) Ventilatory variability induced by spontaneous variations of paco_2 in humans. *J Appl Physiol*, **76**, 2765–2775.
- Molhoek, G. P., Wesseling, K. H., Settels, J. J., van Vollenhoven, E., Weeda, H. W., de Wit, B. and Arntzenius, A. C. (1984) Evaluation of the penáz servo-plethysmo-manometer for the continuous, non-invasive measurement of finger blood pressure. *Basic research in cardiology*, **79**, 598–609.
- Moosmann, M., Ritter, P., Krastel, I., Brink, A., Thees, S., Blankenburg, F., Taskin, B., Obrig, H. and Villringer, A. (2003) Correlates of alpha rhythm in functional magnetic resonance imaging and near infrared spectroscopy. *Neuroimage*, **20**, 145–158.
- Morita, Y., Hardebo, J. E. and Bouskela, E. (1994) Influence of cerebrovascular parasympathetic nerves on resting cerebral blood flow, spontaneous vasomotion, autoregulation, hypercapnic vasodilation and sympathetic vasoconstriction. *Journal of the autonomic nervous system*, **49 Suppl**.
- Muizelaar, J. P., Lutz, H. A. and Becker, D. P. (1984) Effect of mannitol on icp and cbf and correlation with pressure autoregulation in severely head-injured patients. *J Neurosurg*, **61**, 700–706.
- de Mul, F. F., Morales, F., Smit, A. J. and Graaff, R. (2005) A model for post-occlusive reactive hyperemia as measured with laser-doppler perfusion monitoring. *IEEE Trans Biomed Eng*, **52**, 184–190.
- Newell, D. W., Weber, J. P., Watson, R., Aaslid, R. and Winn, H. R. (1996) Effect of transient moderate hyperventilation on dynamic cerebral autoregulation after severe head injury. *Neurosurgery*, **39**.
- Nilsson, H. and Aalkjaer, C. (2003) Vasomotion: mechanisms and physiological importance. *Mol Interv*, **3**.
- Nollert, G., Mohnle, P., Tassani-Prell, P. and Reichart, B. (1995) Determinants of cerebral oxygenation during cardiac surgery. *Circulation*, **92**, 327–333.
- Nolte, J. (2002) *The Human Brain: An Introduction to Its Functional Anatomy*. Mosby.
- Obata, T., Liu, T. T., Miller, K. L., Luh, W. M., Wong, E. C., Frank, L. R. and Buxton, R. B. (2004) Discrepancies between bold and flow dynamics in primary and supplementary motor areas: application of the balloon model to the interpretation of bold transients. *Neuroimage*, **21**, 144–153.
- Obrig, H., Neufang, M., Wenzel, R., Kohl, M., Steinbrink, J., Einhupl, K. and Villringer, A. (2000) Spontaneous low frequency oscillations of cerebral hemodynamics and metabolism in human adults. *Neuroimage*, **12**, 623–639.
- Oehm, E., Reinhard, M., Keck, C., Els, T., Spreer, J. and Hetzel, A. (2003) Impaired dynamic cerebral autoregulation in eclampsia. *Ultrasound Obstet Gynecol*, **22**, 395–398.
- Ogawa, S., Lee, T.-M., Nayak, A. S. and Glynn, P. (1990) Oxygenation-sensitive contrast in magnetic resonance image of rodent brain at high magnetic fields. *Magnetic Resonance in Medicine*, **14**, 68–78.
- Oka, H., Mochio, S., Yoshioka, M., Morita, M. and Inoue, K. (2003) Evaluation of baroreflex sensitivity by the sequence method using blood pressure oscillations and r-r interval changes during deep respiration. *Eur Neurol*, **50**, 230–243.
- Olesen, J. (1972) The effect of intracarotid epinephrine, norepinephrine, and angiotensin on the regional cerebral blood flow in man. *Neurology*, **22**, 978–987.
- Olhede, S. and Walden, A. T. (2004) The hilbert spectrum via wavelet projections. *Proceedings of the Royal Society A: Mathematical, Physical and Engineering Sciences*, **460**, 955–975.
- Olsen, K. S., Svendsen, L. B. and Larsen, F. S. (1996) Validation of transcranial near-infrared spectroscopy for evaluation of cerebral blood flow autoregulation. *J Neurosurg Anesthesiol*, **8**, 280–285.
- Panerai, R.B., Sammons, E.L., Smith, S.M., Rathbone, W.E., Bentley, S., Potter, J.F., Samani and N.J. (2008) Continuous estimates of dynamic cerebral autoregulation: influence of non-invasive arterial blood pressure measurements. *Physiological Measurement*, **29**, 497–513.
- Panerai, R. (2003) The critical closing pressure of the cerebral circulation. *Med Eng Phys*, **25**, 621–32.
- Panerai, R., Rennie, J., Kelsall, A. and Evans, D. (1998) Frequency-domain analysis of cerebral autoregulation from spontaneous fluctuations in arterial blood pressure. *Medical and Biological Engineering and Computing*, **36**, 315–322.
- Panerai, R. B. (1998) Assessment of cerebral pressure autoregulation in humans - a review of measurement methods. *Physiological Measurement*, **19**, 305–338.
- Panerai, R. B., Dawson, S. L., Eames, P. J. and Potter, J. F. (2001) Cerebral blood flow velocity response to induced and spontaneous sudden changes in arterial blood pressure. *Am J Physiol Heart Circ Physiol*, **280**, 2162–2174.
- Panerai, R. B., Dawson, S. L. and Potter, J. F. (1999) Linear and nonlinear analysis of human dynamic cerebral autoregulation. *Am J Physiol*, **277**, 1089–1099.
- Panerai, R. B., Eames, P. J. and Potter, J. F. (2006) Multiple coherence of cerebral blood flow velocity in humans. *Am J Physiol Heart Circ Physiol*, **291**.
- Panerai, R. B., Hudson, V., Fan, L., Mahony, P., Yeoman, P. M., Hope, T. and Evans, D. H. (2002) Assessment of dynamic cerebral autoregulation based on spontaneous fluctuations in arterial blood pressure and intracranial pressure. *Physiol Meas*, **23**, 59–72.
- Panerai, R. B., James, M. A. and Potter, J. F. (1997) Impulse response analysis of baroreceptor sensitivity. *Am J Physiol Heart Circ Physiol*, **272**, H1866–1875.
- Panerai, R. B., Kelsall, A. W., Rennie, J. M. and Evans, D. H. (1995a) Cerebral autoregulation dynamics in premature newborns. *Stroke*, **26**, 74–80.
- (1995b) Estimation of critical closing pressure in the cerebral circulation of newborns. *Neuropediatrics*, **26**, 168–173.
- (1996) Analysis of cerebral blood flow autoregulation in neonates. *IEEE transactions on bio-medical engineering*, **43**, 779–788.
- Panerai, R. B., Moody, M., Eames, P. J. and Potter, J. F. (2005) Cerebral blood flow velocity during mental activation: interpretation with different models of the passive pressure-velocity relationship. *J Appl Physiol*, **99**, 2352–2362.
- Panerai, R. B., Simpson, D. M., Deverson, S. T., Mahony, P., Hayes, P. and Evans, D. H. (2000) Multivariate dynamic analysis of cerebral blood flow regulation in humans. *IEEE Trans Biomed Eng*, **47**, 419–423.
- Parati, G., Casadei, R., Groppelli, A., Di Rienzo, M. and Mancia, G. (1989) Comparison of finger and intra-arterial blood pressure monitoring at rest and during laboratory testing. *Hypertension*, **13**, 647–655.
- Paulson, O. B., Strandgaard, S. and Edvinsson, L. (1990) Cerebral autoregulation. *Cerebrovasc Brain Metab Rev*, **2**, 161–192.
- Paulson, O. B., Waldemar, G., Andersen, A. R., Barry, D. I., Pedersen, E. V., Schmidt, J. F. and Vorstrup, S. (1988) Role of angiotensin in autoregulation of cerebral blood flow. *Circulation*, **77**.
- Payne, S. J. (2006) A model of the interaction between autoregulation and neural activation in the brain. *Mathematical Biosciences*, **204**, 260–281.
- Payne, S. J. and Tarassenko, L. (2006) Combined transfer function analysis and modelling of cerebral autoregulation. *Annals of Biomedical Engineering*, **34**, 847–858.
- Peng, T., Ainslie, P. N., Cotter, J. D., Murrell, C., Thomas, K., Williams, M. J., George, K., Shave, R., Rowley, A. B. and Payne, S. J. (2008a) The effects of age on the spontaneous low-frequency oscillations in cerebral and systemic cardiovascular dynamics. *Physiological Measurement*, **29**, 1055–1069.
- Peng, T., Rowley, A. B., Ainslie, P. N., Poulin, M. J. and Payne, S. J. (2007) Multivariate system identification for cerebral autoregulation. *Ann Biomed Eng*.
- (2008b) Wavelet phase synchronization analysis of cerebral blood flow autoregulation. *Accepted by IEEE transaction on Biomedical Engineering*.
- Percival, D. B. and Walden, A. T. (2000) *Wavelet Methods for Time Series Analysis (Cambridge Series in Statistical and Probabilistic Mathematics)*. Cambridge University Press.
- Perreault, E. J., Kirsch, R. F. and Acosta, A. M. (1999) Multiple-input, multiple-output system identification for characterization of limb stiffness dynamics. *Biol Cybern*, **80**, 327–337.
- Posse, S., Kemna, L. J., Elghahwagi, B., Wiese, S. and Kiselev, V. G. (2001) Effect of graded hypo- and hypercapnia on fmri contrast in visual cortex: quantification of $t^{(*)}2$ changes by multiecho epi. *Magn Reson Med*, **46**, 264–271.
- Posse, S., Olthoff, U., Weckesser, M., Jancke, L., Muller-Gartner, H. W. and Dager, S. R. (1997) Regional dynamic signal changes during controlled hyperventilation assessed with blood oxygen level-dependent functional mr imaging. *AJNR Am J Neuroradiol*, **18**, 1763–1770.

- Poulin, M. J., Liang, P. J. and Robbins, P. A. (1996) Dynamics of the cerebral blood flow response to step changes in end-tidal pco₂ and po₂ in humans. *J Appl Physiol*, **81**, 1084–1095.
- Poulin, M. J., Liang, P.-J. and Robbins, P. A. (1998) Fast and slow components of cerebral blood flow response to step decreases in end-tidal pco₂ in humans. *J Appl Physiol*, **85**, 388–397.
- Poulin, M. J. and Robbins, P. A. (1996) Indexes of flow and cross-sectional area of the middle cerebral artery using doppler ultrasound during hypoxia and hypercapnia in humans. *Stroke*, **27**, 2244–2250.
- Preiss, G. and Polosa, C. (1974) Patterns of sympathetic neuron activity associated with mayer waves. *Am J Physiol*, **226**, 724–730.
- Priebe, H.-J. (1999) *Cardiovascular Physiology: Fundamentals of Anaesthesia and Acute Medicine*. Wiley-Blackwell.
- Pryds, O., Greisen, G., Lou, H. and Friis-Hansen, B. (1990) Vasoparalysis associated with brain damage in asphyxiated term infants. *J Pediatr*, **117**, 119–125.
- Purves, D., Augustine, G. J., Fitzpatrick, D. and Katz, L. C. (1997) *Neuroscience*. Sinauer Associates Inc.
- Raiha, I., Luutonen, S., Piha, J., Seppanen, A., Toikka, T. and Sourander, L. (1995) Prevalence, predisposing factors, and prognostic importance of postural hypotension. *Arch Intern Med*, **155**, 930–935.
- Reinhard, M., Hetzel, A., Lauk, M. and Lücking, C. H. (2001) Evaluation of impaired dynamic cerebral autoregulation by the mueller manoeuvre. *Clin Physiol*, **21**, 229–237.
- Reinhard, M., Müller, T., Guschlbauer, B., Timmer, J. and Hetzel, A. (2003a) Dynamic cerebral autoregulation and collateral flow patterns in patients with severe carotid stenosis or occlusion. *Ultrasound Med Biol*, **29**, 1105–1113.
- Reinhard, M., Roth, M., Guschlbauer, B., Harloff, A., Timmer, J., Czosnyka, M. and Hetzel, A. (2005) Dynamic cerebral autoregulation in acute ischemic stroke assessed from spontaneous blood pressure fluctuations. *Stroke*, **36**, 1684–1689.
- Reinhard, M., Roth, M., Müller, T., Czosnyka, M., Timmer, J. and Hetzel, A. (2003b) Cerebral autoregulation in carotid artery occlusive disease assessed from spontaneous blood pressure fluctuations by the correlation coefficient index. *Stroke*, **34**, 2138–2144.
- Reivich, M. (1964) Arterial pco₂ and cerebral hemodynamics. *Am J Physiol*, **206**, 25–35.
- Renkin, E. M. and Michel, C. C. (1983) *Handbook of Physiology: Section 2: The Cardiovascular System Volume IV, Parts 1 & 2: Microcirculation (Handbook of Physiology Revised Edition)*. An American Physiological Society Book.
- Rice, J. (1995) *Mathematical Statistics and Data Analysis (Statistics)*. Belmont, Calif: Duxbury Press.
- Robbins, P. A., Conway, J., Cunningham, D. A., Khamnei, S. and Paterson, D. J. (1990) A comparison of indirect methods for continuous estimation of arterial pco₂ in men. *J Appl Physiol*, **68**, 1727–1731.
- Rosenblum, W. I. (1995) Autoregulatory plateau: does it exist? *Journal of cerebral blood flow and metabolism: official journal of the International Society of Cerebral Blood Flow and Metabolism*, **15**, 174–177.
- Rosenblum, W. I., Nelson, G. H. and Povlishock, J. T. (1987) Laser-induced endothelial damage inhibits endothelium-dependent relaxation in the cerebral microcirculation of the mouse. *Circ Res*, **60**, 169–176.
- Rostrup, E., Law, I., Blinkenberg, M., Larsson, H. B. W., Born, A. P., Holm, S. and Paulson, O. B. (2000) Regional differences in the cbf and bold responses to hypercapnia: A combined pet and fmri study. *NeuroImage*, **11**, 87–97.
- Rowley, A. B. (2008) *Signal processing methods for cerebral autoregulation*. Ph.D. thesis, University of Oxford.
- Rowley, A. B., Payne, S. J., Tachtsidis, I., Ebden, M. J., Whiteley, J. P., Gavaghan, D. J., Tarassenko, L., Smith, M., Elwell, C. E. and Delpy, D. T. (2007) Synchronization between arterial blood pressure and cerebral oxyhaemoglobin concentration investigated by wavelet cross-correlation. *Physiological Measurement*, **28**, 161–173.
- Rubanyi, G. M., Romero, J. C. and Vanhoutte, P. M. (1986) Flow-induced release of endothelium-derived relaxing factor. *The American journal of physiology*, **250**.
- Schimpfenig, T. and Lindsey, L. (2000) *Nols Wilderness First Aid (Nols Library)*. Stackpole Books.
- Schmidt, J. F., Waldemar, G., Vorstrup, S., Andersen, A. R., Gjerris, F. and Paulson, O. B. (1990) Computerized analysis of cerebral blood flow autoregulation in humans: validation of a method for pharmacologic studies. *J Cardiovasc Pharmacol*, **15**, 983–988.
- Schroeter, M. L., Kupka, T., Mildner, T., Uluda, K. and von Cramon, D. Y. (2006) Investigating the post-stimulus undershoot of the bold signal—a simultaneous fmri and fnirs study. *NeuroImage*, **30**, 349–358.
- Schroeter, M. L., Schmiedel, O. and von Cramon, D. Y. (2004) Spontaneous low-frequency oscillations decline in the aging brain. *J Cereb Blood Flow Metab*, **24**, 1183–1191.
- Selesnick, I. W. (2002) The design of approximate hilbert transform pairs of wavelet bases. *Signal Processing, IEEE Transactions on [see also Acoustics, Speech, and Signal Processing, IEEE Transactions on]*, **50**, 1144–1152.
- Selesnick, I. W., Baraniuk, R. G. and Kingsbury, N. C. (2005) The dual-tree complex wavelet transform. *Signal Processing Magazine, IEEE*, **22**, 123–151.
- Shmueli, K., van Gelderen, P., de Zwart, J. A., Horowitz, S. G., Fukunaga, M., Jansma, M. J. and Duyn, J. H. (2007) Low-frequency fluctuations in the cardiac rate as a source of variance in the resting-state fmri bold signal. *NeuroImage*, **38**, 306–320.
- Siesjo, B. K. (1978) *Brain Energy Metabolism*. John Wiley and Sons Ltd.
- Smielewski, P., Czosnyka, M., Kirkpatrick, P., Mceroy, H., Rutkowska, H. and Pickard, J. D. (1996) Assessment of cerebral autoregulation using carotid artery compression. *Stroke*, **27**, 2197–2203.
- Smith, J. J., Hughes, C. V., Ptacin, M. J., Barney, J. A., Tristani, F. E. and Ebert, T. J. (1987) The effect of age on hemodynamic response to graded postural stress in normal men. *J Gerontol*, **42**, 406–411.
- Smith, S., Bannister, P. R., Beckmann, C., Brady, J. M., Clare, S., Flitney, D., Hansen, P., Jenkinson, M., Leibold, D., Ripley, B., Woolrich, M. and Zhang, Y. (2001) Fsl: New tools for functional and structural brain image analysis. *NeuroImage*, **13**, S249.
- Steiger, H. J., Aaslid, R., Stooss, R. and Seiler, R. W. (1994) Transcranial doppler monitoring in head injury: relations between type of injury, flow velocities, vasoreactivity, and outcome. *Neurosurgery*, **34**.
- Strandgaard, S. (1976) Autoregulation of cerebral blood flow in hypertensive patients: the modifying influence of prolonged antihypertensive treatment on the tolerance to acute, drug-induced hypotension. *Circulation*, **53**, 720–727.
- Strandgaard, S., Olesen, J., Skinhoj, E. and Lassen, N. A. (1973) Autoregulation of brain circulation in severe arterial hypertension. *Br Med J*, **1**, 507–510.
- Strebel, S., Lam, A. M., Matta, B., Mayberg, T. S., Aaslid, R. and Newell, D. W. (1995) Dynamic and static cerebral autoregulation during isoflurane, desflurane, and propofol anesthesia. *Anesthesiology*, **83**, 66–76.
- Tachtsidis, I., Elwell, C. E., Leung, T. S., Lee, C. W., Smith, M. and Delpy, D. T. (2004) Investigation of cerebral haemodynamics by near-infrared spectroscopy in young healthy volunteers reveals posture-dependent spontaneous oscillations. *Physiol Meas*, **25**, 437–445.
- Taylor, J. A. and Eckberg, D. L. (1996) Fundamental relations between short-term rr interval and arterial pressure oscillations in humans. *Circulation*, **93**, 1527–1532.
- Tiecks, F. P., Douville, C., Byrd, S., Lam, A. M. and Newell, D. W. (1996) Evaluation of impaired cerebral autoregulation by the valsalva maneuver. *Stroke*, **27**, 1177–1182.
- Tiecks, F. P., Lam, A. M., Aaslid, R. and Newell, D. W. (1995) Comparison of static and dynamic cerebral autoregulation measurements. *Stroke*, **26**, 1014–1019.
- Tominaga, S., Strandgaard, S., Uemura, K., Ito, K. and Kutsuzawa, T. (1976) Cerebrovascular co₂ reactivity in normotensive and hypertensive man. *Stroke*, **7**, 507–510.
- Torizuka, K., Hamamoto, K., Morita, R., Mukai, T., Kosaka, T., Handa, J. and Nishitani, H. (1971) Regional cerebral blood flow measurement with xenon 133 and the scinticamera. *Am. J. Roentgenol.*, **112**, 691–700.
- Toronov, V., Walker, S., Gupta, R., Choi, J. H., Gratton, E., Hueber, D. and Webb, A. (2003) The roles of changes in deoxyhemoglobin concentration and regional cerebral blood volume in the fmri bold signal. *NeuroImage*, **19**, 1521–1531.
- Treib, J., Haass, A., Koch, D., Grauer, M. T., Stoll, M. and Schmirigk (1996) Influence of blood pressure and cardiac output on cerebral blood flow and autoregulation in acute stroke measured by tcd. *European Journal of Neurology*, **3**, 539–543.

- Triantafyllou, C., Hoge, R. D., Krueger, G., Wiggins, C. J., Potthast, A., Wiggins, G. C. and Wald, L. L. (2005) Comparison of physiological noise at 1.5 t, 3 t and 7 t and optimization of fmri acquisition parameters. *Neuroimage*, **26**, 243–250.
- Ursino, M., Iezzi, M. and Stocchetti, N. (1995) Intracranial pressure dynamics in patients with acute brain damage: a critical analysis with the aid of a mathematical model. *Biomedical Engineering, IEEE Transactions on*, **42**, 529–540.
- Ursino, M. and Lodi, C. A. (1997) A simple mathematical model of the interaction between intracranial pressure and cerebral hemodynamics. *J Appl Physiol*, **82**, 1256–1269.
- (1998) Interaction among autoregulation, co2 reactivity, and intracranial pressure: a mathematical model. *Am J Physiol*, **274**, 1715–1728.
- Ursino, M., Ter Minassian, A., Lodi, C. A. and Beydon, L. (2000) Cerebral hemodynamics during arterial and co(2) pressure changes: in vivo prediction by a mathematical model. *Am J Physiol Heart Circ Physiol*, **279**, 2439–2455.
- Vesely, A., Sasano, H., Volgyesi, G., Somogyi, R., Tesler, J., Fedorko, L., Grynszpan, J., Crawley, A., Fisher, J. A. and Mikulis, D. (2001) Mri mapping of cerebrovascular reactivity using square wave changes in end-tidal pco2. *Magnetic Resonance in Medicine*, **45**, 1011–1013.
- Wang, R., Foniok, T., Wamsteeker, J. I., Qiao, M., Tomanek, B., Vivanco, R. A. and Tuor, U. I. (2006) Transient blood pressure changes affect the functional magnetic resonance imaging detection of cerebral activation. *NeuroImage*, **31**, 1–11.
- Wang, S. and Tang, M. (2004) Exact confidence interval for magnitude-squared coherence estimates. *Signal Processing Letters, IEEE*, **11**, 326–329.
- Watkins, L. L., Fainman, C., Dimsdale, J. and Ziegler, M. G. (1995) Assessment of baroreflex control from beat-to-beat blood pressure and heart rate changes: a validation study. *Psychophysiology*, **32**, 411–414.
- Wei, E. P. and Kontos, H. A. (1982) Responses of cerebral arterioles to increased venous pressure. *Am J Physiol*, **243**.
- Welch, P. D. (1967) The use of fast fourier transform for the estimation of power spectra: A method based on time averaging over short, modified periodograms. *IEEE Transactions on Audio and Electroacoustics*, **15**, 70–73.
- Whitcher, B., Craigmile, P. F. and Brown, P. (2005) Time-varying spectral analysis in neurophysiological time series using hilbert wavelet pairs. *Signal Process.*, **85**, 2065–2081.
- Whitcher, B. and Craigmile, P. F. (2004) Multivariate spectral analysis using hilbert wavelet pairs. *International Journal of Wavelets, Multiresolution and Information Processing*, **2**, 567–587.
- White, R. P. and Markus, H. S. (1997) Impaired dynamic cerebral autoregulation in carotid artery stenosis. *Stroke*, **28**, 1340–1344.
- Willis, T. (1664) *Cerebri Anatome*. Martin and Allestry.
- Wilson, D. A., Traystman, R. J. and Rapela, C. E. (1985) Transient analysis of the canine cerebrovascular response to carbon dioxide. *Circ Res*, **56**, 596–605.
- Wise, R. G., Ide, K., Poulin, M. J. and Tracey, I. (2004) Resting fluctuations in arterial carbon dioxide induce significant low frequency variations in bold signal. *Neuroimage*, **21**, 1652–1664.
- Wollner, L., McCarthy, S. T., Soper, N. D. and Macy, D. J. (1979) Failure of cerebral autoregulation as a cause of brain dysfunction in the elderly. *British medical journal*, **1**, 1117–1118.
- Woolrich, M. W., Ripley, B. D., Brady, M. and Smith, S. M. (2001) Temporal autocorrelation in univariate linear modeling of fmri data. *Neuroimage*, **14**, 1370–1386.
- Young, W. L., Kader, A., Prohovnik, I., Ornstein, E., Fleischer, L. H., Ostapkovich, N., Jackson, L. D. and Stein, B. M. (1993) Pressure autoregulation is intact after arteriovenous malformation resection. *Neurosurgery*, **32**.
- Young, W. L., Prohovnik, I., Ornstein, E., Ostapkovich, N. and Matteo, R. S. (1991) Cerebral blood flow reactivity to changes in carbon dioxide calculated using end-tidal versus arterial tensions. *Journal of cerebral blood flow and metabolism : official journal of the International Society of Cerebral Blood Flow and Metabolism*, **11**, 1031–1035.
- Zhang, R., Zuckerman, J. H., Giller, C. A. and Levine, B. D. (1998a) Transfer function analysis of dynamic cerebral autoregulation in humans. *Am J Physiol*, **274**, 233–241.
- Zhang, R., Zuckerman, J. H., Iwasaki, K., Wilson, T. E., Crandall, C. G. and Levine, B. D. (2002) Autonomic neural control of dynamic cerebral autoregulation in humans. *Circulation*, **106**, 1814–1820.
- Zhang, R., Zuckerman, J. H. and Levine, B. D. (1998b) Deterioration of cerebral autoregulation during orthostatic stress: insights from the frequency domain. *J Appl Physiol*, **85**, 1113–1122.
- Zhao, H., Lu, S., Zou, R., Ju, K. and Chon, K. (2005) Estimation of time-varying coherence function using time-varying transfer functions. *Annals of Biomedical Engineering*, **33**, 1582–1594.
- Zheng, Y., Martindale, J., Johnston, D., Jones, M., Berwick, J. and Mayhew, J. (2002) A model of the hemodynamic response and oxygen delivery to brain. *Neuroimage*, **16**, 617–637.